Stony Brook University

Interneuron Subgroups Identified in the Mouse Visual Cortex

A Dissertation Presented

by

Jessica Susan Helm

to

The Graduate School

in Partial Fulfillment of the

Requirements

for the Degree of

Doctor of Philosophy

in

Neuroscience

Stony Brook University

December 2012

Stony Brook University

The Graduate School

Jessica Susan Helm

We, the dissertation committee for the above candidate for the

Doctor of Philosophy degree, hereby recommend

acceptance of this dissertation.

Lonnie Wollmuth - Dissertation Advisor
Professor, Department of Neurobiology and Behavior

Gary Matthews – Chairperson of Defense
Professor, Department of Neurobiology and Behavior

David Talmage
Associate Professor, Department of Pharmacological Sciences

Arianna Maffei
Assistant Professor, Department of Neurobiology and Behavior

James Dilger
Professor, Department of Anesthesiology, Stony Brook University School of Medicine

This dissertation is accepted by the Graduate School

Charles Taber

Interim Dean of the Graduate School

Abstract of the Dissertation

Interneuron Subgroups Identified in the Mouse Visual Cortex

by

Jessica Susan Helm

Doctor of Philosophy

in

Neuroscience

Stony Brook University

2012

As information flows through a cortical circuit, layers 2/3 provide an important area for signal processing and integration, and inhibitory interneurons are crucial to this function. Diversification of inhibitory interneurons provides the means for diversification of function. Inhibitory interneurons have been classified based on morphology, electrophysiology, and molecular markers, and each classification provides additional insight into how an interneuron type could shape information flow in the cortical circuit. Parvalbumin (PV) and somatostatin (SOM) are markers for two of the most common, distinct, and well-characterized groups of inhibitory interneurons in the cortex. Studies in the somatosensory cortex have divided SOM interneurons into subgroups based on electrophysiology (Halabisky et al. 2006), but the fine structure of variations in electrophysiology of the fast spiking 'basket' type PV interneurons have not been defined. This thesis provides a method for objective classification of interneurons based on passive and active firing properties, and verifies the effectiveness of the method by blindly classifying PV and SOM interneurons into the correct groups. Using this method, four

PV interneuron subgroups are identified in layers 2/3 of the visual cortex. Independent support for this classification is provided by the fact that the subgroups also differed in excitatory synaptic input. These subgroups would each be capable of fulfilling a distinct functional role in the neural circuit.

Table of Contents

List of Figures

List of Tables

Acknowledgments

This dissertation was made possible through the support of the Neuroscience Program and the Department of Neurobiology and Behavior, the Wollmuth Lab, my dissertation committee, and my husband Brian Fix. I would like to acknowledge the support and contributions of the members of the Wollmuth Lab past and present, including Cathleen Hewlett and Junryo Watanabe who taught me slice electrophysiology, Alexandra Corrales who has always been there when I needed support or advice, Martin Prieto, Catherine Salussolia, Iehab Talkuder, Rashek Kazi, and Quan Gan for helpful discussion and comments, and most especially Gulcan Akgul for her work collecting data used in this dissertation. Without Gulcan this dissertation could not happened. I would like to thank my advisor, Dr. Lonnie Wollmuth, for his willingness to see me over all the hurdles we encountered, and for his time and excellent writing advice. I am grateful to Dr. Josh Huang and the rest of his laboratory for assistance with mice, and to Drs. Arianna Maffei and Brian Fix for their technical assistance and advice. Thanks also to the many other members of the graduate program I consulted with over the years. I would like to thank my dissertation committee – Dr. Gary Matthews, Dr. Arianna Maffei, Dr. David Talmage, Dr. Jim Dilger, and Dr. Lonnie Wollmuth – for their support and advice.

The following figures have been reprinted with permission from the copyright holders. Figure 1-4 is reprinted from (Markram et al. 2004) with permission from the Nature Publishing Group. Figure 1-5 is reprinted from (Burkhalter 2008) with permission from the Frontiers Research Foundation. Figure 1-6 is reprinted from (Kubota et al. 2011) with permission from the Oxford University Press.

CHAPTER 1: INTRODUCTION

Computation in the brain and within visual areas is based on complex interactions between excitatory and inhibitory neurons operating in feed-forward and feedback circuits, reviewed in (Douglas 2004). Two general types of neurons underlie this synaptic activity - pyramidal neurons and interneurons. Pyramidal neurons have glutamatergic excitatory outputs that project out of the cortex and to other cortical areas as well as to local targets (Kandel 2000). These neurons ultimately convey the sum of local circuit activity between layers and to other regions of the brain. In contrast, interneurons are synaptically restricted to targets in the local cortical column. Most are GABAergic, and inhibit the activity of their post-synaptic target (Kandel 2000). These inhibitory interneurons suppress excitation in circuits to shape the timing and activity of neuronal firing and modulate the output of the neocortex by inhibiting pyramidal neurons (Burkhalter 2008).

This focus of this dissertation is on inhibitory interneurons in layers 2/3 of the visual cortex, a key layer for cortical processing. Specifically, parvalbumin expressing (PV) and somatostatin expressing (SOM) interneurons are grouped based on their membrane properties using cluster analysis (discussed in the chapter 2). Following this validation of clustering methodology, subgroups of PV interneurons are identified which may contribute uniquely to neural circuits in layers 2/3.

This chapter introduces the sensory system and the circuits in which PV and SOM interneurons are functioning, reviews the diversity in inhibitory interneurons, and finally reviews some of the mechanisms with which PV and SOM interneurons respond to a dynamic circuit.

VISUAL PROCESSING

Visual Cortex

Visual perception is initiated in the retina by the transduction of light into neuronal activity. Retinal processing of the visual signal detects contrast and intensity (Kuffler 1953), then the output is sent retinotopically to the thalamus. Retinotopy means that the two dimensional projection of the visual field is conserved as it is conveyed to neurons. By the time visual information leaves the thalamus, it has been processed in both the retinal ganglia and thalamic ganglia to enhance contrast. Thalamocortical pathways project visual information retinotopically to the primary visual cortex (Figure 1-1). Local processing in the visual cortex enables the detection of line orientations, movement, and more complex line features (Hubel D.H. 1962). Subsequent processing of feature detection is parceled out to modular rostral and lateral secondary visual areas, to refine perception of form, color, motion, and depth, eventually resulting in object recognition and spatial perception.

Information flow largely moves through the cortex up and down within a vertical column. The cortex is divided into different layers that lie parallel to the pia, or surface of the cortex (Figure 1-1, upper image). Six layers are generally distinguished based on cell type, density, and connectivity, although the prominence of the different layers varies between cortical areas as illustrated in the left and middle columns in Figure 1. The layers are interconnected by the projections of neuronal axons and dendrites, illustrated in Figure 1 in the column on the right. Although layers are recurrently interconnected, the vertical flow through the cortex can be simplified to the following circuit: efferents from the thalamus terminate in layer 4, layer 4 neurons project to layers 2/3, and layers 2/3 output to layer 5 (Figure 1-2), reviewed in (Douglas 2004).

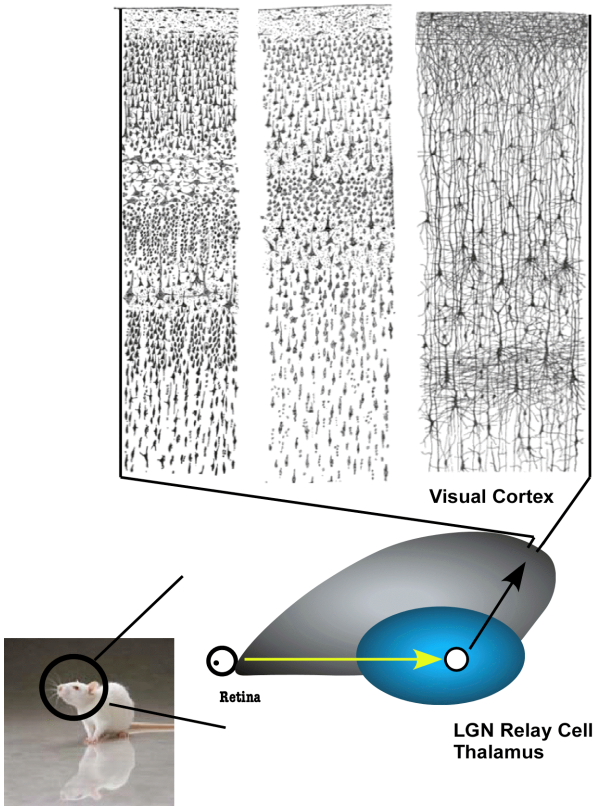

Figure 1-1. Overview of signal processing in the visual cortex.
Visual information is translated into neural impulses at the retina. A retinotopic projection of the visual information is sent to the thalamus and from the thalamus to the cortex. The cortex is composed of cells arranged in a laminar fashion, shown above in a drawing of three stained cortical sections by Ramon y Cajal. Visual cortex (left column) and motor cortex (middle column) from a human was stained to show cell bodies, while the column on the right is human cortex stained to show axons and dendrites.

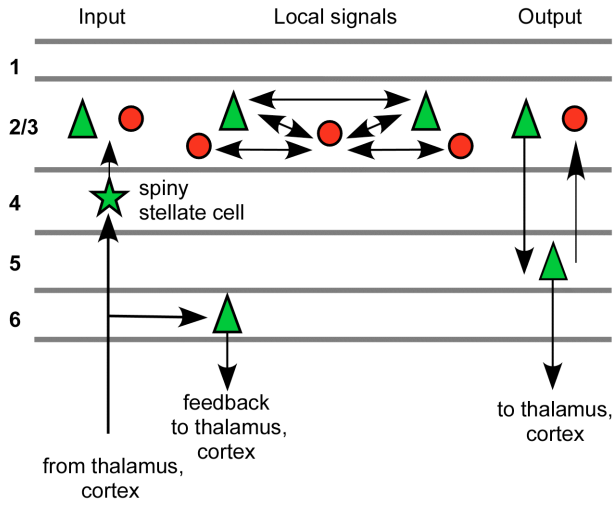

Figure 1-2. Simplified circuit diagram of vertical flow of information through the laminar cortex.
Input arrives in layer 4, is sent to layers 2/3 where it is processed by local signals, then flows to layers 5 and 6, where it is sent to the thalamus or other cortical areas.

Information flows between cortical areas in two ways; through the thalamus and pulvinar, or directly from one cortical area to another. Pyramidal cells in layer 6 provide feedback to the areas of the thalamus connecting to that cortical area while pyramidal neurons in layer 5 project to other thalamic areas which preferentially connect with other cortical areas (Figure 1-3) (Shipp 2003). Intercortical connections between visual areas are arranged hierarchically. Axons projecting from 'lower' cortical areas that receive primary visual input to 'higher' areas are called 'feed-forward' projections, while axons projecting from 'higher' areas that receive less primary visual input to 'lower' primary cortical areas are called 'feed-back' projections (Coogan and Burkhalter 1993). Many direct inter-areal feed-forward projections arise from layer 3 and project to layer 4 in higher areas, providing processed visual input where the primary cortex receives primary visual input (Figure 1-3) (Felleman 1991). Direct inter-areal feed-back projections arise from layers 5 and 6 and project to multiple layers including layer 1, but avoid layer 4 (Figure 1-3) (Felleman 1991).

Layer 2/3 thus serves as the nexus of both vertical and inter-cortical information flow through the cortex, making it a key area for signal convergence, processing, and modulation.

Layer 2/3 organization

Input from layer 4 provides the primary interlayer stimulus to layer 2/3, and the primary excitatory output from layers 2/3 targets layer 5 (Thomson et al. 2002). In addition to feed-forward excitatory input from layer 4, layer 2/3 pyramidal cells (green triangles in Figure 1-2) also receive excitation from other pyramidal cells in layers 2/3 (Feldmeyer et al. 2006; Mason et al. 1991). Layer 2/3 interneurons (red circles in Figure 1-2) receive feed-forward excitatory input from layer 4, lateral excitation and inhibition from layers 2/3, and feed-back excitation from

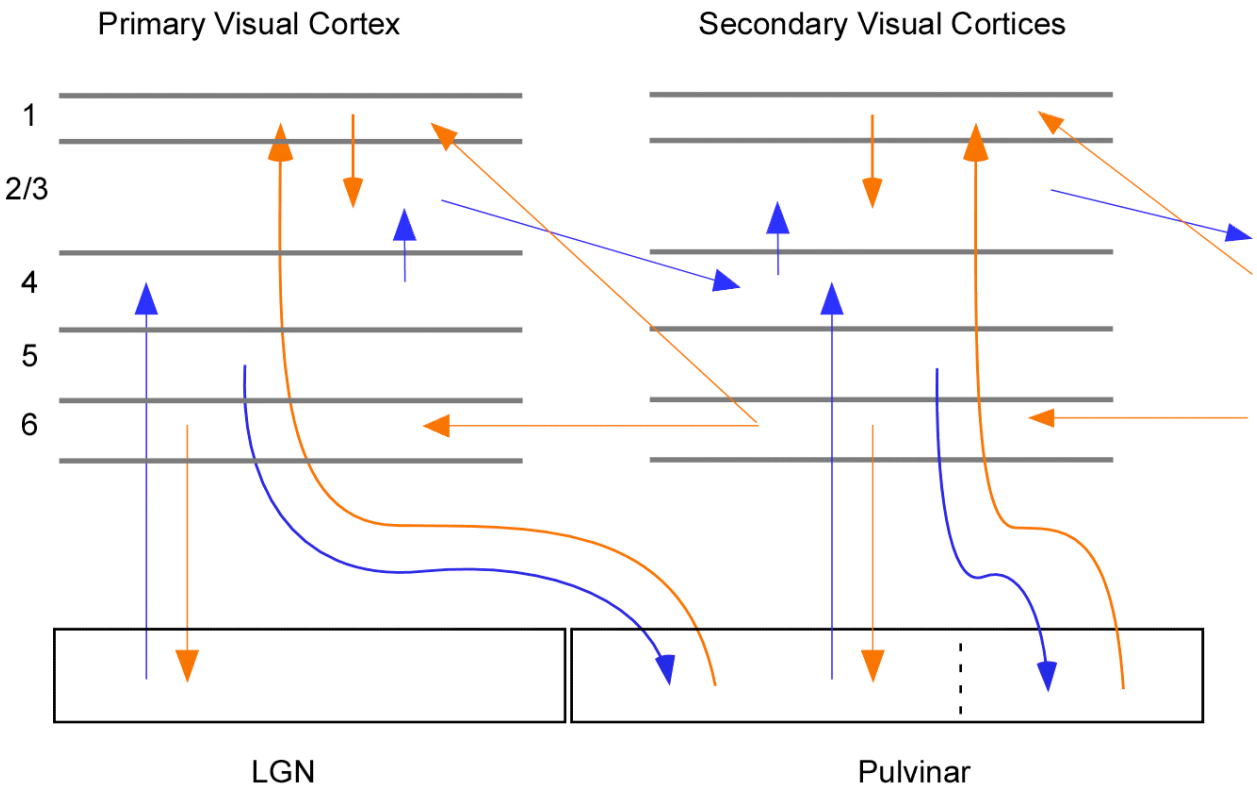

Figure 1-3. Feed-forward and feedback pathways in the visual cortex are hierarchical and layer specific.
Inter-cortical feed-forward or ascending pathways arise largely from layers 2/3 and terminate in layer 4. Inter-cortical feedback or descending pathways arise from layer 6 and terminate in layer 1 and 6. Feed forward thalamocortical pathways arise from the LGN or pulvinar and terminate largely in layer 4 and feed-forward cortico-thalamic pathways arise from layer 5 and terminate in the pulvinar. Feedback from the cortex to the thalamus or pulvinar comes from layer 6, while feedback from the pulvinar terminates in layer 1. Adapted from (Shipp 2007).

layer 5 (Dantzker and Callaway 2000; Thomson et al. 2002), and make local connections with layer 2/3 pyramidal cells and interneurons.

Most of the synapses that layers 2/3 neurons make or receive are with other layers 2/3 neurons (Douglas 2004). Pyramidal to pyramidal connections are relatively infrequent and decrease rapidly with distance, from a connection probability of 0.09 at 25 um to 0.06 at 100 um (Holmgren et al. 2003). In contrast, interneuron connections with pyramidal cells are much more common and occur at a greater distances, with a connection probability of around 0.7 between 0 and 200 um (Fino and Yuste 2011; Holmgren et al. 2003), meaning interneurons are connected to the majority of pyramidal cells around them. A third of these connections are reciprocal, though the probability of reciprocal connections begins to decline with distance (Fino and Yuste 2011). Interneurons are connected with other interneurons and in particular with other interneurons of the same type (Galarreta and Hestrin 2002; Gonchar and Burkhalter 1999; Tamas et al. 1998). With multiple types of interneurons, it is possible to have multiple overlapping inhibitory circuits with varying roles in the circuit.

CORTICAL INHIBITORY INTERNEURONS

Inhibitory interneuron diversity

Cortical inhibitory interneurons are diverse in properties and function (Markram et al. 2004). Inhibitory interneurons can be classified into different types based on different properties, most commonly firing pattern, morphology, and/or expression of molecular markers (Ascoli et al. 2008). These interneuron types can overlap, so that an interneuron classified by firing pattern might fall into multiple morphological classes and vice versa (Burkhalter 2008).

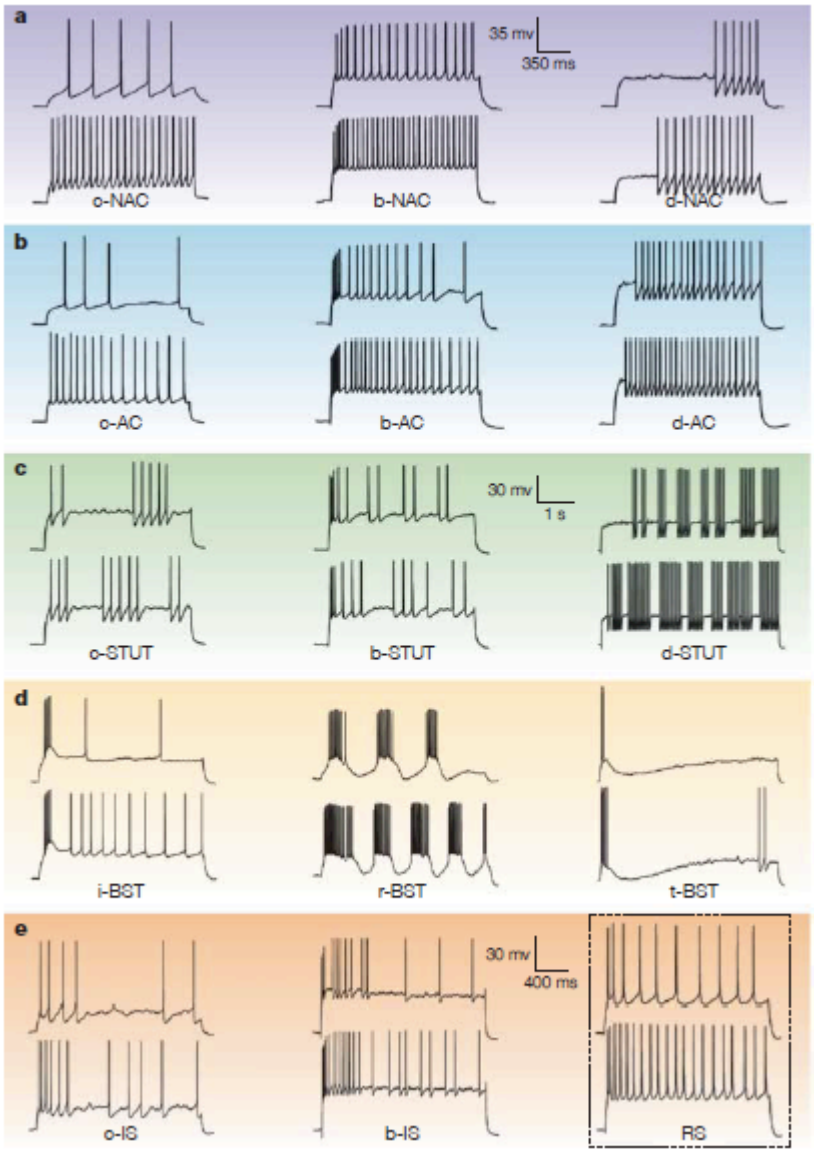

Figure 1-4. Inhibitory interneurons can be grouped based on their firing patterns.
A system of inhibitory interneuron classification based on firing patterns is shown. Firing patterns are divided into a. non-accomodating, b. accomodating, c. stuttering, d. bursting, and e. irregular spiking. The "classic" version of the firing pattern is shown in the left column and marked 'c-', while variations and combinations of these patterns are shown on the right. From (Markram et al. 2004).

Physiology.

Inhibitory interneurons have been classified into multiple groups based on the firing pattern and the shape of the action potential (AP) (Cauli et al. 1997). Inhibitory interneurons can initially be divided into fast spiking and regular spiking non-pyramidal interneurons. Fast spiking interneurons (Figure 1-4A) fire at high frequencies without adaptation or failure and have low membrane resistance and a narrow AP (Kawaguchi 1993; McCormick et al. 1985). The classical regular spiking interneuron (Figure 1-4B) cannot fire at high frequencies, shows spike frequency adaptation, and has a higher input resistance and a wider AP than the fast spiking interneurons (Kawaguchi 1995). Several additional groups of regular spiking non-pyramidal interneurons have been distinguished, including Late Spiking interneurons with a slow ramp onset (Kawaguchi 1995), Burst Spiking interneurons (Figure 1-4D) which fire several action potentials following a hyperpolarizing pulse (Cauli et al. 1997; Kawaguchi and Kubota 1993; 1997), and Irregular Spiking interneurons (Figure 1-4E), which fire a few early APs followed by single APs spaced at irregular intervals. A more exhaustive classification includes interneurons with combinations of these firing pattern features (Figure 1-4, columns at right)(Markram et al. 2004).

Morphology.

Interneuron morphology can be described by the direction, extent, and density of dentritic and axonal arborization relative to the soma, as well as the size and shape of the soma itself. Based on the number and orientation of primary dendrites leaving the soma, inhibitory interneurons have been called bipolar, bitufted, or multipolar (Porter et al. 1998; Reyes et al. 1998; Rozov et al. 2001b; Zilberter et al. 1999).

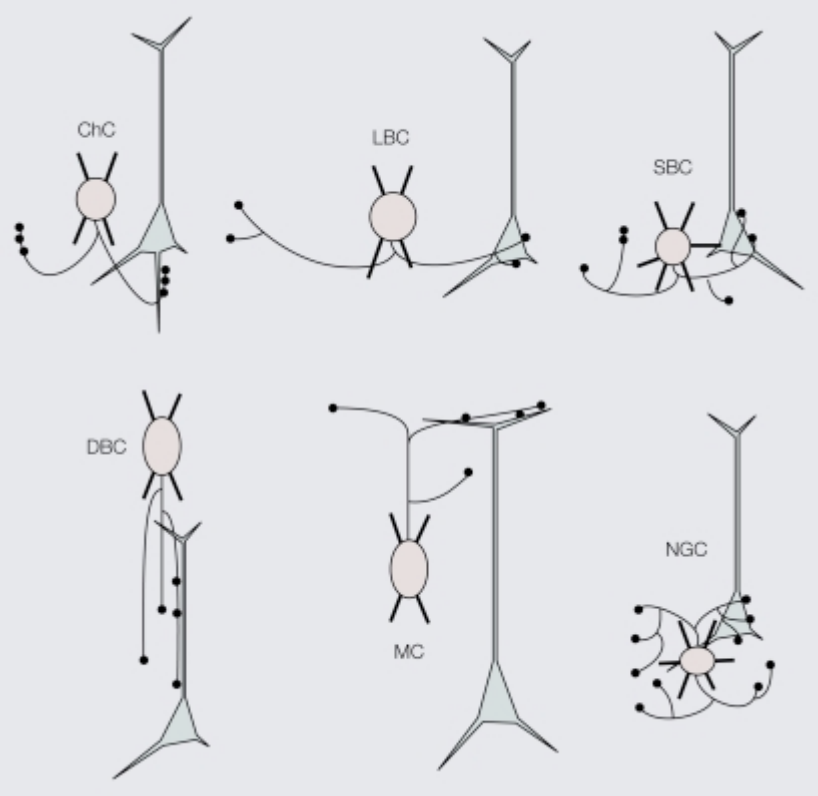

Figure 1-5. Six distinct morphological groups of inhibitory interneurons.
Morphological groups of inhibitory interneurons (red) can be defined using the extent, orientation, and target of axonal projections onto postsynaptic pyramidal neurons (gray). Chandelier cells (ChC), small basket cells (SBC), large basket cells (LBC), neurogliaform cells (NGFC), double bouquet cells (DBC) and Martinotti cells (MC). From (Burkhalter 2008).

Alternatively, interneurons may be grouped by the axon shape and postsynaptic target. Inhibitory interneurons characterized in such a manner include basket, chandelier, double bouquet, martinotti, and neurogliaform cells (Buhl et al. 1997) (Figure 1-5). Basket cells are so named because the majority of their axons target the postsynaptic cell's soma or perisomatic dendrite (Tamas et al. 2003; Tamas et al. 1998) in some cases appearing to form baskets. Basket cells have been divided morphologically into large, small, and nest basket cells which differ in the extent and branching of the axonal arbor (Wang et al. 2002). Chandelier cells feature distinctive vertically oriented axonal cartridges that lie alongside and target the postsynaptic neuron's axon initial segment (Somogyi et al. 1983). By targeting the soma and axon initial segment, basket and chandelier cells have greater control over the activity and thus output of their postsynaptic targets (Miles et al. 1996).

Unlike basket and chandelier cells, double bouquet, Martinotti and neurogliaform cells synapse onto dendritic shafts and spines (Kawaguchi and Kubota 1997; Somogyi and Cowey 1981; Tamas et al. 2003), giving them preferential control over the postsynaptic neuron's other synaptic inputs (Miles et al. 1996). Double bouquet cells have narrow vertically oriented axonal arborizations primarily descending from a fusiform soma (Kawaguchi 1995; Somogyi and Cowey 1981; Tamas et al. 1998). Martinotti cells are characterized by an axonal projection into and arborization within layer 1(Kawaguchi and Kubota 1997), with spiny dendrites (Wang et al. 2004). Neurogliaform cells feature a highly branched, dense, fine axonal network surrounding a small round soma (Kawaguchi 1995; Krimer et al. 2005).

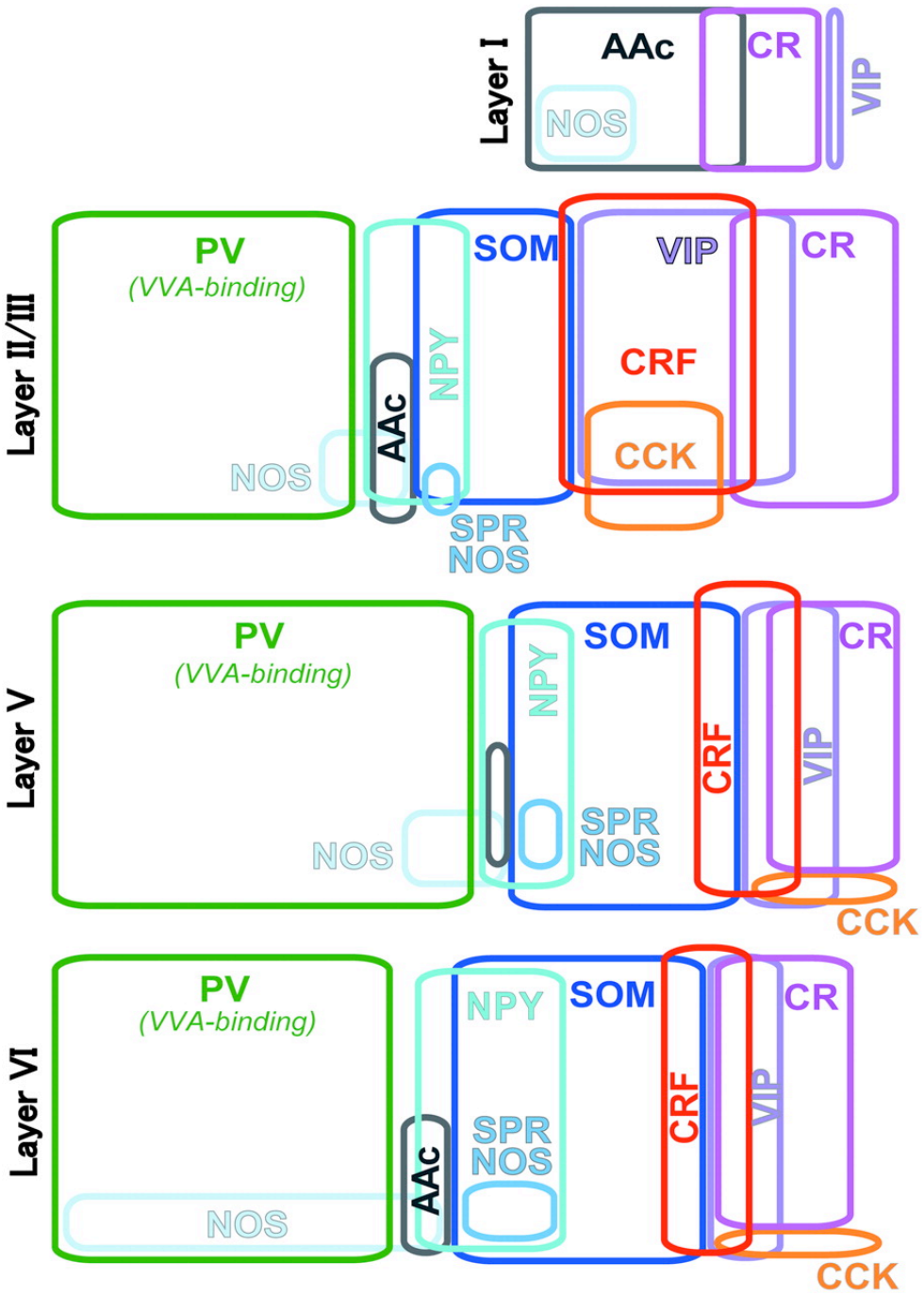

Figure 1-6. Inhibitory interneurons can be grouped based on the expression of molecular markers PV, SOM and VIP.
Most inhibitory interneurons express either PV, SOM, or VIP, and expression of these three markers is non-overlapping. PV interneurons are basket or chandelier fast spiking and MB cells, SOM include Martinotti cells, and VIP include irregular spiking cells. PV interneurons do not express most of the other molecular markers observed in SOM or VIP cells. From (Kubota et al. 2011).

Molecular markers.

Molecular markers can be used to distinguish almost all GABAergic interneurons into distinct non-overlapping groups (Figure 1-6) (Lee et al. 2010), in which membrane properties, morphology, and synaptic connectivity vary with group identity (Cauli et al. 2000; Dumitriu et al. 2007). Interneurons expressing the calcium binding protein parvalbumin (PV) do not overlap with interneurons expressing the neuropeptide somatostatin (SOM) (Gonchar et al. 2007). PV and SOM expressing interneurons do not overlap with interneurons expressing the serotonin receptor 5HT3aR mRNA (Lee et al. 2010). 5HT3aR labels a heterogenous group of interneurons, most expressing either the neuropeptide VIP (Lee et al. 2010) or the glycoprotein Reelin (Miyoshi et al. 2010). VIP expression does not overlap with PV or SOM (Kawaguchi and Kubota 1997), and together PV, SOM, and VIP positive interneurons make up at least 60% of the total inhibitory interneuron population (Xu et al. 2010). This dissertation focuses on PV as well as SOM interneurons, and identifies subgroups in PV interneurons.

PV is expressed in 40% of all cortical GABA-ergic interneurons (Gonchar et al. 2007; Rudy et al. 2011). PV interneurons correspond to a group of interneurons described variously as fast-spiking or multipolar interneurons, and include nest and large basket cell morphologies (Cauli et al. 1997; Strauss et al. ; Toledo-Rodriguez et al. 2005), as well as the distinctive chandelier cell (DeFelipe et al. 1989). Most PV interneurons show fast spiking, non-adapting, non-accommodating firing patterns (Povysheva et al. 2008). The exception is the multipolar bursting (MB) PV interneuron located at the border of layers 1 and 2, which has a large soma and a bursting, non fast-spiking firing pattern (Blatow et al. 2003). Fast-spiking PV interneurons typically have smooth (aspiny) dendrites, and axons that contact somatic and perisomatic postsynaptic locations (Galarreta and Hestrin 2002; Kawaguchi and Kubota 1998).

SOM is expressed in 20-30% of cortical GABA-ergic interneurons (Gonchar et al. 2007; Rudy et al. 2011). SOM interneurons mostly correspond to the classical regular spiking non-pyramidal interneurons, or to bitufted or Martinotti cells (Toledo-Rodriguez et al. 2005; Wang et al. 2004). However, there is also a stuttering faster spiking SOM subgroup in layer 4 which synapses onto other neurons in the same layer (Ma et al. 2006). The majority of SOM interneurons in layers 2/3 are in the first group, and show accommodating, adapting, and rapid-spiking firing patterns. Morphologically, most have spiny dendrites, and feature an axon that extends upwards into and arborizes in layer 1 as is typical for Martinotti cells. SOM axons synapse distally on the post-synaptic dendrite (Kawaguchi and Kondo 2002).

VIP is expressed in about 12% of cortical GABA-ergic interneurons (Gonchar et al. 2007; Rudy et al. 2011). VIP expressing interneurons are bipolar, irregular spiking (Cauli et al. 2000; Porter et al. 1998) or burst spiking double bouquet cells or small basket cells (Kawaguchi and Kubota 1997; Toledo-Rodriguez et al. 2005; Wang et al. 2002).

Inhibitory interneurons in development

Cortical inhibitory interneurons are born in the median and caudal ganglionic eminences (MGE and CGE) of the embryonic ventral telencephalon, travel along the cortical plate to their destination along the cortex, migrate into the cortical plate at P1, and move into their final laminar destination over the next couple of weeks after birth (Miyoshi and Fishell 2011).

There are developmental differences between the major inhibitory interneuron groups. PV interneurons are continuously generated in prenatal development, while SOM interneurons are generated earlier and VIP interneurons generated later (E15+) (Miyoshi et al. 2007). PV and SOM interneurons both come from the median ganglionic eminence (Fogarty M. 2007) while VIP interneurons are derived from the caudal ganglionic eminence (Miyoshi et al. 2010). All

inhibitory interneuron groups reach a largely mature laminar distribution by P7 (Miyoshi and Fishell 2011). PV interneurons begin to develop mature membrane properties around P7 (Okaty et al. 2009) and have the low membrane resistance and fast spiking firing pattern characteristic of mature PV interneurons by P14 (Goldberg et al. 2011). PV interneurons continue to mature until the early P20s, early in the critical period (Lazarus and Huang 2011). SOM interneurons follow a similar time course except that SOM maturation extents into the late P20s, the critical period when ocular dominance is set.

NEURAL NETWORK ACTIVITY IN LOCAL CIRCUITS

The individual response to a change in circuit activity is a key aspect of a neuron's role in that circuit (Somogyi and Klausberger 2005). The response can range in duration from short term to long term, and can involve changes in membrane properties, synapses, and even morphology (Lee et al. 2008). Short changes in circuit activity usually lead to short term changes mediated by post-transcriptional mechanisms (Miller et al. 2011), while longer shifts in circuit activity lead to long term changes mediated by modifications in gene transcription (Malenka and Bear 2004). Of particular interest to neuron function are changes in firing patterns, synaptic transmission, and the ongoing balance of excitation and inhibition.

Firing Patterns

The firing patterns used to describe and even group inhibitory interneurons are generated by the differential expression of molecules with varying baseline and dynamic biophysical properties (Golomb et al. 2007; Markram et al. 2004; Mensi et al. 2012). Firing frequency can be delayed (Goldberg et al. 2008), burst (Blatow et al. 2003), accelerate (Miller et al. 2008), and adapt (Cauli et al. 1997). AP threshold (Azouz and Gray 2000) and AP peak, AHP peak, and

AHP area (Wang et al. 2004) can all change with activity or the degree and duration of activation of the neuron.

Potassium channels that activate quickly and inactivate slowly (e.g. Kv1) affect the likelihood of AP firing and thus the time to AP onset, and as they inactivate the firing frequency can accelerate (Miller et al. 2008). Potassium channels that are slow to activate and deactivate, including calcium activated potassium channels (Sah 1996) and voltage activated KCNQ channels (Otto et al. 2006), can generate spike frequency adaptation as they activate. However, these channels are apparently absent in SOM interneuron and the mechanisms underlying adaptation and AHP change in these cells remain unclear. AP threshold is dependent on the availability of voltage dependent sodium channels, and activity dependent inactivation of these channels can shift the threshold and affect firing frequency (Fleidervish et al. 1996).

Synaptic dynamics

Single postsynaptic responses in the cortex are too small to evoke a postsynaptic action potential, and the somatic amplitude of a postsynaptic potential depends on both the proximity and dynamic amplitude of the input (Buhl et al. 1997). A perisomatic input can depolarize the soma more than a distal one, and a larger or slower input has a greater potential for temporal and spatial summation. Closer, larger, or slower synaptic inputs therefore require fewer coincidental inputs to initiate an action potential. The location, amplitude and dynamic regulation of synaptic events are therefore integral to the question of whether a neuron will fire in response to activity.

The presynaptic contribution to a postsynaptic current response (I_{post}) can be simplified into three primary factors, described by the equation $I_{post} \propto N * P_r * Q$ (Kandel 2000). These factors are the number of release sites N, the probability of vesicular release P_r, and the quantal size per vesicle Q. In the simplest case, N equals the number of active synapses releasing vesicles. N can

change dynamically during development or in response to activity (Holtmaat et al. 2006). The probability of release is related to the size of the readily releasable pool (RRP) at each synapse (Dobrunz and Stevens 1997). Release probability increases in relation to the available intracellular calcium, which enters through voltage gated calcium channels (Dodge and Rahamimoff 1967). Modulation and location of these calcium channels relative to synaptic vesicles is therefore a major factor of release probability. Finally, quantal size is proportional to the average number of molecules of neurotransmitter contained in each vesicle. Q can vary based on neurotransmitter availability (Wu et al. 2007) and metabolic state (Juge et al. 2010).

Postsynaptic mechanisms also regulate synaptic amplitudes. The postsynaptic current I_{post} generated by the binding of neurotransmitter to receptors is proportional to product of the number of postsynaptic receptors N, the conductance of the receptors G, and the fraction of receptors occupied and opened by neurotransmitter P_o, described by the equation $I_{post} \propto NGP_o$ (Kandel 2000). Thus, a difference in postsynaptic neurotransmitter receptors can greatly affect the synaptic signal received.

In response to repetitive activation, synaptic events can facilitate, depress, or show a mix of the two, as reviewed in (Zucker and Regehr 2002). The mechanism engaged depends on the rate of vesicle priming and probability of release. Synapses with a higher probability of release and slower rate of priming will show depression as vesicles are depleted, while synapses with a lower probability of release and a faster rater of priming facilitate as calcium increases the release probability (Sudhof 2004). Synapses from pyramidal onto PV interneurons show depression in response to repetitive stimulation while synapses from pyramidal onto SOM interneurons show facilitation (Reyes et al. 1998; Rozov et al. 2001a). This underlies one important difference between PV and SOM interneuron's contribution to the neural circuit.

Depressing inputs have the greatest impact at low frequency or brief circuit activity, while facilitating inputs have a maximal impact with sustained higher frequency activity (Kapfer et al. 2007).

Some synapses show evidence of multivesicular release (MVR), in which more than one vesicle is released simultaneously at the same synapse. MVR has been identified at cortical pyramidal to PV interneuron synapses (Watanabe et al. 2005) and other synapses (Christie and Jahr 2006; Wadiche and Jahr 2001; Watanabe et al. 2005), and appears to be a common result of high release probability (Behrends and ten Bruggencate 1998; Foster et al. 2005; Searl and Silinsky 2002) and is thus experience dependent. Infrequent activity primes more vesicles and increases MVR, but repeated activity depletes the extra primed vesicles eliminating MVR, contributing to the depression characteristic of pyramidal to PV synapses (Watanabe et al. 2005).

Balance of Excitation and Inhibition

Cortical neurons are recurrently connected (Thomson and Bannister 2003), and in the absence of inhibition can generate runaway excitation (Lau et al. 2000). Inhibitory interneurons provide feed-forward and feedback inhibition that dampens excitation in the circuit (Haider et al. 2006). In a healthy brain, the level of excitation and inhibition remains evenly balanced even as the overall level of activation in the cortex varies (Haider et al. 2006). This balance of excitation permits functional processing (Haider et al. 2006; Yizhar et al. 2011).

Supported by the stabilizing influence of inhibitory interneurons, cortical networks can safely undergo increases in network activity that depolarizes the neurons in the network and brings them closer to threshold, increasing the impact of individual inputs (Haider et al. 2007). This increased network activity (UP state) scales up the response of the neuron to visual and other inputs, providing a mechanism for controlling gain in the network (Haider et al. 2007).

Within this balanced excited state, higher frequency fluctuations in the membrane potential arise from the synchronized activity of presynaptic inhibitory interneurons (Hasenstaub et al. 2005). These fluctuations are particularly powerful in the gamma range, and sharpen and enhance the timing and transmission excitatory inputs (Hasenstaub et al. 2005; Schaefer et al. 2006). Gamma frequency oscillations are generated by networks of PV interneurons and promotes cortical signal processing (Sohal et al. 2009).

Homeostatic changes also affect the input gain in circuits, and can be induced by elevating or suppressing the overall level of excitation for a long period of time (days). Multiple presynaptic and postsynaptic changes can mediate homeostatic response, including adding or removing receptors and increasing or decreasing release pool size (Bear 1995; Desai et al. 2002; Maffei and Turrigiano 2008; Morales et al. 2002; Turrigiano et al. 1998).

Inhibitory interneurons in Disease

Considering the central role of inhibitory interneurons in maintaining a balance of excitability in the brain, it is not surprising that inhibitory interneuron dysfunction has either been implicated in or has the potential to influence many disease states. Indeed, GABA-A receptors have been specifically targeted with sedatives and anti-anxiolytics (Chen et al. 2012). Because of their prevalence, differing short-term synaptic plasticity and postsynaptic connectivity, PV and SOM interneurons are of particular interest.

Epilepsy is the presence of runaway excitation, and disruptions in GABAergic signaling are linked to epilepsy (DeFelipe 1999; Galanopoulou ; Lau et al. 2000). Excess excitation is also associated with increased baseline gamma oscillations (Yizhar et al. 2011). Abnormal gamma frequency oscillations are implicated in both autism and schizophrenia. Especially strong baseline gamma frequency oscillations have been observed in autism and may contribute to

autism symptoms (Orekhova et al. 2007). Conversely, schizophrenic patients display decreased gamma oscillatory activity in response to sensory (Gallinat et al. 2004; Spencer et al. 2008) and cortical (Ferrarelli et al. 2008) stimulus.

Parvalbumin positive interneurons are specifically implicated in schizophrenia, reviewed in (Lewis et al. 2012). Loss of PV interneurons in mice disrupts gamma oscillations and impairs behavior in an animal model of schizophrenia (Lodge et al. 2009). Fewer PV expressing cells were observed in postmortem tissue samples from patients with schizophrenia and bipolar disorder (Torrey et al. 2005). It is even possible that PV interneurons may actually be immature in autism, schizophrenia, and bipolar disorder (Gandal et al. 2012).

CONCLUSION

Layers 2/3 are the point of intersection of information flow through the cortical column and between cortical areas. There are a large number of diverse inhibitory participants in the local layers 2/3 circuit with a high degree of connectivity and a wide range of dynamic response. PV and SOM interneurons are especially significant as the two largest groups. Interneurons in each group share multiple features with other members in the same group, including membrane, synaptic, and morphological properties. These features allow each group to contribute differently to information processing in the local circuit.

PV subgroups could similarly differ in multiple features allowing further refinement of circuit processes. Detailed quantification of PV interneuron membrane properties allows the identification of potential subtypes. The identification of PV subtypes differing in membrane properties would facilitate the study of this population of inhibitory interneurons, and offer the opportunity to investigate the role of the identified subtypes in healthy and diseased brain

function. To this end, I develop a clustering protocol and test it on the PV and SOM subgroups before using it to identify subgroups of PV interneurons based on membrane properties.

CHAPTER 2: CLUSTER ANALYSIS

ABSTRACT

Variation in the membrane properties of inhibitory interneurons allows different inhibitory interneurons to play different roles in local cortical circuits. PV fast spiking interneurons are a major group of inhibitory interneurons with no major physiological subgroups besides minor differences between chandelier and basket cells, although individual features are known to vary. Cluster analysis is a powerful way to identify patterns in data objectively, particularly when dealing with data in multiple dimensions where visual or subjective examination is difficult. Clustering procedures can be applied to parameters extracted from neuronal features to identify patterns and generate new classifications. This chapter describes the algorithms used in this dissertation to identify PV interneuron subgroups.

INTRODUCTION

Inhibitory interneurons can classified into different groups on the basis of various features, including morphology, membrane properties, and molecular markers (Burkhalter 2008; Markram et al. 2004). Historically, classification has been based on identifying a dominant feature such as the frequency of firing patterns (McCormick et al. 1985) or morphology (Kawaguchi 1995; Somogyi 1977), sorting according to that feature, and characterizing other features in the same class. Studies have also correlated the occurrence of multiple features of different types, such as firing pattern and expression of molecular markers (Kawaguchi and Kubota 1993) or morphology (Kawaguchi 1995). In either case, the selection of features to be correlated is subjective, and limited by the number of features that can be sorted simultaneously.

One major way to distinguish inhibitory interneurons is by the expression of molecular markers. In particular, parvalbumin (PV) and somatostatin (SOM) expression provide a useful

key to interneuron diversity (Kawaguchi and Kondo 2002). Each molecular marker is expressed by a distinct group of inhibitory interneurons with predictable and generalizable features. The consistency is strong enough that interneurons from the two groups can usually be distinguished from each other on the basis of just one or a couple of features, such as morphology or firing pattern. Based on these different features, PV and SOM interneurons are expected to contribute differently to the function of the neural network.

Even subtle differences in membrane properties would allow PV or SOM subgroups to act as a differential filter playing different roles in the neural network. Furthermore, the membrane properties would provide a real-time indication of subgroup membership, unlike morphological or synaptic features. However, the consistency of PV and SOM interneuron features makes it more difficult to identify subgroups.

In a more homogenous system in which no one feature seems entirely dominant, it becomes increasingly difficult to identify subgroups subjectively. Individual features may appear evenly distributed in a mixed population. Pairs of features may show a correlation, but putative class features may not be sufficiently separated to allow classification on this basis. PV and SOM interneuron membrane properties present this challenge. In such cases, multiple variables can be considered together using multi-dimensional cluster analysis to see if interneurons differ in these variables in a consistent way.

Cluster analysis has become an increasingly common tool in neurophysiology. Features subject to clustering include gene expression profiles (Cauli et al. 2000; Toledo-Rodriguez et al. 2004; Toledo-Rodriguez et al. 2005), neuronal morphology (Dumitriu et al. 2007; McGarry et al. 2010), synaptic kinetics (Dumitriu et al. 2007; Halabisky et al. 2006), membrane properties (Cauli et al. 2000; Halabisky et al. 2006; Krimer et al. 2005; McGarry et al. 2010; Nowak et al.

2003; Zaitsev et al. 2005), and a mix of interneuron parameters (Cauli et al. 2000; Halabisky et al. 2006; Helmstaedter et al. 2009; Karagiannis et al. 2009). The majority of studies use a single clustering algorithm - Ward's hierarchical clustering (Cauli et al. 2000; Dumitriu et al. 2007; Halabisky et al. 2006; Karube et al. 2004; Krimer et al. 2005; Nowak et al. 2003; Zaitsev et al. 2005). K-means has also been used to verify the clusters identified with Ward's method (Karagiannis et al. 2009; McGarry et al. 2010).

PV electrophysiology is generally treated as homogenous, however variations in firing patterns exist (Goldberg et al. 2008), suggesting the possible presence of subgroups. Multiple subgroups in SOM interneurons have been identified based on multivariable cluster analysis (Halabisky et al. 2006) then confirmed by the generation of SOM mouse strains in which different SOM electrophysiological subgroups were labeled (Ma et al. 2006). In this dissertation, multivariable cluster analysis is applied to parameters describing PV interneuron membrane properties to identify PV subgroups.

To find PV interneuron subgroups, I use Ward's and k-means clustering algorithms. In addition to the clustering algorithms, data manipulations and statistical tests are used to describe the clustering results. In this chapter, I explain the background and function of clustering, the Ward's and k-means clustering algorithms, and cluster related statistics.

CLUSTER ANALYSIS

A cluster is a set of objects that are similar to each other in some way. Clustering a dataset means grouping similar objects into the same cluster, and separating different objects into different clusters. The goal of cluster analysis is to distinguish significant patterns in the data. The patterns can then be used to accurately summarize the data, to describe the data in greater detail, or to perform further experiments on various subsets of the data. My purpose in

identifying clusters of PV interneurons is not necessarily to identify new rigid, distinct groups of interneurons, but to summarize and describe the natural patterns in the data and detail the extent to which any subgroups are present.

When represented as variables, clusters can be identified in patterns like a set of objects located in a higher density than the surrounding space, or objects in greater proximity to one another than to other objects (Figure 2-1). Humans are quite good at visually detecting patterns like clusters, as long as the pattern can be accurately represented in two or three dimensions. However, visual detection is subjective and difficult to apply consistently, and cannot detect patterns in more than three dimensions simultaneously. Algorithms and descriptive cluster statistics help to overcome this limitation.

Most forms of clustering use a metric to find a clustering solution. In the context of clustering, a metric is any measure applied to the clustering that is either optimized or otherwise used to make a clustering decision. In theory, a clustering algorithm could generate every possible combination of objects in the dataset and choose the cluster configuration that optimizes the metric criterion, such as minimal separation between objects in a cluster or maximal distance between clusters. However, as the number of objects to be clustered increases, such a computation becomes exponentially time and resource intensive. Instead of brute force combinations, heuristic algorithms apply the metric using a set of rules. The rules are designed to greatly reduce the computational requirements, making it possible to find the optimal or near optimal solution (Jain 1988; Murtagh 1985).

However, even in cases where natural clusters are very clear, no perfect clustering algorithm exists, and there will not always be one correct cluster arrangement (Jain 1988). Different clustering algorithms and metrics are better at finding different kinds of patterns in the

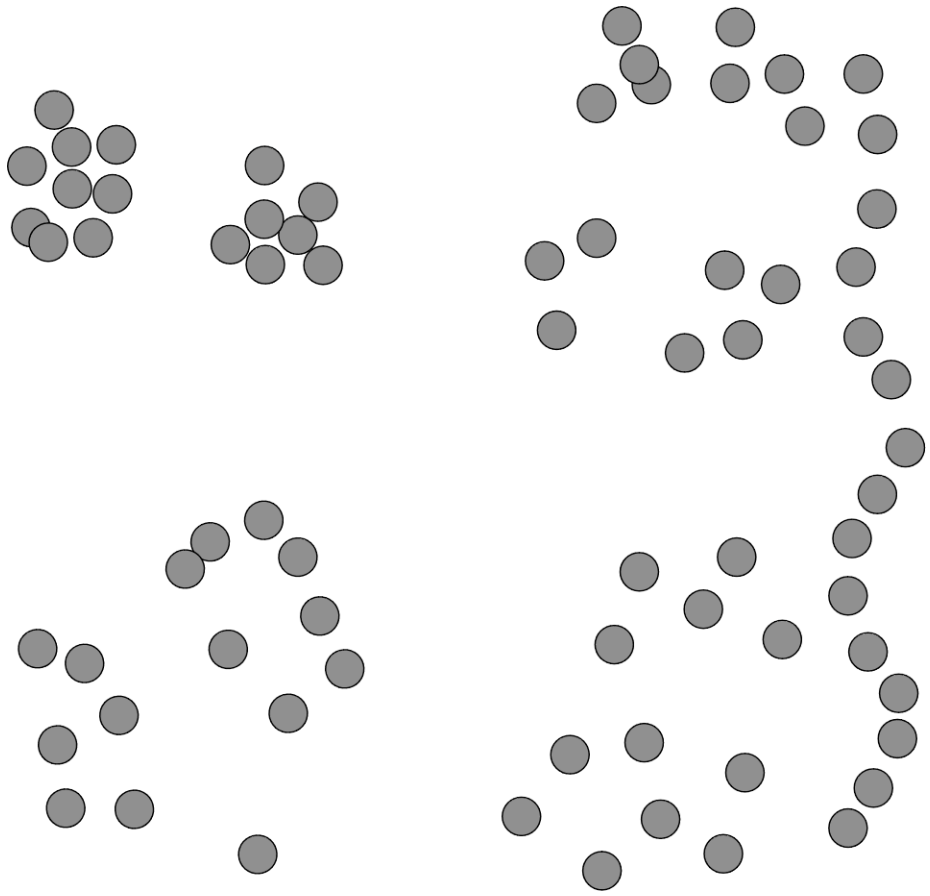

Figure 2-1. Examples of different types of clusters and numbers of clusters.
Clusters can have different shapes and densities, from compact and spherical clusters (upper left), to loose clusters (lower center), or form chain-like patterns (right). The number of clusters seen depends in part on the viewer's perspective.

data, and the experimenter must consider both the observable or known patterns in the data and the kind of pattern desired to select an appropriate algorithm. For example, in Figure 2-1, the long wavelike pattern on the right may be a new and unknown factor to be highlighted and investigated, or could result from some well-known factor and distract from novel patterns distributed like the smaller clusters on the left.

A major challenge in cluster analysis is determining the correct number of clusters in the data. If too many or too few clusters are used, information can be lost (Figure 2-2). Even a randomly generated dataset can be clustered, but such a clustering does not yield additional information, and information about larger patterns is absent. Using too few clusters, important distinctions between groups are lost. In Figure 2-2, one could allow for two clusters, a red and a non-red cluster. However, the distinction between the red stars and circles or blue and green objects would be lost. Conversely, one could allow for 4 clusters: blue, green, stars, and red circles. In this case the commonality between red circles and stars is lost. It is also important to consider how much information is useful. Each unique object could be placed into its own cluster, but then it would become difficult to summarize patterns in the data. The choice of number of clusters is also a matter of perspective. For example, Figure 2-1 contains anywhere from four to ten or more distinct groups of higher density objects. Depending on the nature of the data and the purpose of the investigator, either the four largest clusters or ten or more clusters may be the most significant information to report.

Suggestions about an optimal number of clusters can come from descriptive cluster statistics, information on the relationships between clusters, comparison between multiple algorithms, and examination of the clusters and the objects clustered in them.

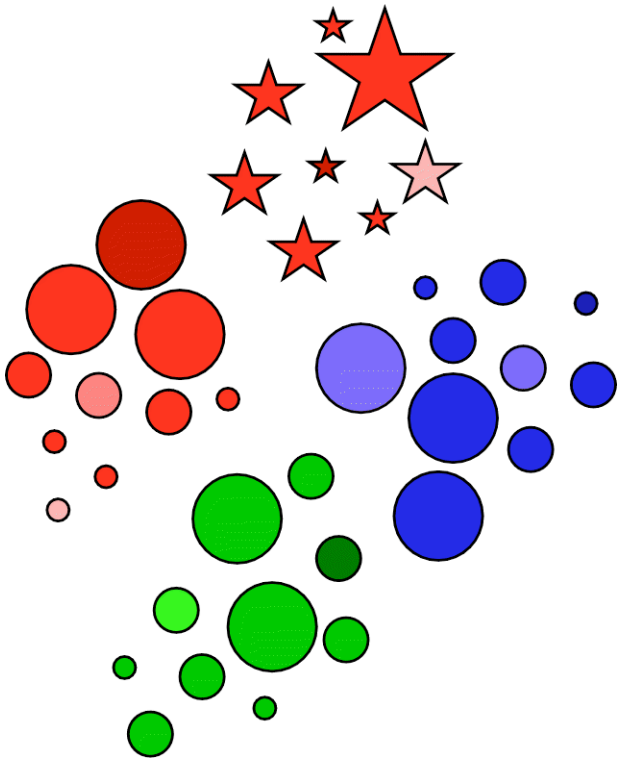

Figure 2-2. Finding the right number of clusters.
To maximize the information conveyed by clusters, the right number of clusters must be used. Object information is represented by color, shape, size, and two-dimensional distance.

Clustering Algorithms.

Two different types of clustering algorithms were used to find clusters of PV interneurons: a hierarchical agglomerative algorithm (Ward's) and a non-hierarchichal, partitioning algorithm (k-means). Both algorithms are unsupervised - done without influence or knowledge of existing groups within the dataset (Murtagh 1987). This differs from a supervised classification in which samples are sorted into clusters using known class membership as a discriminator (Figure 2-3). Both algorithms use Euclidean distances to measure distances between interneurons or clusters of interneurons. Euclidean distance is measured as the root of the squared distance between two points in space in each dimension, summed across all dimensions. The calculation is shown for two dimensions in Figure 2-4. For the distance between points *a* and *b* in *D* dimensions, the formula for the Euclidean distance is:

$$\sqrt{\sum_{d=1}^{D}\left(a_d - b_d\right)^2}\,.$$

Note that the squared Euclidean distance between two objects is proportional to the variance.

Because distance is summed across all dimensions, it is very important that each variable be scaled to the same scale before distances are calculated. I use Z standardization to normalize each parameter's data to a mean of zero and a standard deviation of one by subtracting the parameter mean and dividing by the standard deviation.

$$\frac{x - \bar{x}}{\sqrt{\frac{1}{N-1}\sum_{i=1}^{N}(x_i - \bar{x})^2}}$$

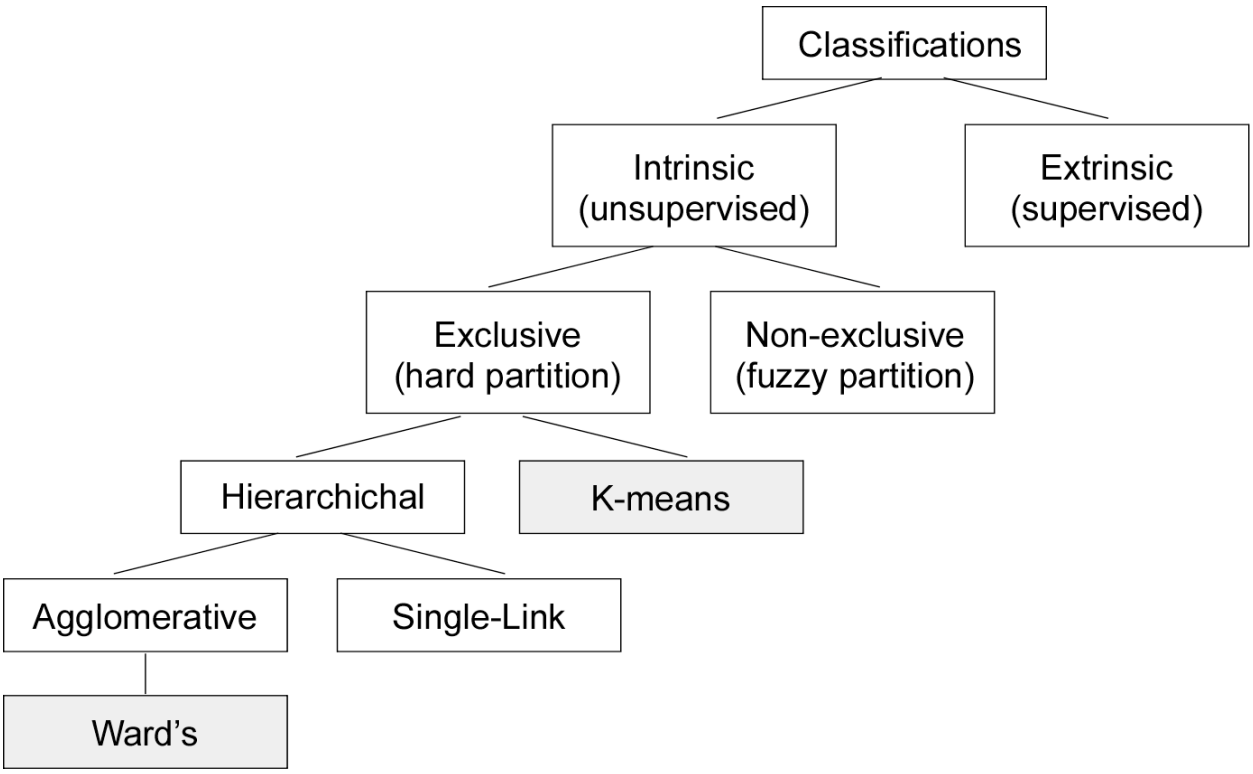

Figure 2-3 Types of classification algorithms.
This flow chart illustrates some of the most common categories of classification algorithms. Unsupervised clustering is a form of classification that does not use known classes to cluster data. The Ward's and k-means algorithms used to cluster interneuron data are shaded.

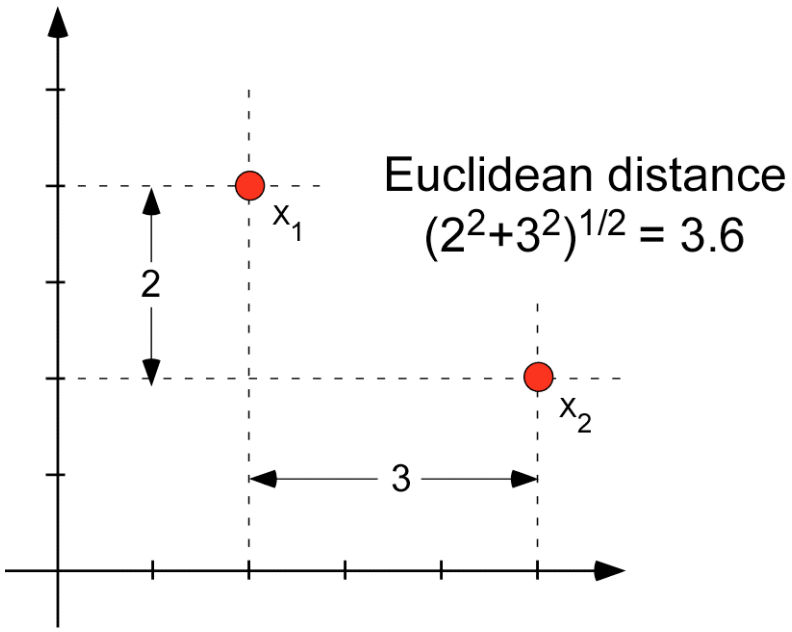

Figure 2-4. Euclidean distance.
The formula for measuring Euclidean distance between objects x_1 and x_2 is shown.

The z-standardization is a linear transformation that shifts the mean and scales the data to the standard deviation, so the distribution of objects in the standardized dimension remain the same relative to each other. Also, because it uses parameter standard deviation rather than parameter minimum and maximum values, it is not overly susceptible to the effect of outliers.

Clusters can be summarized by their cluster centroid, where the centroid's location in each dimension is the average of the location of all objects in that cluster in that dimension. The compactness of a cluster can be described by its within cluster sum of squares (WCSS), which is the sum of the squares of the distances between all objects in the cluster and the centroid C of the cluster.

$$\sum_{i=1}^{N}\sum_{d=1}^{D}(i_d - C_d)^2$$

This is equal to the internal or within cluster variance multiplied by the number of objects in the cluster.

Ward's hierarchical clustering

Ward's hierarchical clustering, also known as minimum variance or error sum or squares method, is a geometric type of hierarchical agglomerative clustering (Murtagh 1985). The Ward's algorithm builds a map called a dendrogram (Figure 2-5) that quantifies the similarity between objects and clusters of objects. It begins with each object in its own cluster, where *k* (the number of clusters) equals the number of objects in the dataset, and combines the two clusters with the minimum combined increase in internal variance to generate a single cluster.

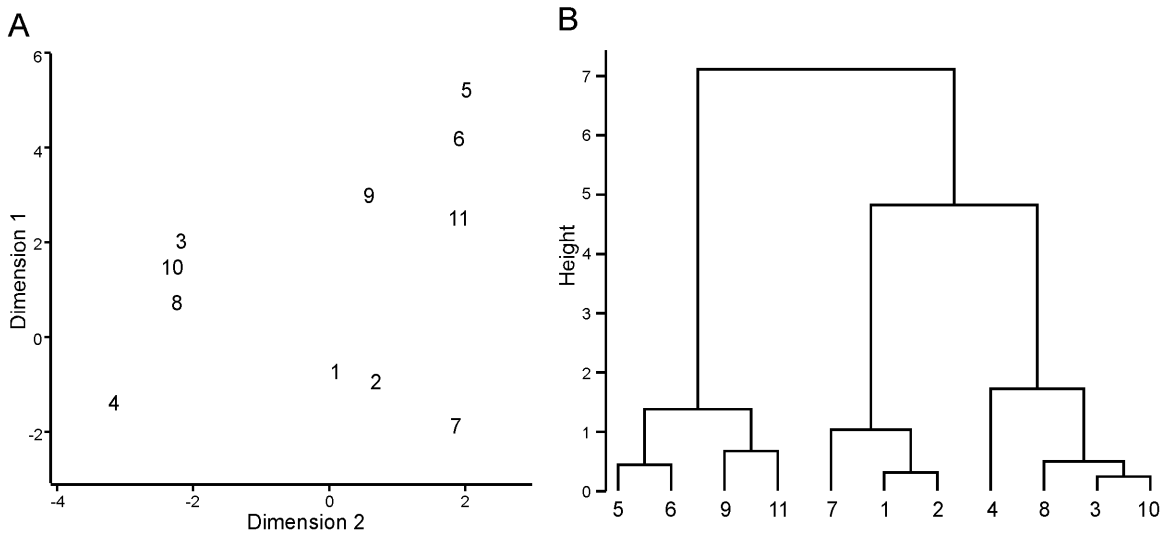

Figure 2-5. Ward's hierarchical clustering creates a dendrogram of dissimilarities between clusters.

A. Each object in this sample dataset is labeled with a unique ID.

B. The sample dataset was used to generate a Ward's dendrogram, in which the height of the horizontal line joining two clusters in the dendrogram is an indicator of distance between clusters. The objects are labeled below the dendrogram with the corresponding ID from A.

The process is repeated until all objects are in a single cluster ($k = 1$). The fusion height of the cluster being formed is the dissimilarity between the two contributing clusters. The dissimilarity can be found using the squared Euclidean distance between the contributing cluster centers g_i and g_j weighted by the number of objects in each cluster *i* and j (Murtagh 1987). In the equation below, | | means the number of objects in the cluster and || || means Euclidean distance.

$$\frac{|i| \times |j|}{|i| + |j|} \times \left\| g_i - g_j \right\|^2$$

This is equivalent to the increase in total within cluster sum of squares as a result of joining clusters *i* and *j, eg*. WCSS*i*U*j* –(WCSS*i*+WCSS*j*), where *i*∪*j* means the set formed by the union of *i* and *j*. The fusion height is in arbitrary units (a.u.), as it measures distance between standardized parameter measures. At each merge point, the cluster merge that minimizes within cluster variance also maximizes between cluster variance.

The dendrogram illustrates the relationship (similarity) between objects and clusters of objects by the order in which they merge, and the absolute and relative height of that merge (Figure 2-5). More similar objects or clusters of objects (Figure 2-5) are merged together lower down on the dendrogram, and very different clusters merge farther up the dendrogram. The relationship among objects in a cluster is described by the absolute fusion height (the height of the horizontal link merging two clusters), and by the difference between the cluster fusion heights of the cluster formed and the two contributing clusters. A larger absolute fusion height means that the objects in that cluster are more heterogeneous. A larger difference between the fusion height of the formed and contributing clusters indicates that the contributing clusters are more distinct from each other while a smaller distance suggests that the three or four cluster being merged are separated by similar distances.

The algorithm requires a dissimilarity matrix as input, so normalized variables were used to generate a dissimilarity matrix based on Euclidean measures (R function *dist*). A dissimilarity matrix is an n by n matrix where n is the number of objects being compared, and each entry in the matrix gives the dissimilarity between the indexed objects. In this case the dissimilarity is the squared Euclidean distance between the two objects. The dissimilarity matrix was entered into Ward's hierarchical clustering algorithm (R function *hclust*). The algorithm is based on Murtaugh's clustering algorithm (Murtagh 1987), and proceeds along the following steps:

1. Agglomerate
   a. create list of nearest neighbors from the dissimilarity (distance) matrix
   b. find the minimum dissimilarity (shortest distance) between clusters
   c. merge the two clusters.
   d. decrease the tally of the total number of clusters by 1.

2. Update distance matrix with distances to the newly formed cluster.
   The updating algorithm uses the Lance and Williams dissimilarity update formula with α_i, α_j, and β variables specific to the Ward's method. The formula with Ward's α_i, α_j, and β variables inserted is shown below, with the following definitions; the new cluster is defined as the union of dissimilarities *i* and *j,* or *i* U *j*. while the other cluster for which the distance is being calculated is *k*. *d* is the dissimilarity between the two clusters separated by a comma, and | | is the number of objects in that cluster.

$$d(i \cup j,k) = \frac{\left(|i| + |k|\right) \times d(i,k) + \left(|j| + |k|\right) \times d(j,k) - |k| \times d(i,j)}{|i| + |j| + |k|}$$

3. Repeat until n-1 agglomerations are complete.

Note that the entire hierarchical clustering is performed on dissimilarities, and that the Ward's algorithm updates the dissimilarities for each new cluster formed.

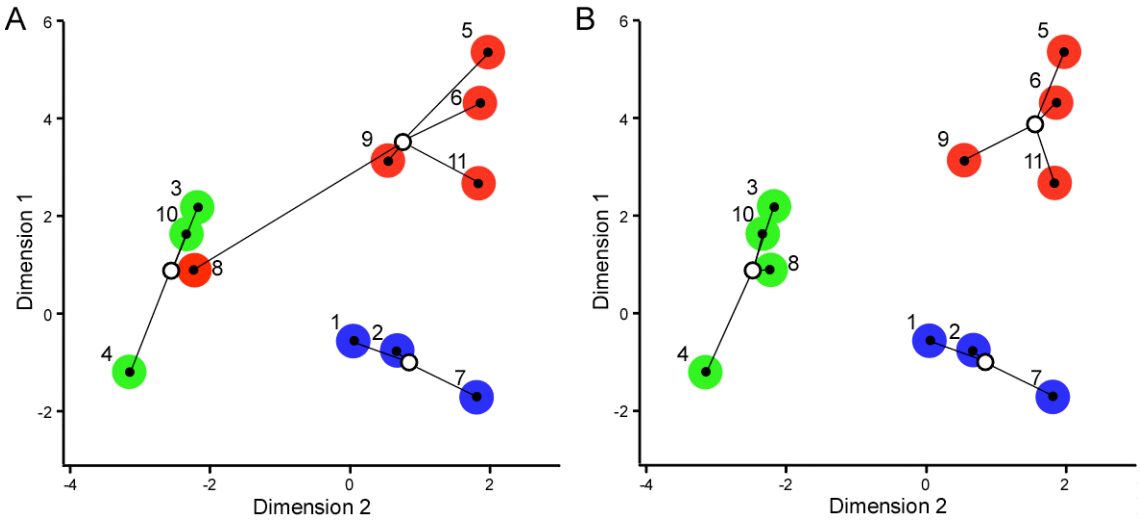

Figure 2-6. K-means clustering algorithms move objects between clusters until no single move remains that further minimizes within cluster sum of squares.
In this example, *k* is set to 3. Numbered objects have two dimensions, and belong to one of three clusters: red, green, or blue. Each object in a cluster has a line drawn to the cluster center, or mean.
A. Object 8, which belongs to the red cluster, is being evaluated in this step of the algorithm.
B. Object 8 is switched from the red to the green cluster, minimizing the total within cluster variance.

K-means

K-means is an iterative partitioning algorithm that seeks the minimum totaled within-cluster variance for k clusters by moving objects between clusters (Hartigan and Wong 1979; Telgarsky 2010). The number of clusters *k* is a required input set by the experimenter, and is fixed for any given implementation of the k-means algorithm.

The k-means algorithm starts with a random assignment of the objects into the specified number of clusters *k*,. Each object is labeled and color coded according to the cluster number assigned to it. In each iteration, each object is evaluated with each cluster and is moved to or retained in the cluster that minimizes the total of the within cluster sum of square distances. The algorithm continues to cycle through the objects until it reaches the local optimum solution identified by the algorithm, in which no single move would further reduce the total within cluster variance In the example illustrated in Figure 2-6 for the same sample dataset shown in Figure 2-5, only one final step is required to reach the local optimum, shown in Figure 2-6B. In Figure 2-6A, at the start of the step object 8 belongs to the red cluster, but when the distance to each cluster is evaluated, object 8 is closer to the green cluster, and so algorithm moves it to the green cluster, minimizing the total variance of the clusters.

The k-means clustering algorithm *kmeans* was from the statistical package R (R Development Core Team 2005). With initialization parameters set to 100 starts, 100 maximum iterations and the 'Hartigan-Wong' algorithm (Hartigan and Wong 1979) for implementation, the algorithm proceeds as follows:

1. For each object, find the closest and second closest cluster centers, and assign the object to the closer center.
2. Update all the cluster centers to be the average of the objects in them.
3. Optimal Transfer OPTRA stage.
   Use the following equation to find R1, the weighted distance between object 1 to L1, the cluster currently containing I, where NC is the number of points in the

given cluster and D is the Euclidean distance between I and the *L1* cluster center.

$$R1 = \frac{NC(L1) \times D(I,L1)^2}{NC(L1) - 1}$$

Then use the following equation to find the weighted distance from object I to each other cluster L, and set R2 to be the minimum found, and L to be the cluster giving the minimum.

$$R2 = \frac{NC(L) \times D(I,L)^2}{NC(L) + 1}$$

If R2 < R1, switch *i* to L and update cluster centers.

4. Quick Transfer QTRAN stage
   For each object *i*, compute R1 for the current cluster and R2 for the closest cluster. If Value R2 < R1, switch *i* into the other cluster and update the cluster centers.
5. If no transfer in the last M steps where M is the number of objects, go to step 6, otherwise go to step 4, repeat up to set number of iterations (100).
6. When local minimum is reached, save the cluster information along with the start number and the sum of within cluster sum of squares.
7. Repeat according to preset number of starts (100), then find the solution with the lowest total within cluster sum of squares.

Additional iterations before step 6 do not change the outcome. The Hartigan-Wong algorithm finds the local optimum, which means that no movement of a single object will decrease the within cluster sum of squares (WCSS) for any cluster. However, an entirely different partition could result in a smaller WCSS. It is for this reason that the k-means is restarted multiple times (here, 100 times), allowing for 100 different random starts to encounter a different, more optimal, partition.

Comparing Ward's and k-means algorithms

Ward's algorithm is agglomerative, starting with every object in its own cluster and at each step merging the nearest clusters, whereas k-means partitions by randomly assigning objects to clusters and moving individual objects to minimize within cluster variance. In Ward's method, cluster memberships are fixed once assigned, whereas k-means can move an object out of a cluster if it is no longer similar to other cluster members. The permanent assignment of

Ward's clusters enables Ward's to yield significantly more information on relationships between objects, especially via the construction of a dendrogram. The flexibility of k-means enables it to optimize the results, although since the k-means finds only a local minimum variance, more optimal solutions might exist. However, this limitation is reasonably well addressed by using multiple starts in k-means as is done here.

Another limitation of k-means is the requirement for the number of clusters *k* to be set as an input. K-means was therefore run for a range of possible *k* and the cluster assignments aligned by similarity and compared. This converted a weakness into an informational asset, as clusters present over multiple *k* were validated while other less stable clusters divided or moved.

Both Ward's and k-means use the whole cluster for distance measures, so both are better at detecting certain kinds of clusters than others. Both Ward's and k-means algorithms are ideal for compact, spherical clusters like those on the left of Figure 2-2. On the other hand, neither one would successfully cluster data with long, thin groups like those on the right in Figure 2-2. For long chains of objects, single linkage methods would be more effective. The single linkage method finds the minimum distance from any non-cluster object to the most recently clustered object rather than the distance to the centroid of the entire cluster (Murtagh 1987).

Both Ward's and k-means algorithms produce hard clusters, meaning each object belongs to only one cluster at a time. This likely forces more than one object into a cluster to which it is not especially similar, however, it is useful for summarizing patterns in data, which is the immediate goal. Neither algorithm can accept empty variables, and neither is equipped to properly cluster categorical data (eg, stuttering, continuous firing, and bursting). However, both the Ward's and k-means algorithms are successful for a broad range of applications.

Descriptive cluster statistics

The best cut test and upper tailed t-test were used to find the optimal number of clusters in the Ward's clustering, the bootstrap test was used to find the reproducibility of the cluster arrangements, and silhouette analysis used to examine the quality of cluster separation. The average silhouette index, within and between cluster distances, and Calinski Harabasz index were used to compare the Ward's and k-means clusters to each other.

Partitioning statistics.

The best cut test and upper tailed t-test suggest a partition – visually, a line through the dendrogram forming clusters at the cut points. In practice, these partitions are used to suggest clusters of interest for further examination and a possible number of clusters. Both measures analyze the fusion heights in the dendrogram looking for fusion values that are significantly larger than the rest, indicating that the clusters being joined are very different. The best cut test uses the formula

$$bestcut = mean(fusions) + 1.96 * stdev(fusions)$$

where *fusions* is the set of all fusion heights in the Ward's dendrogram (McGarry et al. 2010). The upper tailed t-test looks for fusion heights significantly greater than the mean of all fusion heights whose test statistic exceeds the critical value for $\alpha = 0.05$.

Bootstrapping.

In general, bootstrapping is a method for estimating a sampling distribution based on a single sample. This estimate can then be used to evaluate the likelihood of a given cluster occurring when repeated samples drawn from the same population. Since hierarchical clustering is deterministic, there is only one cluster arrangement for a given dataset. Thus bootstrapping gives an indication of how sensitive the clusters created are to variances in the dataset.

Bootstrapping of the dendrogram was performed using R function *pvclust* from the *pvclust* package for R (Suzuki and Shimodaira 2009). Each cluster found in the data is accompanied by a value (approximately unbiased, or a.u.) representing the probability that the cluster is not formed by chance (100 would be a perfectly reproducible cluster). The pvclust algorithm varies the sample size of a replicated dataset (based on the observed dataset) and the data on the resulting clusters is collected to create a distribution of clusters in that geometric region. The actual cluster can then be compared against this pattern to get an estimate of likelihood or stability. In this dissertation the a.u. values are used for their absolute confidence, and to compare the stability and likelihood of clusters.

Silhouette analysis.

Silhouette analysis (Rousseeuw 1987) evaluates clustering based on the distance from each object to its own cluster compared to the nearest different cluster, and plots the index for all objects. Silhouette analysis was implemented using the R function *silhouette*. The silhouette index is calculated for each object in the dataset *i*:

$$\frac{b(i) - a(i)}{\max\{a(i), b(i)\}}$$

A is the cluster containing *i*, and B is the nearest cluster to *i*, identified as the cluster with the minimum average dissimilarity to *i*, a(*i*) is the average dissimilarity of *i* to all other objects in A, and b(*i*) is the average dissimilarity of *i* to all objects in nearest cluster B. The two statistics a(*i*) and b(*i*) are similar to R1 and R2 used in the k-means algorithm in that both are measures of separation between object *i* and the two nearest clusters. The difference is that R1 and R2 find the weighted variance to the cluster mean, and a(*i*) and b(*i*) find the average of variances between the object and each individual point in the cluster. Note that the cluster mean includes object *i* for cluster A

The silhouette index and the silhouette plot provide a useful visual representation of the cluster configuration, revealing the degree to which objects are proximal to the cluster they are in compared to the nearest cluster. Silhouette analysis can also highlight clusters of objects in which the objects fit poorly with each other and are apparently clustered by exclusion from other clusters. For these reasons silhouette plots indicate the quality of an individual cluster and can also point to the natural number of clusters present.

Comparing clusters.

To compare Ward's and k-means cluster results, I used the average silhouette index, the average within cluster distance, the average between cluster distance, and the Calinski Harabasz index. The R *cluster.stats* function from the *fpc* package (Hennig 2010) was used to generate metrics. The average silhouette index is the average of all object silhouette indices. The within cluster distance is an index of how tightly objects are grouped in the center of a single cluster, so the average is an index for cluster tightness in that cluster configuration overall. The average between cluster distance is an index of how well separated the clusters are. The Calinski Harabasz index (Calinski and Harabasz 1974) is proportional to the ratio of the sum of the squared distances between each cluster mean and the dataset mean $\bar{x}$, to the sum of the squared within cluster distances, adjusted for the size of the dataset N and the number of clusters *k*, i.e.:

$$\frac{\sum_{l=1}^{k} N_l \left(\bar{x}_l - \bar{x}\right)^2}{\sum_{l=1}^{k}\sum_{i=1}^{N_l} \left(x_l(i) - \bar{x}_l\right)^2} \times \frac{N-k}{k-1}$$

Principal Component Analysis.

Principal Component Analysis (PCA) can be used to reduce the dimensionality (number of parameters) of a multi-parameter dataset by generating new uncorrelated variables (Murtagh 1987), which can then be used to visualize patterns or clusters in the data.

PCA uses linear algebra to provide a new coordinate system where the axes are orthogonal to each other and are ordered by the amount of variance along that axis. The axes are computed such that the first coordinate direction, or principal component, encompasses the highest variance, the second is orthogonal to the first and has lower variance and so on. If the variance is not equally spread along the new coordinate directions but instead resides in the first several axes, it suggests that much of the variance in the data can be represented by just a few principal components.

The original data is thus transformed into new variables mapped onto the new orthogonal axes, one variable per dimension per object. The location in the new dimensions, called the component score, is a factor of the location in the original dimensions weighted by the contribution of each original dimension to the new principal components. By plotting the component factors from the first two or three principal components against each other for each object in the dataset, the data can be examined for natural patterns or clusters. Labeling this plot by cluster membership allows the clustering efficacy to be visualized.

CHAPTER 3: CLUSTERING DISTINGUISHES PV AND SOM INTERNEURON SUBGROUPS

ABSTRACT

PV and SOM interneurons are two major groups of inhibitory interneurons that differ in multiple features including morphology, synaptic connectivity, and input response. These features enable PV and SOM interneurons to play different roles in the cortical circuit, including different computational functions. PV and SOM interneurons are readily distinguished based on passive and active membrane properties as well as axonal morphology. Historically this has been done subjectively, but more recently PV interneurons have been distinguished from other inhibitory interneurons including SOM using unsupervised clustering methods. A combined dataset of parameters describing passive and active membrane properties from PV and SOM interneurons were therefore used to validate an unsupervised clustering protocol. The protocol uses Ward's hierarchical and k-means clustering along with descriptive clustering statistics to find groups of interneurons sharing similar features. Clustering using passive and active membrane parameters effectively separated PV and SOM interneurons into different groups with a low error rate. These results suggest that, applied to a dataset of passive and active membrane properties from PV interneurons, the clustering protocol is capable of identifying subgroups sharing similar features.

INTRODUCTION

Inhibitory interneurons can be classified based on morphology, membrane properties, and molecular markers, among other qualities. The calcium binding protein parvalbumin (PV) is expressed in 40% of all inhibitory interneurons, and does not overlap with expression of the neuropeptide somatostatin (SOM), present in 20% of all inhibitory interneurons (Gonchar et al. 2007; Kawaguchi and Kubota 1998; Xu et al. 2010). PV interneurons are typically multipolar, soma targeting large basket cells with low membrane resistance and a fast spiking, non-accommodating firing pattern. In contrast, SOM interneurons are typically bitufted, dendrite targeting Martinotti cells with a rapid spiking, adapting, accommodating firing pattern (Cauli et al. 2000; Kawaguchi and Kondo 2002; Kawaguchi and Kubota 1998).

Firing patterns are commonly used to identify and distinguish PV and SOM interneurons, and have been used in unsupervised clustering to classify them into separate groups (Cauli et al. 2000). An effective clustering protocol should be able to separate PV from SOM interneurons, making a combined dataset of PV and SOM interneurons a useful test of a clustering protocol.

This chapter describes in detail the methods of data collection, analysis, and clustering which successfully separated PV from SOM cells in a combined PV and SOM dataset, and which are then applied to a PV dataset in chapter 4 to look for PV subgroups. This chapter thus should be seen as a methodological validation of the PV clustering procedure and results.

PV and SOM interneurons in cortical networks

Differences between PV and SOM interneurons go beyond morphology and physiology to circuit connectivity and computational role. PV and SOM interneurons in layers 2/3 both receive excitatory input from local layers 2/3 pyramidal neurons, but additional input also comes from layers 4 and 5 (Dantzker and Callaway 2000; Xu and Callaway 2009) as well as excitatory

inter-cortical projections (Gonchar and Burkhalter 2003). PV interneurons receive a greater number of inter-cortical inputs than SOM interneurons (Gonchar and Burkhalter 2003). Laminar synapses onto PV interneurons are minimal and distributed across distal dendrites, while inter-cortical axons terminate in large synapses proximal to the soma (Buhl et al. 1997; Krimer and Goldman-Rakic 2001).

PV interneurons are preferentially recruited by a brief stimulus because the input is large and reliable, but undergoes short-term depression (Reyes et al. 1998; Thomson 1997; Watanabe et al. 2005). Conversely, excitatory input onto SOM interneurons is initially small with a high rate of failure, but undergoes strong short-term synaptic facilitation (Reyes et al. 1998; Thomson 1997; Watanabe et al. 2005). Therefore, in the presence of sustained stimuli, an initial strong PV mediated inhibitory signal would drop out and be replaced by SOM mediated inhibition. A complex signal arriving at a pyramidal neuron in layers 2/3 thus encounters its first differential filter at the pyramidal to inhibitory interneuron synapse.

Leaving the interneuron, the signal encounters another differential filter - PV interneurons preferentially target and inhibit perisomatic regions of their postsynaptic target, while SOM interneurons target distal dendrites (Kapfer et al. 2007). The sum of differences in synaptic input, membrane properties, and targets of synaptic output makes SOM interneurons modulate discrete circuit connections, while PV interneurons broadly modulate pyramidal output (Burkhalter 2008) A sustained complex signal going through the PV and SOM filters will emerge as an early, strong, higher frequency but generalized inhibitory signal which later turns into a weak, lower frequency but very specific inhibitory signal (Burkhalter 2008).

A high degree of synaptic and electrical interconnectivity within inhibitory interneuron classes enable synchronization of inhibitory interneuron firing rates and local up or down states

of excitability (Gibson et al. 1999; Helmstaedter et al. 2009; Hestrin and Galarreta 2005). PV interneurons in the cortex form strong electrical connections with other PV interneurons (Hestrin and Galarreta 2005). In layers 2/3 of the visual cortex, over 80% of PV interneuron pairs examined were interconnected and connectivity remained consistent over maturation from 14 to 42 days post natal (Meyer et al. 2002). These properties make PV interneurons a major driver of gamma oscillations (30-80 Hz) in the cortex (Cardin et al. 2009), and SOM interneurons may underlie slower theta rhythms (3-10 Hz) (Fanselow et al. 2008), as reviewed in (Whittington and Traub 2003). Super-cellular oscillation such as gamma or theta waves select for inputs of the same frequency by increasing the signal to noise ratio.

Hence, PV and SOM interneurons may serve as differential signal filters, amplifiers, and processors in the cortex.

MATERIALS AND METHODS

Animals

We took advantage of several transgenic mouse lines in which PV or SOM expressing interneurons are fluorescently labeled. Two transgenic mouse lines were used to identify PV interneurons in visual cortex: B13 and PV-tdTomato. B13 mice (Dumitriu et al. 2007) were generated from a bacterial artificial chromosome (BAC) clone in which EGFP cDNA and the phosphoglycerate kinase polyadenylation sequence were inserted at the translation initiation codon of a PV clone, resulting in EGFP expression driven by the PV promoter. B13 mice were used as heterozygotes in a C57Bl/6 background. About 50% of PV-positive interneurons in B13 mice express GFP (Akgul and Wollmuth 2010; Dumitriu et al. 2007). PV-tdTomato (PV-Cre; LSL-tdTomato) mice were generated by the Cre/loxP based strategy. PV-Cre mice (Hippenmeyer et al. 2005; Kuhlman and Huang 2008) in which Cre recombinase expression was

driven by a PV promoter (an IRES-Cre-pA cassette inserted at the 3' end of the PV gene) were crossed with the LSL-tdTomato line (B6;129S6-Gt(ROSA)26Sor$^{tm9(CAG-tdTomato)Hze}$/J from Jackson Labs, donator: Allen Brain Institute) in which tdTomato expression was activated upon the excision of a lox-flanked STOP cassette upstream of the tdTomato gene following Cre-mediated recombination. PV expression begins around P14, and tdTomato expression follows. By adulthood, greater than 95% of PV expressing cells express tdTomato and all tdTomato cells express PV (Akgul and Wollmuth 2010; Hippenmeyer et al. 2005; Kuhlman and Huang 2008).

The GIN strain was used to identify SOM interneurons. GIN mice carry a transgene containing a GAD1 regulatory domain upstream of an EGFP gene, resulting in EGFP fluorescence in a subset of somatostatin expressing interneurons (Oliva et al. 2000). GIN mice were founded by a FVB wild type and FVB/N albino mutant cross, and were maintained and used as homozygotes.

Solutions

The artificial cerebral spinal fluid (ACSF) solution used for recordings consisted of (in mM): 125 NaCl, 2.5 KCl, 25 glucose, 25 $NaHCO_3$, 1.25 NaH_2PO_4, 2 $CaCl_2$ and 1 $MgCl_2$, and was saturated with 95% O_2/ 5% CO_2 under all conditions. EPSCs were recorded in the presence of $MgCl_2$ unless otherwise indicated. All pharmacological agents were added to the external solution without substitution. The standard internal solution was an ATP generating internal (AGI) solution containing (in mM): 105 K-gluconate, 30 KCl, 3 $MgCl_2$, 10 HEPES, 10 phosphocreatine, 4 Mg-ATP and 0.3 GTP, pH 7.3 (KOH), and adjusted to 305 mOsm with sucrose.

Acute slice preparation

Mice between postnatal day 15 (P15) and day 20 (P20) were anesthetized with isofluorane and then decapitated in accordance with the institutional animal ethics committee and in keeping with guidelines established by the National Institute of Health. The brain was dissected out in ice-cold ACSF solution with added kynurenic acid (200 μg/mL). Coronal slices were collected from each blocked hemisphere using a vibratome (Sigmann electronic, Hüffenhardt, Germany). Slice collection began 1.0 mm rostral to the caudal cortical surface, and yielded four 300 μm slices. Slices were placed into oxygenated ACSF at 32°C for 15 minutes then left undisturbed at room temperature for another 40 minutes before use.

Electrophysiology

Membrane potentials or currents were recorded at 32 - 34 ˚C using an EPC 10 USB amplifier with PatchMaster software (HEKA Elektronik, Lambrecht, Germany). Recordings were sampled at 20 kHz and low pass filtered using a 4-pole Bessel filter at 10 kHz. Pipettes had resistances of 2-4 MΩ when filled with internal solution and measured in the ACSF bath. External solutions were bath applied at a perfusion rate of approximately 3 mL/min. Membrane potentials were not corrected for liquid junction potentials.

Targeting neurons.

I initially identified layers 2/3 in relation to the pial edge of the slice, and targeted the visual cortex using the lateral ventricle size and shape as a reference. I then visually identified the interneurons by searching for EGFP or tdTomato expression under magnification (Olympus BX50WI fitted with a x 40-W/0.80 NA objective, and cooled CCD camera Quantifire XI from Optronics).

Experimental Protocols

Passive and active membrane properties.

Upon achieving the whole cell mode, resting membrane potentials (V_m) were measured in current clamp. The amplifier mode was changed to voltage clamp and the baseline holding potential set to –70 mV. I placed all cells at the same membrane potential so that voltage dependent channels would be at a similar starting state and rheobase current would be independent of V_m. Pipette series resistance, neuronal membrane resistance, and neuronal membrane capacitance (C_m) were monitored at the start and regularly throughout the experiment using the LOCKIN Sine+DC protocol from HEKA (Gillis 1995), with a 20 mV (–90 to –70 mV) sine wave of 1 kHz for 100 ms. The amplifier was then switched to current clamp mode and the current adjusted to bring the reported membrane potential to approximately –70 mV. Action potentials were evoked using a series of depolarizing pulses of 1 s duration each, with 5 s between each stimulus. Depolarizing currents varied with cell type and membrane resistance but ranged from 10 pA to 1 nA. Rheobase (see below) was found by applying 10 pA increments of current.

Analysis

Passive/subthreshold membrane properties.

Resting membrane potential (V_m) was measured in current clamp upon achieving the whole-cell mode. Series resistance and membrane capacitance (C_m) were analyzed in real-time using the PatchMaster LOCKIN online analysis software. Subsequent analysis was performed using IgorPro (WaveMetrics). Membrane resistance (R_m) is the slope of a line fit to subthreshold

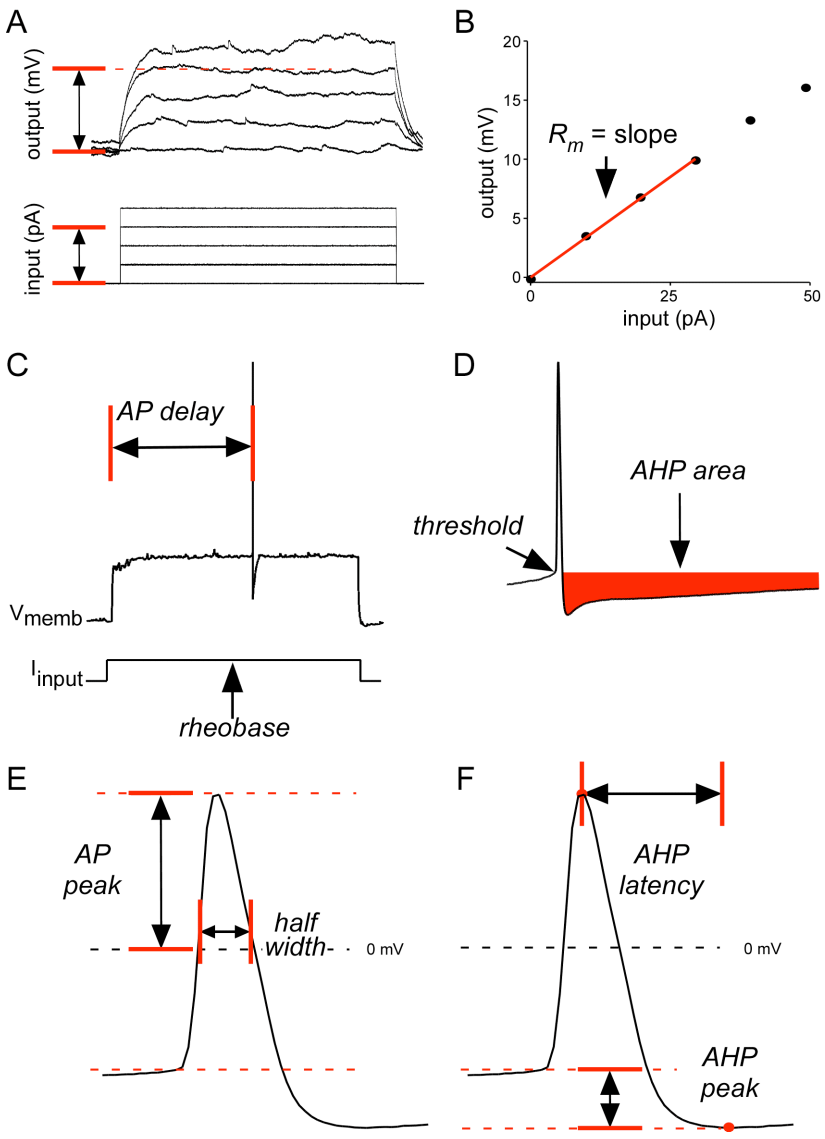

Figure 3-1. Characterization of passive and active membrane properties.
A&B. Input-output responses.
A. Input; successive depolarizing current injections one second in duration are shown in the lower traces. Output; membrane potential responses are shown above.
B. The change in membrane potential plotted against current input. A line fit to the first 10 mV of sub-threshold depolarization is overlaid in red. The slope of this line corresponds to the *membrane resistance (R_m, MΩ)*
C. The first action potential evoked using a series of depolarizing pulses was selected for further analysis. The current required to evoke this first action potential is the *rheobase*, and the *AP delay* is measured from the start of the depolarizing stimulus to the peak of the AP.
D. *Threshold* is found using the third derivative to find the point where the slope of the depolarizing phase of the first action potential (C) is changing most rapidly. Recovery from afterhyperpolarization (*AHP area*) is measured as the area under a line defined by the threshold voltage.

E. The depolarized portion of the action potential can be described by AP amplitude and half-width. *AP peak* is measured from 0 mV to AP peak. *Half-width* is measured at 1/2 the difference between threshold and AP peak.
F. *AHP latency* is the time elapsed between maximum AP and minimum AHP potentials. *AHP peak* is measured from threshold to minimum potential reached.

voltage responses to current input (Figure 3-1A+B). Rheobase is the minimum current input over a one second stimulus that generates an action potential (Figure 3-1C).

Active/action potential shape.

The first action potential evoked by the rheobase current was used to characterize action potential (AP) shape. AP threshold was determined by the third derivative of the action potential found over the AP rising phase (Figure 3-1D). Smoothing of the AP waveform was performed after each derivative. AP peak and half-width were used to describe the rising and falling phases of the AP (Figure 3-1E). AP peak is the absolute maximum amplitude. Half-width was measured as the time from the rising phase to the falling phase of the AP at 1/2 the distance from threshold to peak. After hyper-polarization (AHP) was characterized by the AHP peak, latency, and area (Figure 3-1D+E). AHP peak is the difference between threshold and maximum after-hyperpolarization. AHP latency is the time from AP peak to AHP peak. AHP area is the area under a line defined by the AP threshold membrane potential.

Active/firing pattern.

The delay to onset of the 1st AP is measured from the start of a depolarizing stimulus pulse to the peak of the first AP evoked in response to rheobase (Figure 3-1C). AP firing patterns, as outlined below, were analyzed in the trace that contained around 30 APs, e.g. fired APs at 30 Hz, the low range of the gamma frequency (Jagadeesh et al. 1992; Steriade et al. 1996) (Figure 3-2A). In some cases the firing frequency jumped from no or a few APs to frequencies much higher than 30 Hz. In these cases, analysis of firing patterns were analyzed on the first available trace over 25 Hz. AP amplitude accommodation was measured as amplitude change (Δamplitude) – the amplitude of the first peak minus the last peak (Figure 3-2A). Interspike interval (ISI) was measured as the time between successive AP peaks (Figure 3-2A). Spike

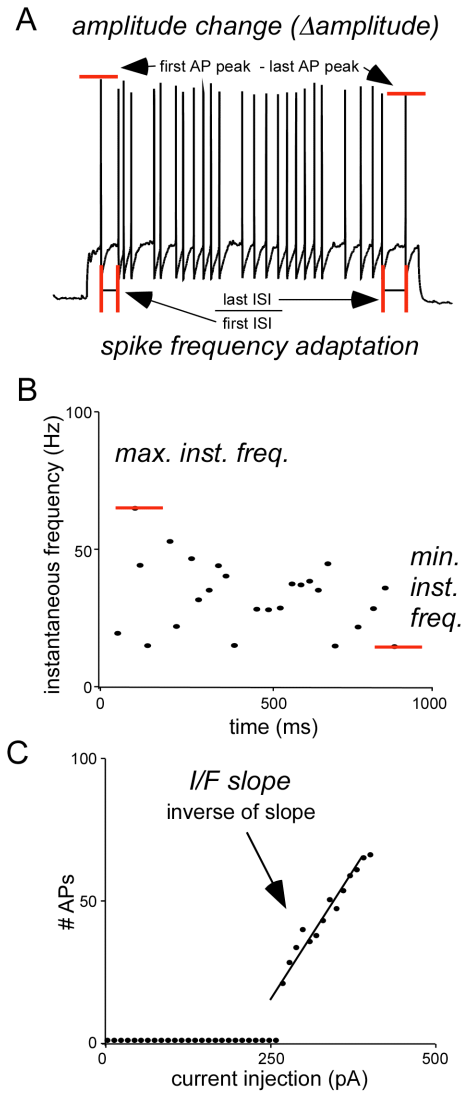

Figure 3-2 Characterization of action potential patterns.
A. The first trace to exhibit 30 APs (or the closest possible trace) is used to calculate AP *amplitude change (Δamplitude)* and *spike frequency adaptation*.
B. The instantaneous frequency plotted against time, scaled and aligned with AP firing trace above (B). *Maximum and minimum instantaneous frequency* measurements are the maximum and minimum instantaneous frequencies derived from the 30 AP trace as shown.
C. Number of APs generated during a 1s depolarization plotted against the amplitude of current injected. A linear fit describes the input response F/I of the interneuron. *I/F slope* is the inverse of the slope of the fit.

frequency adaptation was measured as the last ISI divided by the first ISI (Figure 3-2A). Instantaneous frequency of AP_x is the inverse of the interspike interval (in seconds) AP_x to AP_{x+1}. Maximum and minimum instantaneous frequencies are the maximum and minimum instantaneous frequencies detected in the 30 AP trace (Figure 3-2B). The coefficient of variation (CV) of the firing rate (CV frequency) is the standard deviation of the frequency divided by the average frequency. Input-output response (I/F slope) is measured as the slope of a line fit to a plot of the number of evoked action potentials versus current input (Figure 3-2C). Histograms showing the distribution of data in 6 parameters are shown in Figure 3-3.

Cells were included in analysis only if the neurons showed rapid or fast-spiking behavior, had resting membrane potentials < -57 mV, and had a stable baseline.

Parameter selection

Multi-dimensional cluster analysis was performed on passive and active membrane properties to separate PV from SOM interneurons**.** For clustering, I focused on 16 parameters that were largely unrelated. Figure 3-4A is a cross-correlation matrix of these 16 parameters with correlation indices color coded, with black being perfectly correlated (correlation index of 1.0) and white being perfectly uncorrelated (correlation index of 0). Most parameters are not strongly correlated (e.g. threshold & AP peak). However, some parameters were correlated (correlation coefficient > 0.6) (R_m & rheobase; AP half-width & AHP latency; ISI average & minimum frequency; minimum frequency & CV frequency) but were both retained because they encompass different features of membrane properties. For example, AP half-width is correlated to AHP latency because they both encompass the rate of AP decay; however, AP half-width also encompasses AP duration whereas AHP latency describes the rate of after-hyperpolarization.

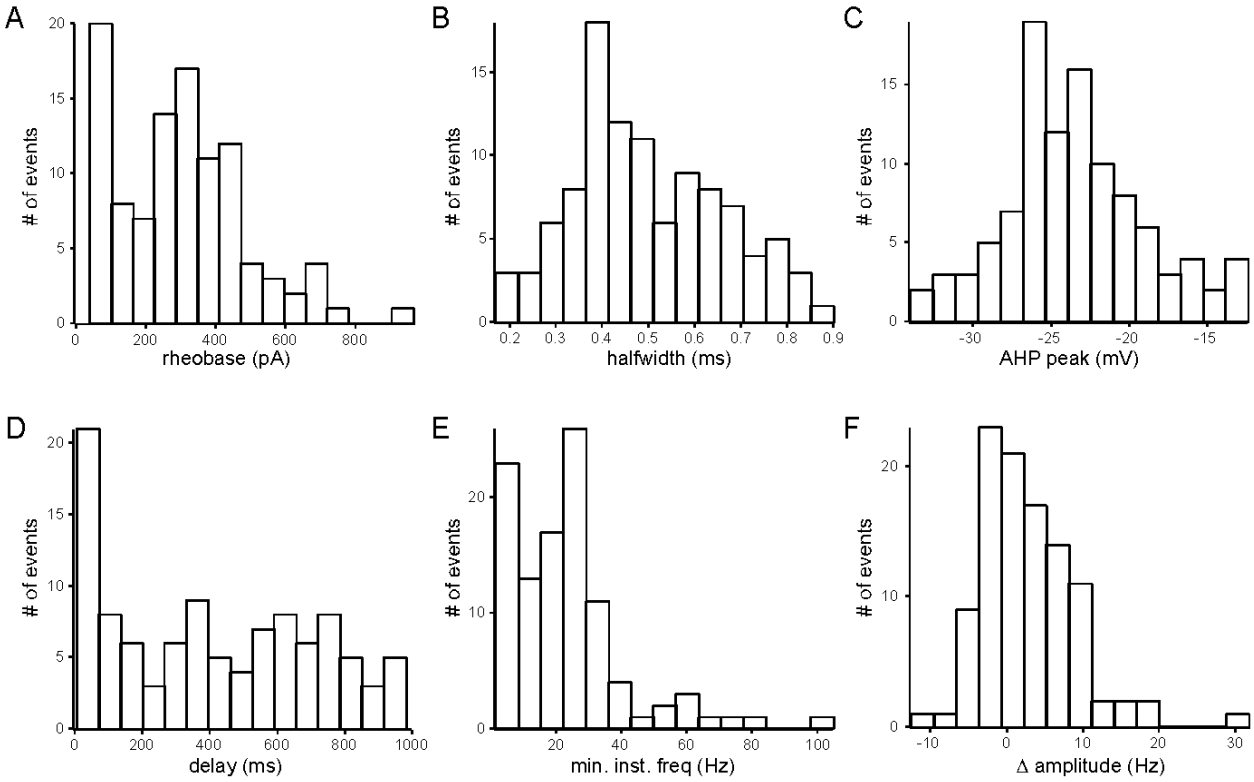

Figure 3-3 Distribution of data in the combined PV and SOM dataset.
A, B, C, D, E F. Data is plotted for parameters describing rheobase (A), halfwidth (B), AHP peak (C), delay to first AP (D), minimum instantaneous frequency (E), and change in amplitude (F). The bin size set to form 15 bins to cover the range of data.

Although the AHP shape in SOM interneurons is distinct compared to the AHP shape in PV interneurons (SOM AHP is typically multiphasic, compared to a simple mono or biexponential recovery in PV AHPs), this feature was not adequately captured in the parameters. I therefore did not use AHP area for classification.

I also performed PCA on the 16 parameters to reduce the dimensionality. Figure 3-4B shows the eigenvalues associated with the resulting principal components (PC) along with the proportion of the total variance accounted for by that PC. The first five eigenvalues are greater than one, indicating they contribute more to the variance of the dataset than any one the original parameters. Together the first five PCs account for 74% of the variance in the dataset and 9 PCs are required to reach 90% of the variance. PCA is most useful when it can identify two or three PCs to describe most of the variance in a dataset, therefore I did not use PCs for clustering. Instead, the 16 original parameters were used for clustering, accompanied by a unique id assigned to each cell.

RESULTS

PV and SOM interneurons have been previously characterized and are widely regarded as distinct non-overlapping interneuron subgroups (Gonchar et al. 2007), and an effective sorting procedure should correctly distinguish PV from SOM interneurons. The passive and active membrane and firing pattern characteristics of fluorescently labeled interneurons recorded in B13 or PV-tdTomato (PV) and GIN (SOM) mouse strains should provide an ideal dataset with which to test the effectiveness of a clustering procedure, if the B13, PV-tdTomato, and GIN fluorescent-positive interneuron sample is consistent with previously described PV and SOM interneurons.

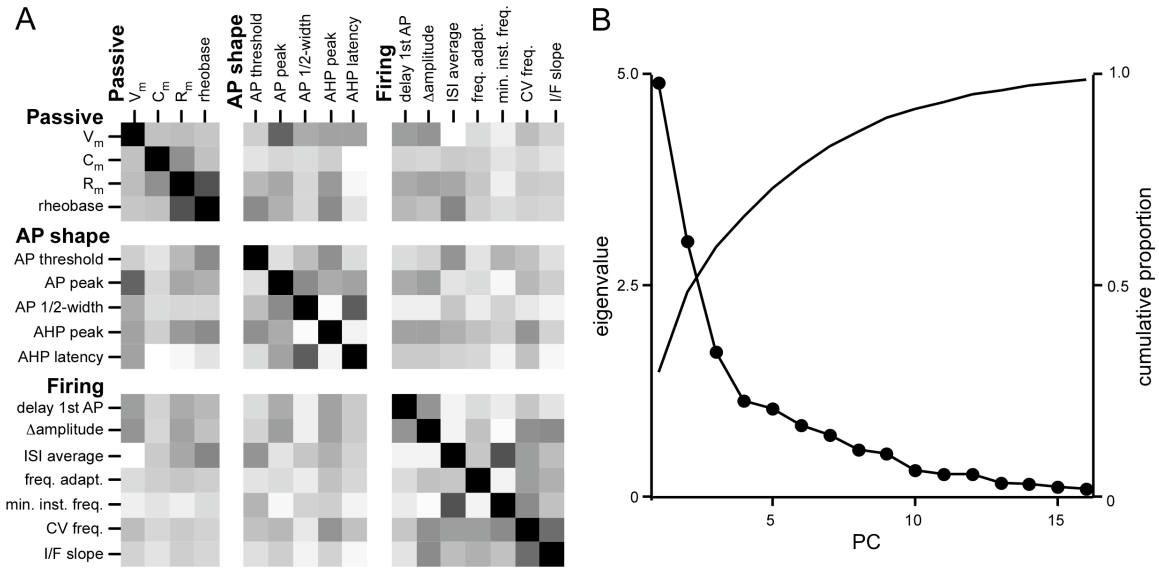

Figure 3-4. Correlation of parameters describing membrane properties of pooled PV and SOM interneurons.

A. The 16 passive and active membrane properties used for clustering (derived from 104 interneurons) are arrayed against each other in a correlation matrix with the degree of correlation indicated by the shading, white is uncorrelated (correlation index of 0) and black is perfectly correlated (correlation index of 1, diagonal squares).

B. Principal component analysis does not greatly reduce variance. For each principal component (PC) derived from the 16 interneuron membrane properties in A, the variance explained by that PC (eigenvalue, solid circles), and the cumulative proportion of variance explained by all principal components up to and including that PC (cumulative proportion, line) are plotted.

PV and SOM interneuron characteristics in visual cortex layers 2/3

PV.

A representative PV recording is shown in Figure 3-5A and C, while frequency and input output plots are shown in E and G. Averaging across all PV cells (Table 3-1), resting membrane potential is –77 ± 1 mV (mean ± SEM, n = 85), membrane resistance is 130 ± 85 MΩ (Figure 3-5 E, upper panel), and capacitance is 19.6 ± 0.4 pF. PV interneurons require 356 ± 18 pA to fire (rheobase) in response to 1 second stimulus. The AP threshold is –35 ± 1 mV, and AP peak is 19 ± 85 mV. Action potentials take 0.51 ± 0.02 ms at half maximum amplitude, and 2.13 ± 0.14 ms to repolarize from AP peak to AHP minimum. PV interneurons reach an AHP peak of 24.9 ± 0.4 mV.

At the rheobase current input, PV interneurons fire an action potential at a delay of 485 ± 31 ms. PV AP amplitudes are non-accommodating with an average change from 1st to last AP peak of 1.12 ± 0.52 (Table 2-1). Action potential firing patterns are also non-adapting - the ratio of the last inter spike interval (ISI) to the first ISI is 1.05 ± 0.14 (Table 3-1). Maximum instantaneous frequency at 30 Hz is 60 ± 3 Hz and minimum instantaneous frequency is 23 ± 2 Hz. On an I/F plot of # of APs versus current input (Figure 3-5G), the slope of the steep phase reveals the current required for each additional action potential - on average 1.84 ± 0.15 pA.

The passive and active properties of PV interneurons measured in this sample pool are consistent with previously described PV interneurons (Table 3-2), with most parameter means falling in the same range. Of those parameters with means outside of the range illustrated in Table 3-2, only the onset of 1st AP seems markedly different. This is likely because of the longer (1 second) test pulse used in this protocol.

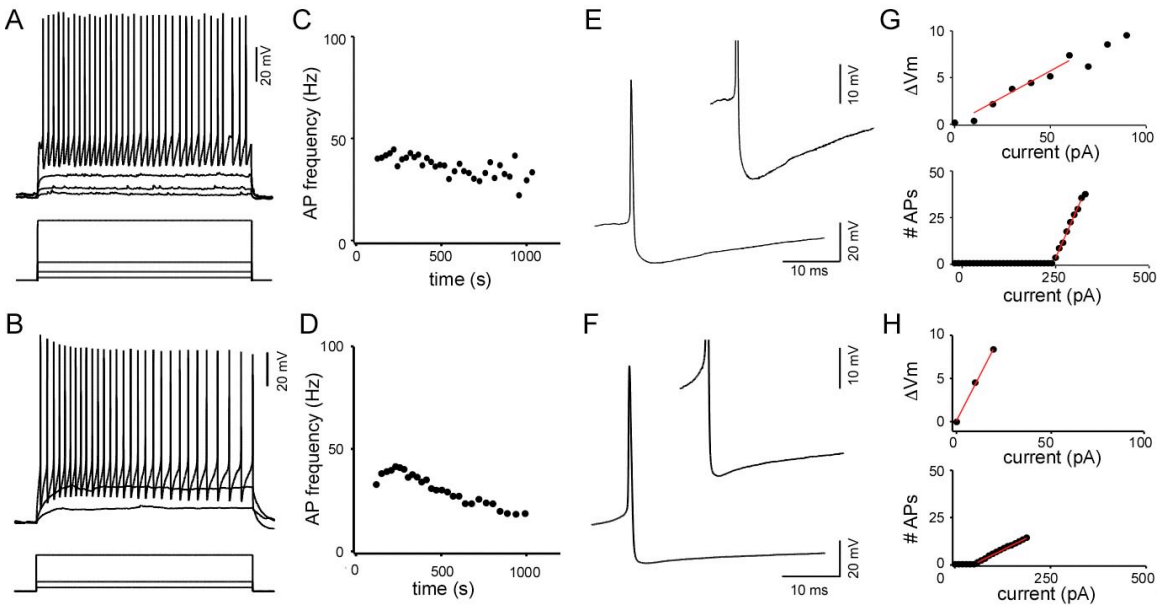

Figure 3-5. Active membrane properties of PV and SOM interneuron subtypes in layers 2/3 of the visual cortex.

Action potentials were recorded in GFP-positive cells in B13 (ACEG) and GIN mice (B,D,F,H).

A. Depolarizing currents of 1 second duration were injected into a PV interneuron current-clamped at approximately –70 mV. 20, 50, 100, and 320 pA current injections are shown. With 320 pA the interneuron fired action potentials at a steady frequency of 35 Hz.

B. Depolarizing currents of 1 second duration were injected into a SOM interneuron current clamped at approximately –70 mV. 20, 50, and 190 pA current injections are shown. With 190 pA the interneuron fired action potentials that exhibited adaptation and accommodation of spike amplitude and frequency, averaging 29 Hz.

C, D. The instantaneous frequency of evoked action potentials $\frac{1000\,m\,\mathrm{sec}}{ISI\,m\,\mathrm{sec}}$, plotted against time of occurrence in PV (C) and SOM (D) interneurons.

E, F. The first super-threshold action potential scaled to 120 mV by 40 ms, and at 40 mV by 40 ms (inset) in PV (E) and SOM (F) interneurons.

G, H. Passive membrane depolarization (upper panel, ΔVm (mV) and active neuronal response (lower panel, number of action potentials) in PV (G) and SOM (H) interneurons plotted against the current input. Fits to ΔVm were applied to the first 10 mV of depolarization and forced to intersect the y-axis at the origin, while fits to number of action potentials were applied to action potential numbers greater than zero and less than forty and no y-intersect was specified.

Table 3-1. Membrane and firing properties of layers 2/3 PV and SOM interneurons.

	PV	SOM	t - test
Passive			
V_m (mV)	-77.2 ± 0.9	-63.1 ± 0.6	P < 0.001
C_m (pF)	19.6 ± 0.4	15.5 ± 0.9	P < 0.001
R_m (MΩ)	130 ± 8	303 ± 24	P < 0.001
rheobase (pA)	356 ± 18	73 ± 8	P < 0.001
AP shape			
AP threshold (mV)	-35.6 ± 1.0	-42.2 ± 1.4	P < 0.001
AP peak (mV)	18.7 ± 1.4	43.4 ± 2.5	P < 0.001
AP half-width (ms)	0.51 ± 0.02	0.44 ± 0.02	P < 0.05
AHP peak (mV)	24.9 ± 0.4	17.2 ± 0.8	P < 0.001
AHP latency (ms)	2.13 ± 0.14	1.25 ± 0.06	P < 0.01
Firing pattern			
delay 1st AP (ms)	485 ± 31	101 ± 14	P < 0.001
Δ amplitude (mV)	1.12 ± 0.52	10.0 ± 1.7	P < 0.001
ISI average (ms)	26.7 ± 0.7	32.4 ± 0.4	P < 0.001
frequency.adapt.	1.05 ± 0.14	2.54 ± 0.29	P < 0.001
min. inst. Freq (Hz)	23.4 ± 2.1	22.0 ± 1.0	N.D.
CV frequency	0.34 ± 0.04	0.17 ± 0.01	P < 0.001
I/F slope (I_{in}/#AP)	1.84 ± 0.15	4.44 ± 1.08	P < 0.05
n	85	19	

B13 and PV-tdTomato (PV) and GIN (SOM) cells are characterized by subthreshold passive membrane properties, action potential shape, and firing pattern. Values are shown as mean ± SEM. A t test was used to find statistical differences between PV and SOM, and results are reported in the right-hand column.

Table 3-2. Comparison of published PV interneuron properties with the experimental pool.

PV Interneurons	Fast spiking	Chandelier	Basket	Rat FS NPY$^+$	PV-GFP$^+$
	(Blatow 2003)	(Woodruff 2009)		(Karagiannis 2009)	
Temperature	RT	34-36 C		RT	32 C
Brain Region	Frontal, somatosensory	somatosensory		somatosensory	visual
Age (days PN)	14	15-23		17-21	15-19
Vm	-73	-81	-83	-72	-77
Threshold	-37	-39	-39		-36
Rheobase		240	539	101	356
1/2 width	0.7			0.6	0.51
Onset of 1st AP		47	195	337	485
Rm	82	129	75	206	130
Subthreshold I/V		supralinear	sublinear		mixed

Published (left) and experimental parameter values (right) for passive and active AP parameters selected based on availability in published data. Mean values are reported.

SOM.

GIN mice express eGFP under the GAD1 promoter, and all labeled cells are positive for somatostatin (Halabisky et al. 2006; Oliva et al. 2000). A representative SOM interneuron is shown in Figure 3-5 B, D, F and H. Average SOM resting membrane potentials are –63 ± 1 mV, membrane resistance is 303 ± 19 MΩ, and capacitance is 15.5 ± 0.9 pF (mean ± SEM, n=19). Low current injections were required to evoke an active response - rheobase is 73 ± 8 pA for SOM interneurons. The threshold of the first action potential is –42.2 ± 0.9 mV, AP peak is 43.3 ± 2.5, and SOM AP half-widths average 0.44 ± 0.02 ms. The membrane takes 1.25 ± 0.06 ms to repolarize from AP peak to AHP minimum, and reaches average AHP peak of 17.2 ± 0.8 mV.

The time from the start of a depolarizing current pulse to the onset of the first AP at rheobase is shorter in SOM interneurons, averaging only 101 ± 14 ms. AP amplitudes accommodate over time, the first spike peak being on average 10.03 ± 1.65 mV higher than the last peak. Action potential firing patterns show spike frequency adaptation - the last inter spike interval (ISI) is on average 2.54 ± 0.29 times longer than the first (Table 3-1). The maximum and minimum instantaneous frequencies are 69.4 ± 6.5 and 22.0 ± 0.9 Hz respectively. The I/F slope is 4.44 ± 1.08 pA/Hz.

SOM expressing neurons in this colony of GIN mice are largely consistent with both previously described GIN interneurons and other SOM interneurons (Table 3-3). The only parameter well outside the range of described amplitudes is the AP amplitude measured from threshold, which is larger in these SOM cells. This could be due to differences in sampling frequency or filtering prior to analysis.

There are significant differences between all PV and SOM passive and active membrane properties except the minimum instantaneous frequency.

Table 3-3. Comparison of published SOM interneuron properties with experimental pool.

SOM Positive Interneurons	GIN	X94 (Ma 2006)	X98	GIN (Xu et al 2006)	GIN (McGarry 2010)	GIN
Temperature		32 C		RT	RT	32
Brain region		barrel		layers 2/3 barrel	V1, S1, FC	visual
Age (days PN)		16-24		17-25	10-18	15-20
Vm	-67	-69	-68	-47	-67	-63
Threshold	-44	-43	-43	-36		-42
Rheobase	51	202	27	30	40	73
AP amplitude	58	60	63	57	59	85
1/2 width	0.55	0.45	0.74	1.17	1.7	0.44
AHP amplitude	17	18	20	9.97		17
Adaptation	1.85	1.75	1.96	2.67	1.9	2.5
Rm	282	132	514	149	441	303

Published (left) and experimental parameter values (right) for passive and active AP parameters, selected based on availability in published data. Mean values are reported for each group. Amplitude is measured from threshold.

Cluster Analysis

PV and SOM interneurons in layers 2/3 of the visual cortex in acute slices were identified by EGFP or tdTomato fluorescence and patched in the whole cell configuration. I recorded passive and active membrane properties (see Materials and Methods) from 104 interneurons (73 from PV-tdtomato, 12 from B13, and 19 from GIN mice) ranging in age from P15 to P20.

I characterized the interneuron properties using 16 largely uncorrelated parameters (Figure 3-4A and Table 3-1) (see Material and Methods) and used the 16 parameters normalized to a mean of 0 and a standard deviation of 1 for clustering analysis.

Ward's hierarchical cluster analysis suggests 2 or 4 major clusters of interneurons

Ward's hierarchical clustering (see Materials and Methods) was applied to the pooled normalized PV and SOM dataset to generate a dendrogram (Figure 3-6). Each cluster is given a unique id, shown above the horizontal link forming the cluster. The dendrogram is dominated by the large fusion height of the merge of all interneurons into cluster 103 (67 a.u.), and by the gap between the fusion heights of cluster 103 and the two contributing clusters 100 (21 a.u.) and 102 (36 a.u.) (Table 3-4). The large absolute and relative fusion heights reveals that clusters 100 and 102 are very different from each other and suggests the presence of two major clusters in the data.

Cluster 100 is very similar to contributing cluster 90, a relatively tight and homogenous cluster (7.7 a.u.) of 16 interneurons, as the other contributing cluster 96 has only 3 interneurons. On the other hand, cluster 102's contributing cluster 101 is relatively close (29 a.u.), suggesting cluster 102 contains three clusters: 93, 98, and 99, with two clusters (98 and 99) more closely related than the other.

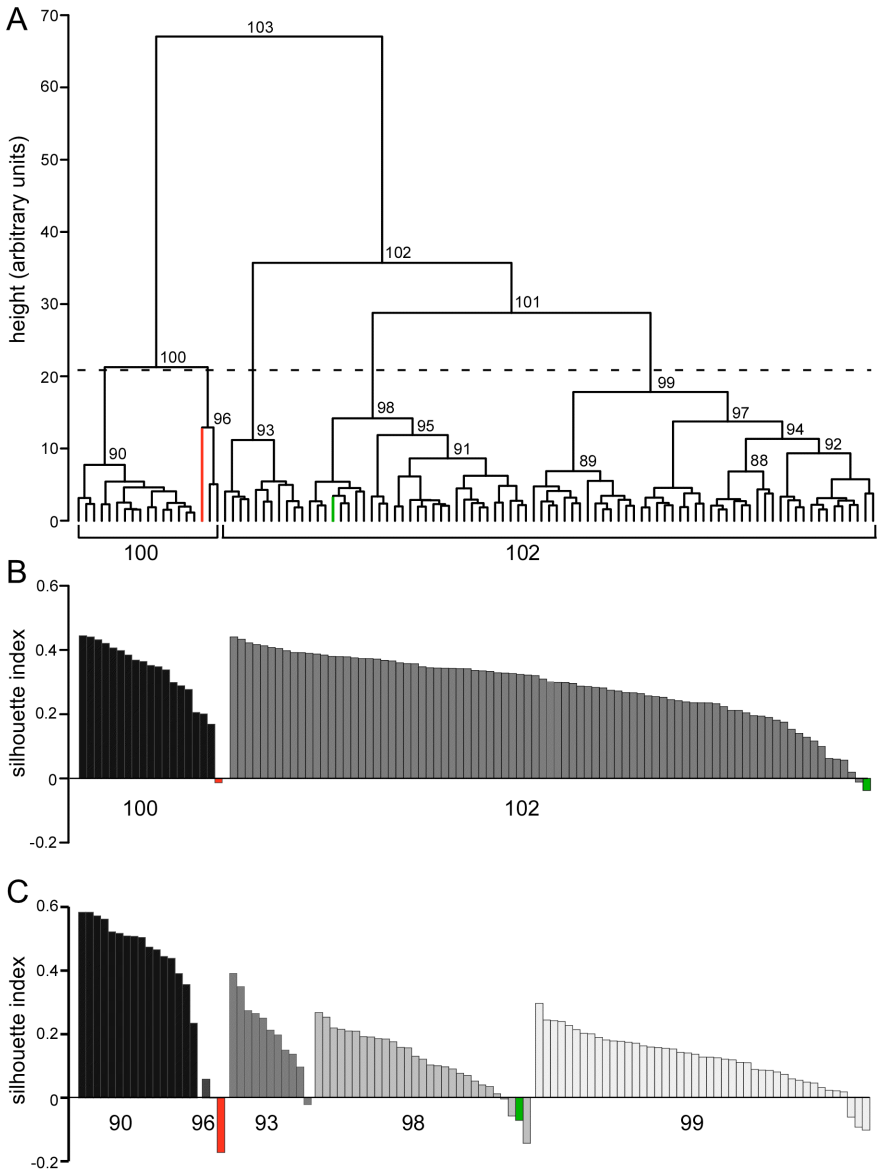

Figure 3-6. Interneurons clustered using Ward's hierarchical clustering algorithm.
Ward's hierarchical clustering was performed using 16 descriptive parameters of passive and active membrane properties (see Materials and Methods) derived from 104 interneurons.
A. Cell cluster merge heights were used to construct the dendrogram. Branch points (marking the formation of a new cluster from two smaller contributing clusters) of the 15 greatest heights are labeled with cluster identities (unique numbers assigned when each cluster is created). All clusters converge at 67 arbitrary units (a.u.). The horizontal dashed line shows the best cut height, 21 a.u. Clusters below the best cut line are 90, 93, 96, 98, and 99. Cluster 100 corresponds to the SOM group, containing 18 SOM interneurons and 1 PV interneuron (in red), while cluster 102 corresponds to the PV subgroups, containing 84 PV interneurons and 1 SOM interneuron (in green).
B. The silhouette index is shown for each interneuron in clusters formed in Ward's dendrogram following a cut above cluster 102, forming 2 clusters. Positive values indicate a good cluster assignment, whereas negative values point to an interneuron that better fits an alternate cluster.

Interneurons are shaded black (cluster 100), and gray (cluster 102). Interneurons are ordered by silhouette index within each cluster, and do not correspond to the order of interneurons displayed in the dendrogram in A. The negative index in cluster 100 (red) belongs to the single PV interneuron in that cluster, and the more negative index in cluster 102 (green) belongs to the single SOM interneuron in that cluster.
C. The silhouette index is shown for each interneuron in clusters formed in Ward's dendrogram following a cut at the best cut line, forming 5 clusters. Interneurons are shaded black (cluster 90), dark gray (cluster 96), gray (cluster 93), light gray (cluster 98) and outlined (cluster 99). Silhouette indices for the two misclassified PV and SOM interneurons are indicated in red and green respectively.

Table 3-4. Ward's hierarchical cluster analysis of membrane properties of interneurons.

cluster id	#	height	t-value	bootstrap probability	k
103	104	67.0	68.89	100	1
102	85	35.7	33.90	90	2
101	74	28.8	26.16	74	3
100	19	21.3	17.77	88	4
99	45	17.8	13.94	64	5
98	29	14.2	9.86	61	6
97	31	13.7	9.37	90	7
96	3	12.9	8.46	78	8
95	21	11.9	7.28	86	9
94	22	11.3	6.68	0	10
93	11	11.2	6.51	73	11
92	13	9.3	4.46	100	12
91	18	8.6	3.68	98	13
90	16	7.7	2.66	93	14
89	14	6.9	1.71	68	15
88	9	6.8	1.66	99	16

For each cluster id, the number of interneurons (#), height of cluster fusion (height), the t-statistic for that fusion height (t-value), and the bootstrap probability for that cluster (bootstrap probability) are shown along with the number of clusters (*k*) present in the dendrogram at that height. The upper tailed t-test reveals that clusters with t-values greater than 3.17 have heights significantly larger than the mean ($p > 0.001$).

Thus, the dendrogram suggests that one of the two major clusters can be further divided into three minor clusters, generating 4 minor clusters total.

The best cut height of 21 a.u. (dashed line, Figure 3-6) suggests a maximum of 5 clusters, or four large clusters (90, 93, 98, and 99) and one tiny heterogenous cluster (96), while the upper tailed t-test finds that clusters 91-103 are significantly larger (Table 3-4), suggesting that up to 14 clusters might be present. Note that a cut above cluster 90 would still leave the SOM cluster 90 intact. Of the largest clusters in the dendrogram, clusters 90, 100, and 102 have the highest bootstrap values (93%, 88%, and 90% respectively), while the three clusters in 102 have lower bootstrap values, between 61% and 73% (Table 3-4), suggesting the cluster identities are less certain. Silhouette plots for 2 and 5 (best cut) clusters are shown in Figure 3-6, panels B and C. The silhouette indices are positive for most interneurons in clusters 100 and 102 (Figure 3-6B), while clusters 98 and 99 each contain several interneurons with negative cluster indices (Figure 3-6C). Thus the two major clusters identified by Ward's hierarchical clustering, 90 or 100 and 102, are supported by cluster statistics.

K-means cluster analysis identifies two major clusters.

To further explore the cluster arrangements suggested by Ward's clustering, I performed k-means clustering on the same dataset. Solutions were generated for $k = 2$ through $k = 5$ (k = number of clusters) and plotted together as a heat map (Figure 3-7A) to compare cluster arrangements. The separation between the black and white clusters established at $k = 2$ is stable through $k = 5$. Even as subsequent clusters split off of the white cluster at $k = 3$ and 4 and a cluster of 2 splits off the black cluster at $k = 5$, only 3 interneurons change cluster identity between black or non-black clusters. This cluster stability suggests that the black and white clusters in $k = 2$ are the primary clusters, with the white cluster being composed of several

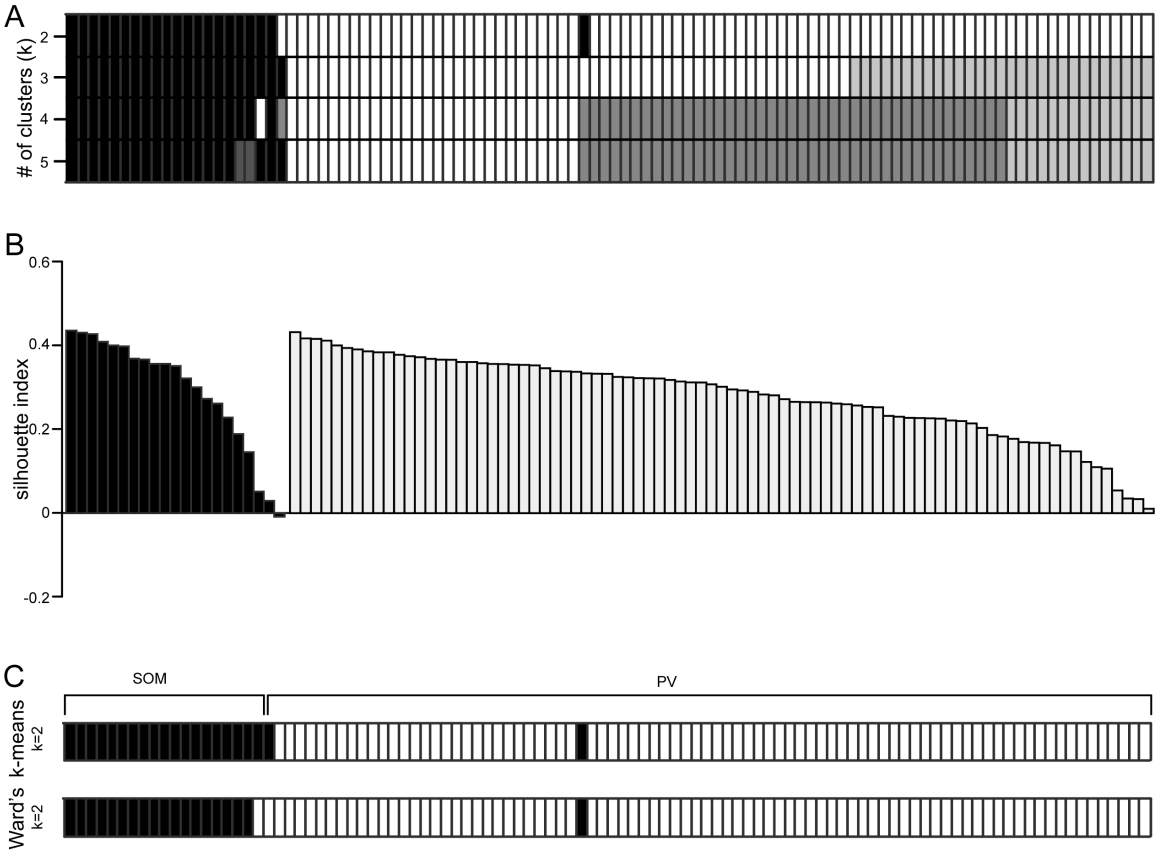

Figure 3-7. Interneurons clustered using k-means algorithm.
K-means clustering was performed using the same dataset as Ward's clustering.
A. Cluster assignments are depicted in a heat map in which each column represents one interneuron (n = 104), and each row contains the shaded k-means cluster assignment for $k = 2$ through $k = 5$.
B. The silhouette index is plotted for each interneuron in each cluster generated by k-means clustering for $k = 2$. Interneurons are shaded black and outlined, corresponding to the major clusters in A. The negative index in the black cluster belongs to the one of the two PV interneurons in that cluster. As in Figure 3-6B, interneurons are ordered by silhouette index within each cluster and do not correspond to the order of interneurons displayed in the heatmap in A.
C. The k-means cluster assignments for $k = 2$ (upper row) are depicted with the $k = 2$ cluster assignments from Ward's clustering (lower row). In brackets above the rows, the known identity of the interneurons is indicated.

smaller clusters. Silhouette analysis for the $k = 2$ clusters reveals that only one (black) interneuron has a negative silhouette index, indicating it is closer to the other (white) cluster.

Algorithm comparison

When the Ward's and k-means cluster assignments for 2 clusters are aligned for comparison (Figure 3-7C), the clusters are found to be very similar. Only 2 out of 104 interneurons are assigned differently between the two algorithms. Both algorithm cluster assignments are compared with the known PV or SOM identity of each interneuron (in brackets above Figure 3-7C), revealing that only two interneurons are incorrectly grouped by each algorithm.

In the Ward's cluster configuration (Figure 3-6), cluster 100 corresponds to the SOM group, containing 18 SOM interneurons and 1 PV interneuron (in red), while cluster 102 corresponds to the PV group, containing 84 PV interneurons and 1 SOM interneuron (in green). In the Ward's silhouette plot for two clusters (Figure 3-6B), the two misclassified interneurons have the two most negative silhouette indices of all the interneurons. Lower down the dendrogram and illustrated in the silhouette plot for the best cut of 5 clusters (Figure 3-6C), PV classified with SOM belongs to cluster 96, the tiny heterogenous cluster, indicating that it is not similar to the majority of SOM interneurons.

In the k-means cluster configuration (Figure 3-7), the black cluster corresponds to the SOM group and contains 19 SOM and 2 PV interneurons, while the white cluster corresponds to the PV group and contains 83 PV interneurons. The sole negative silhouette index in the k-means $k = 2$ silhouette plot belongs to the one of the two PV interneurons in the black (SOM) cluster.

The k-means k = 2 cluster statistics (see Materials and Methods) are very similar to the Ward's two cluster statistics. K-means clusters have a similar average silhouette width (0.28) to

Ward's (0.29) and a similar average between cluster distance, or separation between clusters (k-means 6.6 vs Ward's 6.7). The average within cluster distance (a measure of cluster tightness) for k-means is 4.72 compared to 4.75 for Ward's. Similarly, the Calinski Harabasz index of between/within cluster distance is 28.5 for k-means and 28.2 for Ward's.

Both the Ward's hierarchical clustering algorithm and k-means clustering algorithm classify PV and SOM into different clusters with a high degree of success - 98% of interneurons were correctly clustered by each algorithm. Furthermore, even when the clustering algorithms do not correctly cluster a cell, there are often statistical indicators of an ill-fitting cluster member. In particular, small heterogenous groups with relatively large merge heights for all objects and negative cluster indices are good indicators that those members are not clustered well.

The two major clusters can be visualized using PCA.

The first two principal components generated by PCA (PC1 and PC2) together account for 50% of the total variance in the dataset. To further characterize the validity of the two major clusters, I plotted PC1 against PC2 for each interneuron in a scatter plot (Figure 3-8), coded according to the k-means $k = 2$ cluster assignment. The gray cluster corresponds to the PV group and the black corresponds to the SOM group. A straight line can separate most of the interneurons in the two clusters. However, two black interneurons are close to the gray black cluster (indicated by arrows in Figure 3-8). These are the two PV positive interneurons that were clustered with SOM interneurons into the black cluster by the k-means algorithm.

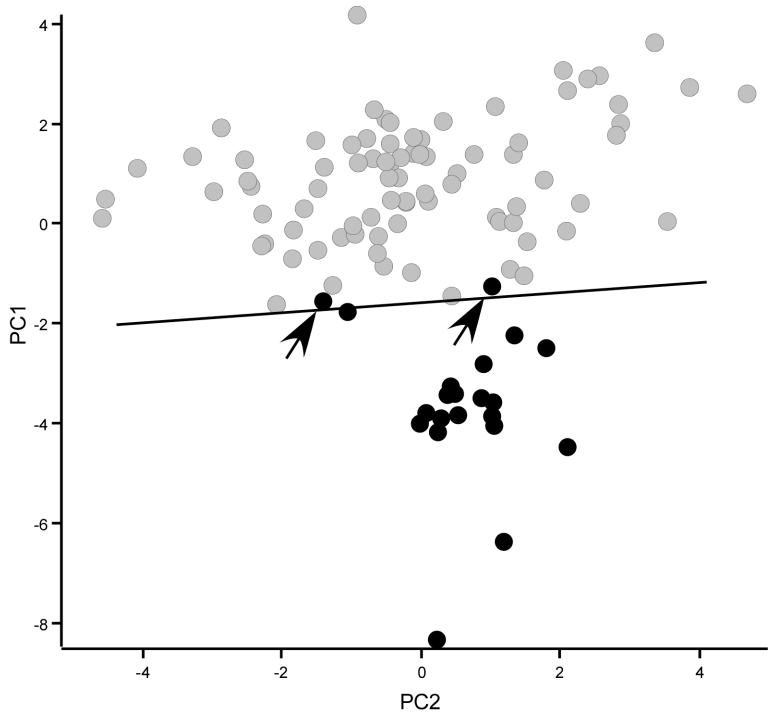

Figure 3-8. Separation of subgroups in scatter plot of first two principal components. The first (PC1) and second (PC2) principal component values derived for each interneuron are plotted against each other and shaded according to the k=2 assignment in the k-means cluster. The gray cluster corresponds to the PV expressing interneurons, and the black cluster corresponds to SOM expressing interneurons. A straight line can separate most of the interneurons in the two clusters. The interneurons indicated by arrows are the two PV positive interneurons that were clustered with SOM interneurons by the k-means algorithm.

DISCUSSION

The goal of this dissertation is to identify subgroups of PV interneurons that might play divergent roles in a cortical circuit. To do so I use cluster analysis in chapter four to look for sub-groupings of PV interneurons based on their membrane properties. In this chapter I validate the methods used to identify PV subgroups by applying them to a dataset composed of passive and active membrane properties from PV and SOM interneurons, two distinct groups of interneurons with unique membrane properties.

Both algorithms effectively separate PV and SOM interneurons into different clusters with an error rate of only 2%. This confirms that the parameters extracted from the membrane properties together describe the differences between the interneurons, and that the clustering algorithms function as intended in clustering those parameters.

The result is especially impressive considering that all 16 dimensions of parameters were used rather than principal components or a few key features known to vary between the groups such as frequency accommodation and AP peak adaptation. This was done in order to keep the conditions as similar as possible to the PV clustering methods.

Interestingly, the two statistical methods for determining the number of clusters in a Ward's dendrogram examined here (best cut and upper tailed t-test) both suggest a greater number of clusters than 2, and would break PV interneurons up into several subgroups. The lesson taken here and applied in clustering PV interneurons is to look beyond these measures to factors like the shape of the dendrogram and the similarities between the Ward's and the k-means cluster methods. Another way to find the number of clusters k is to pick the first k in which all clusters identified in k-means match a Ward's cluster (Karagiannis et al. 2009). This

method would correctly identify the k = 2 cluster arrangement as the major division in the dataset. The silhouette algorithms were also a good indicator of the better clustering arrangement.

In conclusion, the methods used effectively separate the two known groups of interneurons PV and SOM. They also suggest the existence of subgroups in the PV dataset with different membrane properties.

CHAPTER 4: SUBGROUPS OF PARVALBUMIN EXPRESSING INTERNEURONS IN LAYERS 2/3 OF THE VISUAL CORTEX

ABSTRACT

The input, processing, and output characteristics of inhibitory interneurons help shape information flow through layers 2/3 of the visual cortex. Parvalbumin (PV) positive interneurons are a major type of inhibitory interneuron that modulate and synchronize the gain and dynamic responsiveness of pyramidal neurons. To define the diversity of PV interneurons in layers 2/3 of the developing visual cortex, I characterize their passive and active membrane properties. Using Ward's and k-means multidimensional clustering, I identify four PV interneuron subgroups. The most notable difference between the subgroups is their firing patterns in response to moderate stimuli just above rheobase. Two subgroups show regular and continuous firing at all stimulus intensities above rheobase. The difference between these two continuously firing subgroups is that one fired at much higher frequencies and transitioned into this high frequency firing rate at or near rheobase. The two other subgroups show irregular, stuttering firing patterns just above rheobase. Both of these subgroups transition to regular and continuous firing at intense stimulations, but one of these subgroups, the strongly stuttering subgroup, shows irregular firing across a wider range of stimulus intensities. The four subgroups of PV interneurons identified here would presumably respond differently to inputs of varying intensity and frequency, generating diverse patterns of PV inhibition in the developing neural circuit.

INTRODUCTION

GABAergic interneurons are integral to brain function (Burkhalter 2008; Gulyas et al. 2010; Jonas et al. 2004; Mann and Paulsen 2007; Marin 2012). In the cortex, the most prevalent class of GABAergic interneurons express the Ca^{2+}-binding protein parvalbumin (PV) (Gonchar

and Burkhalter 1997; Gonchar et al. 2007; Lee et al. 2010; Miyoshi et al. 2007; Xu et al. 2010). PV interneurons have been implicated in schizophrenia (Lewis et al. 2012) and may be involved in other brain disorders including autism and epilepsy (Marin 2012). In the visual cortex, PV interneurons regulate gain control (Atallah et al. 2012) (Ma et al. 2010; Wilson et al. 2012) and feature selectivity (Lee et al. 2012) of visual processing and underlie gamma oscillatory activity (Cardin et al. 2009; Sohal et al. 2009)

Variations in intrinsic membrane properties and firing patterns underlie an interneuron's role in neural circuit activity. The majority of PV interneurons exhibit a fast-spiking firing pattern (Blatow et al. 2003; Kawaguchi and Kubota 1993; Povysheva et al. 2008; Woodruff et al. 2009). An exception is multipolar bursting cells (Blatow et al. 2003), which are located primarily at the border between layers 1 and 2, display a relatively depolarized resting membrane potential, and do not have fast-spiking firing patterns. In terms of fast-spiking PV interneurons, there are two general groups: chandelier and basket cells. Chandelier cells target the axon initial segment (Karube et al. 2004; Somogyi 1977) and can have a depolarizing effect on the postsynaptic axon (Woodruff et al. 2009). Chandelier cells can be electrophysiologically distinguished from other fast spiking PV interneurons based on their short delay to action potential onset and linear or superlinear subthreshold voltage responses to current input (Woodruff et al. 2009). Basket cells target soma and proximal dendrites (Karube et al. 2004; Kisvarday 1992; Kubota and Kawaguchi 2000; Tamas et al. 1998; Wang et al. 2002). Basket cells show heterogeneity in morphology (Wang et al. 2002), neurophysiology (Goldberg et al. 2008; Karagiannis et al. 2009), and receptive field (Runyan et al. 2010). At present, the variations in membrane and firing properties in the basket group of fast-spiking PV interneurons have not been quantified.

Here I targeted PV interneurons expressing either EGFP or tdTomato in layers 2/3 of the visual cortex focusing on fast-spiking 'basket' cells; based on membrane properties, I excluded any putative chandelier and multipolar bursting cells. My goal was to characterize variations in membrane properties (passive membrane properties, action potential shape and firing pattern) of PV interneurons to identify possible functional subgroups. To that end, I used multi-dimensional clustering, which can distinguish pyramidal neurons and major inhibitory interneuron groups from each other (Cauli et al. 2000; Dumitriu et al. 2007; Guerra et al. 2011; Karube et al. 2004; Krimer et al. 2005; Nowak et al. 2003). When applied to an already restricted group of interneurons (for example, those interneurons that express somatostatin), it can identify subgroups (Halabisky et al. 2006; Ma et al. 2006; McGarry et al. 2010). For these experiments, I used juvenile mice, focusing on the period between eye-opening (Gordon and Stryker 1996) and the onset of the critical period, the timing of which is dependent on maturation of PV basket cells (Fagiolini et al. 2004; Huang et al. 1999).

Using multi-dimensional clustering, I identified four novel PV interneuron subgroups in layers 2/3 in the visual cortex. While all subgroups developed continuous firing patterns with strong stimulation, subgroups differed in their firing patterns in response to near rheobase stimuli. The subgroups also differed in passive membrane properties, action potential shape, and excitatory inputs. These PV interneuron subgroups would participate differently to the wide range of the inputs arriving with eye-opening.

MATERIALS AND METHODS

Materials and methods were as described in Chapter 3 except as noted below.

Animals

Two transgenic mouse lines were used to identify PV interneurons in visual cortex: B13 and PV-tdTomato.

Pharmacological compounds

To record mEPSCs, action potentials were blocked using Na_v blocker tetrodotoxin (TTX) (1 μM). Inhibitory synaptic responses were blocked with $GABA_A$ competitive antagonist bicuculine (50 μM) or the non-competitive antagonist picrotoxin (50 μM). For selected recordings, AMPAR-mediated currents were blocked with 6-cyano-7-nitroquinoxaline-2,3-dione (CNQX) (10 μM) to confirm glutamatergic mEPSCs. All reagents unless otherwise noted were obtained from either Sigma Aldrich Inc. (St. Louis, MO) or Tocris Cookson Inc. (Ellisville, MO).

Acute slice preparation

Mice between postnatal day 14 (P14) and day 19 (P19) were anesthetized with isofluorane and then decapitated in accordance with the institutional animal ethics committee and in keeping with guidelines established by the National Institute of Health.

Electrophysiology

mEPSCs were sampled at 50 kHz and digitally refiltered at 2 kHz.

Experimental protocols

After recording firing patterns, the amplifier was subsequently switched to voltage clamp mode with the holding potential set to –70 mV to record sEPSCs and mEPSCs. Neurons were voltage clamped at –70 mV and recorded in 1-5 minute blocks. Spontaneous excitatory post-synaptic currents (sEPSCs) were recorded in the standard ACSF (containing Mg^{2+}) used to measure action potentials, while miniature EPSCs (mEPSCs) were recorded in the same solution

with added TTX (1 μM) and bicuculine (50 μM) or picrotoxin (50 μM). At the end of some experiments, CNQX (10 μM) was washed in to confirm that the observed synaptic events were AMPAR-mediated.

Analysis

To try to minimize the contribution of chandelier cells to the dataset, I did not include cells with both no delay (estimated delay to 1st AP of 150 ms or less) and linear or superlinear subthreshold I/V relationships (Woodruff et al. 2009). Based on these criteria, two cells were excluded as putative chandelier cells from the data set.

Parameter selection

Multi-dimensional cluster analysis was performed on passive and active membrane properties to identify possible common groupings of PV interneurons**.** For clustering, I focused on 17 parameters (Figure 4-1A) that were largely unrelated. Figure 4-1A is a cross-correlation matrix of these 17 parameters with correlation indices shade- coded with black being perfectly correlated (correlation index of 1.0) and white being perfectly uncorrelated (correlation index of 0). Most parameters are not strongly correlated (e.g. threshold & AP peak). However, some parameters were correlated (correlation coefficient > 0.6) (R_m & rheobase; AP half-width & AHP latency; AHP latency & AHP area, ISI average & minimum frequency; minimum frequency & CV frequency) but were both retained because they encompass different features of membrane properties. For example, AP half-width is correlated to AHP latency because they both encompass the rate of AP decay; however, AP half-width also encompasses AP duration whereas AHP latency describes the rate of after-hyperpolarization. Maximum instantaneous frequency and the maximum to minimum instantaneous frequency ratio (max/min ratio) were not used in clustering but are included in the results to contrast the subgroups.

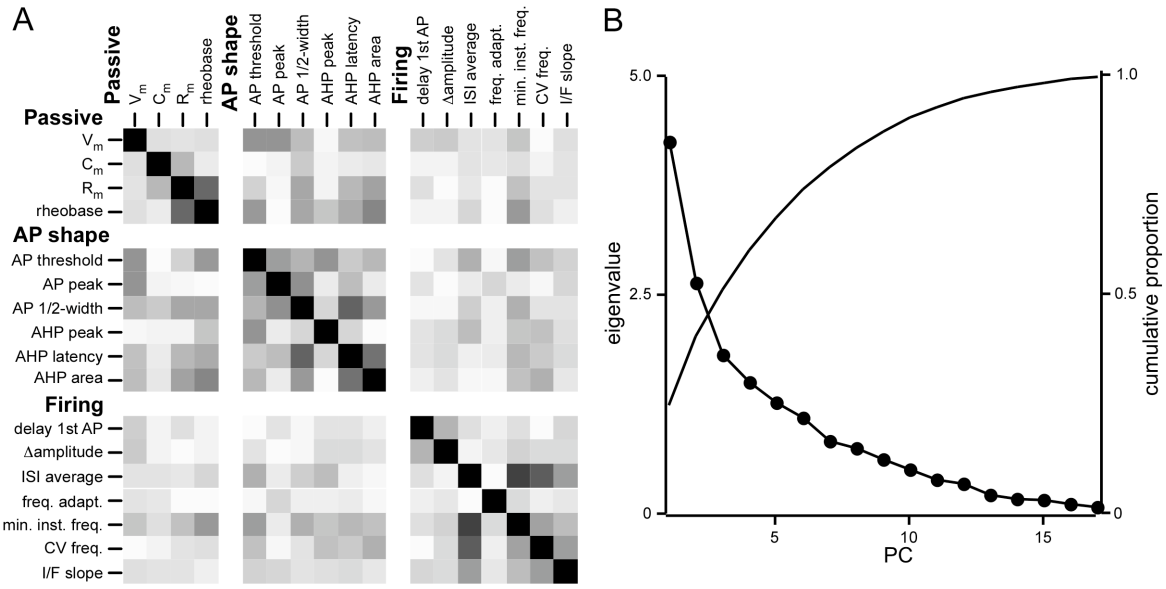

Figure 4-1. Correlation of parameters describing membrane properties of PV interneurons.
A. The 17 passive and active membrane properties used for clustering (derived from 82 interneurons) are arrayed against each other in a correlation matrix with the degree of correlation indicated by the shading, white is uncorrelated (correlation index of 0) and black is perfectly correlated (correlation index of 1, diagonal squares).
B. Principal component analysis does not greatly reduce variance. For each principal component (PC) derived from the 17 PV interneuron membrane properties in A, the variance explained by that PC (eigenvalue, solid circles), and the cumulative proportion of variance explained by all principal components up to and including that PC (cumulative proportion, line) are plotted.

I also performed PCA on the 17 parameters to reduce the dimensionality. Figure 4-1B shows the eigenvalues associated with the resulting principal components (PC) along with the proportion of the total variance accounted for by that PC. The first seven eigenvalues are greater than 1, indicating that they contribute more to the variance of the dataset than one of the original parameters, and together account for 82% of the variance in the dataset. The first 10 PCs together are required to surpass 90% of the variance. PCA is most useful when it can identify two or three PCs to describe most of the variance in a dataset. Because the first three PCs accounted for only 51% of the variance, I did not use PCs for clustering, and instead used the 17 original parameters accompanied by a unique id assigned to each cell.

mEPSP analysis

mEPSCs were analyzed using the MiniAnalysis program (Synaptosoft). Event detection parameters averaged a 2 ms baseline 4 ms prior to a suprathreshold peak. Amplitude threshold levels were set at 5 pA and recordings with baseline noise root mean squared (RMS) greater than 5 pA were discarded. The area threshold was set at 1.5 times the amplitude threshold. Five or more events separated by maximum intervals of 5 ms were labeled as bursts and removed. Segments with high levels of noise that obscured the baseline were omitted, and event detection resumed when the baseline leveled. mEPSC events from individual cells were measured for amplitude, 10-90% rise-time, half-width, area, and time to 50% decay, illustrated in Figure 4-2. mEPSC frequency was measured as the inverse of the time in seconds between $mEPSC_x$ and $mEPSC_{x+1}$ (for cumulative histograms) and as the total number of events recorded divided by the total time (average mEPSC frequency). To determine significant differences between the synaptic inputs to subgroups, I used two approaches. First, 500 mEPSCs were randomly sampled from each cell and combined for each subgroup and the Komogorov-Smirnov (KS) test

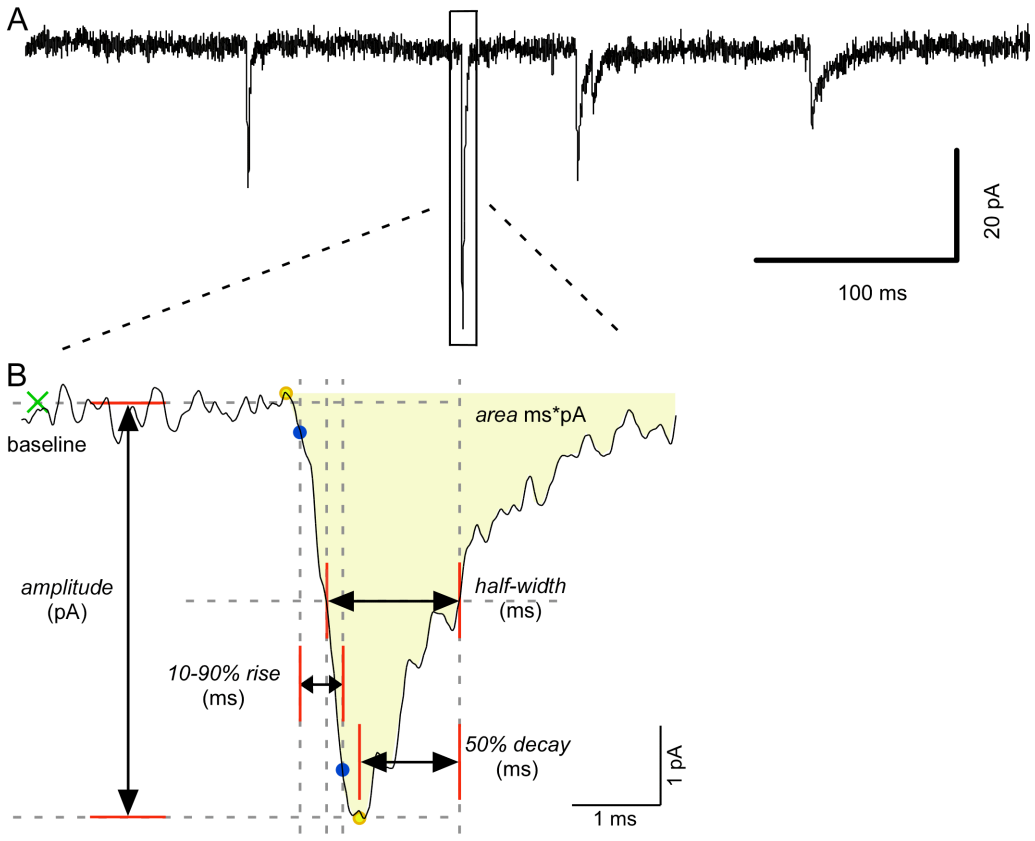

Figure 4-2. Miniature excitatory spontaneous synaptic currents recorded from PV interneurons in layers 2/3 mouse visual cortex.
A. Current trace (500 ms) recorded in the presence of TTX and picrotoxin, digitized at 50 kHz and digitally filtered at 2 kHz.
B. Expanded (7 ms) section from A illustrating how each mEPSC event parameter is calculated.

($\alpha = 0.05$) was used to test for significance between subgroup cumulative histograms. The resulting p value was adjusted for multiple pairs using the Bonferroni correction. Second, mEPSC measurements were averaged for each cell and an ANOVA followed by Tukey test was performed for each parameter. Statistical analysis was performed in IgorPro (WaveMetrics).

RESULTS

Parvalbumin positive interneurons in layers 2/3 of the visual cortex from B13 and PV-tdTomato mice

PV interneurons in layers 2/3 of the visual cortex in acute slices were identified by EGFP or tdTomato fluorescence, patched in the whole cell configuration, and stimulated to confirm fast-spiking firing patterns. I recorded passive and active membrane properties (see Materials and Methods) from 97 fast-spiking interneurons (86 from PV-tdtomato and 11 from B13 mice) ranging in age from P14 to P19. Several membrane properties including R_m, AP half-width, and firing frequency undergo significant developmental changes in layers 2/3 PV interneurons between P13 and P18 in the somatosensory cortex (Goldberg et al. 2011) and between P15 and P25 in the visual cortex (Lazarus and Huang 2011). In the data set, parameters measured between P15 and P19 were largely independent of age, including R_m (Figure 4-3A), AP half-width (Figure 4-3B), and AHP area (Figure 4-3C), The only parameter which showed age dependence between P15 and P19 was the I/F slope (Figure 4-3D), which at P15 was significantly greater than that at P17, P18, and P19. On the other hand, several parameters including AP half-width (Figure 4-3B), AHP peak (not shown), AHP latency (not shown), and I/F slope (Figure 4-3D) were significantly different between P14 and older ages. Given the age dependence of P14 features, I excluded P14 interneurons from the data set and focused only on interneurons between P15 and P19 (n = 82).

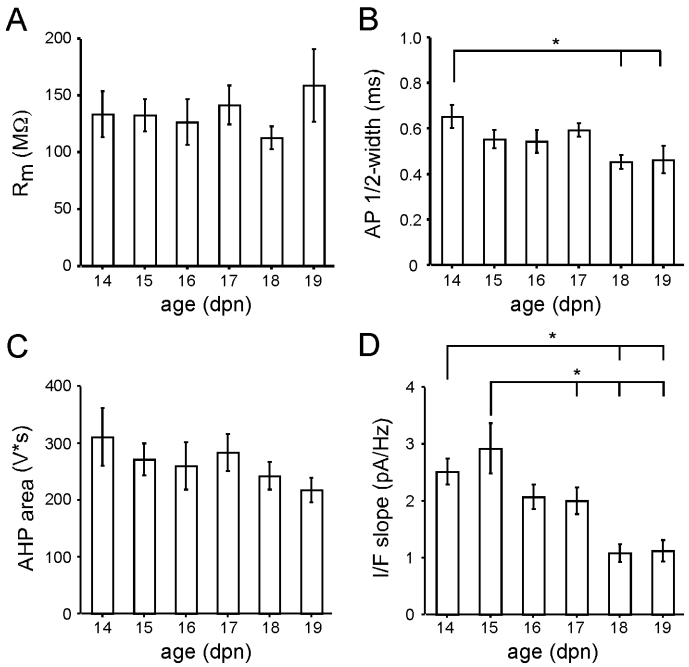

Figure 4-3. Age dependence of membrane properties in PV interneurons in layers 2/3 of the visual cortex between P15 and P19.
A, B, C and D. Bar graph of the (A) average membrane resistance (R_m), (B) action potential half-width (AP half-width), (C) AHP area and (D) I/F slope for each day of age post natal (dpn).
* Indicates significantly different values (Tukey, $p < 0.05$). Error bars are ± SEM.

Ward's hierarchical cluster analysis identifies 4 major clusters of PV interneurons

Initially, I used Ward's hierarchical clustering (see Materials and Methods) to identify subgroups of PV interneurons. Figure 4-4A illustrates a dendrogram based on Ward's clustering. Each cluster formed is given a unique id, shown above the horizontal link forming the cluster. The relationship among interneurons in a cluster is described by the absolute fusion height (the height of the horizontal link merging two contributing clusters), and by the difference between the cluster fusion heights of the formed cluster and its contributing clusters. A larger absolute fusion height means that the interneurons in that cluster are more heterogeneous. A larger difference between the fusion height of the formed cluster and its contributing clusters indicates that the contributing clusters are more distinct from each other. The height is in arbitrary units (a.u.), as it measures distance between standardized parameter measures.

The two largest clusters, 79 and 80, merge at a height of around 36 a.u. (Figure 4-4A; Table 4-1). This fusion height is well separated from contributing cluster 79, which forms around 22 a.u., but not from contributing cluster 80, which forms around 32 a.u. This means that the two contributing clusters making up cluster 80 (77 and 78), are almost as dissimilar to each other as they are to cluster 79, or that clusters 77, 78, and 79 are all comparably dissimilar. Cluster 79 is well separated from its contributing clusters 63 (6.1 a.u.) and 76 (14 a.u.) suggesting that 63 and 76 are separate clusters. Hence, based on the fusion heights, there appear to be at least three clusters.

To define the statistical significance of the clusters identified in the dendrogram, I used the best cut test, the upper tailed t test, and bootstrapping (Figure 4-4 and Table 4-1). The best cut height is 17 (dashed line), identifying 4 clusters: 63, 76, 77, and 78.

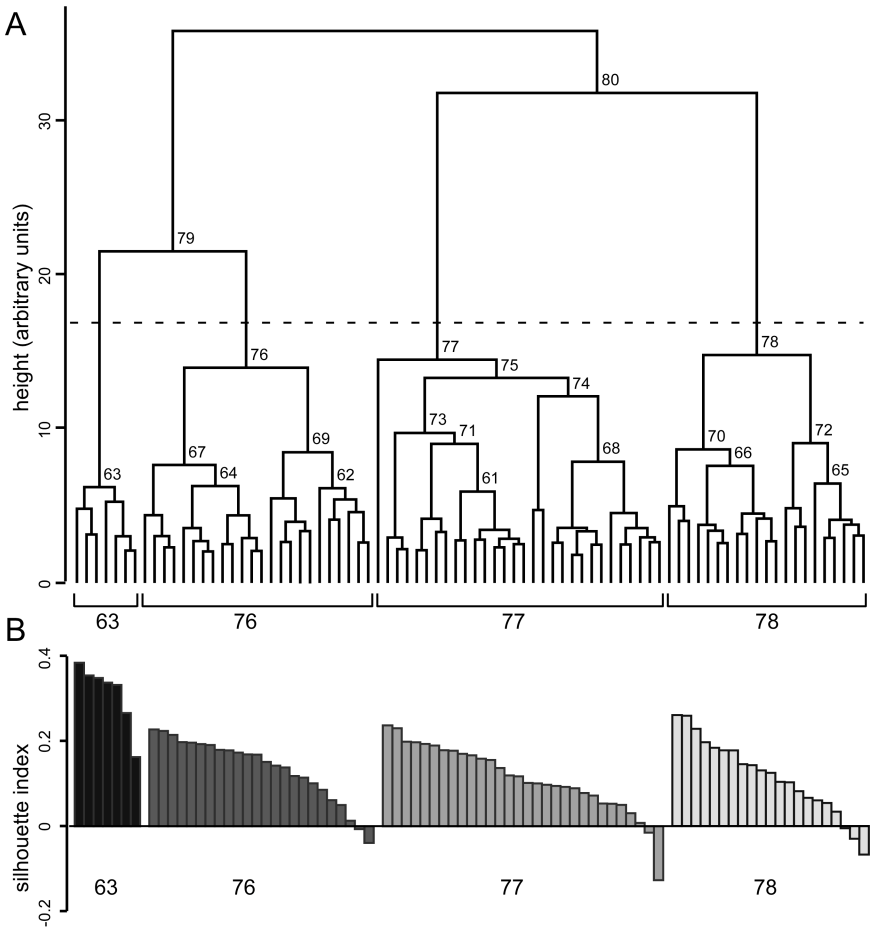

Figure 4-4. PV interneurons grouped using Ward's hierarchical clustering algorithm.
Ward's hierarchical clustering was performed using 17 descriptive parameters of passive and active membrane properties (see Materials and Methods) derived from 82 interneurons.
A. Cell cluster merge heights were used to construct the dendrogram. Branch points (marking the formation of a new cluster from two smaller contributing clusters) of heights greater than 5.5 are labeled with cluster identities (unique numbers assigned when each cluster is created). All clusters converge at 36 arbitrary units (a.u.). The horizontal dashed line shows the best cut height, 17 a.u. Clusters below the best cut line are 63, 76, 77, and 78.
B. The silhouette index is shown for each interneuron in the subgroups identified using Ward's clustering following a cut at the best cut line ($k = 4$) Positive values indicate a good cluster assignment, whereas negative values point to an interneuron that better fits an alternate cluster. Interneurons are shaded black (cluster 63), dark gray (cluster 76), gray (cluster 77) and light gray (cluster 78). Interneurons are ordered by silhouette index within each cluster, and do not correspond to the order of interneurons displayed in the dendrogram in A.

Table 4-1. Ward's hierarchical cluster analysis of membrane properties of PV interneurons.

cluster id	#	height	t-value	bootstrap probability	k
81	82	35.81	47.49		1
80	51	31.78	41.15	96	2
79	31	21.48	24.97	100	3
78	21	14.73	14.37	66	4
77	30	14.43	13.89	92	5
76	24	13.90	13.06	0	6
75	29	13.24	12.03	70	7
74	14	12.04	10.14	99	8
73	15	9.65	6.39	70	9
72	9	8.99	5.36	94	10
71	12	8.94	5.28	51	11
70	12	8.59	4.72	97	12
69	11	8.40	4.42	77	13
68	12	7.78	3.45	100	14
67	13	7.58	3.13	97	15
66	9	7.52	3.04	94	16
65	6	6.36	1.22	96	17
64	9	6.21	0.98	94	18
63	7	6.14	0.87	96	19
62	6	6.07	0.76	90	20
61	8	5.84	0.40	99	21

For each cluster id, the number of interneurons (#), height of cluster fusion (height), the t-statistic for that fusion height (t-value), and the bootstrap probability for that cluster (bootstrap probability) are shown along with the number of clusters (k) present in the dendrogram at that height. The upper tailed t-test reveals that clusters with t-values greater than 3.20 have heights significantly larger than the mean ($p > 0.001$).

Based on the upper tailed t-test, cluster ids 68 through 81, including 63, 76, 77, and 78, all have statistically significant fusion heights (Table 4-1) ($p < 0.001$). Bootstrapping finds the probability that a given cluster will contain the same pool of interneurons under various conditions, and uses this measure of resilience to assign it a confidence value, listed in Table 1 as bootstrap probability. The largest clusters with bootstrap values greater than 95% ($p > 0.05$) (Table 4-1) are 61, 63, 65, 67, 68, 70, 74, 79, 80, and 81. Cluster 76 has a bootstrap probability of 0%, while cluster 77 has a bootstrap probability of 92%. Thus, of the four largest clusters (63, 76, 77, 78), two (63 and 78) are validated in three separate tests and two (76 and 77) are validated in two of the three tests.

Silhouette analysis was used to examine the quality of interneuron assignments in the four major clusters (63, 76, 77, 78) from the Ward's clustering dendrogram. The silhouette index for each interneuron is grouped in descending order by cluster (Figure 4-4B). All interneurons in cluster 63 (average silhouette index of 0.31) have a positive silhouette index indicating an optimal cluster placement. For cluster 76 (average silhouette index 0.14), 22 out of 24 interneurons are positive, for cluster 77 (average silhouette index 0.11), 28 out of 30 are positive, and for cluster 78 (average silhouette index of 0.12), 18 out of 21 are positive. In total, 75 out of 82 interneurons have a positive silhouette index with an overall silhouette index of 0.14 ± 0.01 (mean ± SEM). The silhouette results confirm that there is a natural clustering to the data; cluster 63 is the most tightly clustered, while clusters 76, 77, and 78 are more loosely clustered.

In summary, Ward's hierarchical clustering identifies four clusters: clusters 63 (7 interneurons), 76 (24 interneurons), 77 (30 interneurons), and 78 (21 interneurons).

K-means cluster analysis identifies the same general clustering arrangement.

To further examine the PV interneurons subgroups, I performed k-means clustering on the same dataset as the Ward's clustering described above. Solutions were generated for $k = 2$ through $k = 8$ (k = number of clusters). Solutions $k = 2$ through $k = 6$ were plotted together as a heat map (Figure 4-5A) to facilitate comparisons between clusters. A number of interneurons from both the black and gray clusters at $k = 2$ are moved into the new clusters appearing at $k = 3$ and $k = 4$. Importantly, at $k = 4$ cluster assignments stabilize and show remarkable consistency even with larger k. The cluster shaded black contains the same 11 interneurons from $k = 4$ through $k = 6$. The dark, medium, and light gray clusters are identical between $k = 4$ and $k = 5$ (a single interneuron splits off from the medium gray cluster at $k = 5$). At $k = 6$, when 10 interneurons split off from the light gray to form the white cluster, two additional interneurons shift clusters - one interneuron moves from light to medium gray, and another interneuron moves from dark to light gray. With additional clusters ($k = 7$ and $k = 8$, not shown), new clusters continue to be split off from the existing clusters and only one interneuron changes clusters. In summary, the cluster configuration appearing at $k = 4$ is retained at $k = 5$ through 8, with the clusters being split but not exchanging members – only three interneurons change cluster membership.

Examining the k-means results for an overarching pattern, PV interneurons can be clustered into one consistent (black) cluster PV1a, and three largely consistent clusters PV1b (dark gray), PV2 (medium gray) and PV3 (light gray). PV1a and PV1b are so named because in both Ward's and k-means clustering (see below) these clusters appear to be more closely associated with each other than PV2 or PV3.

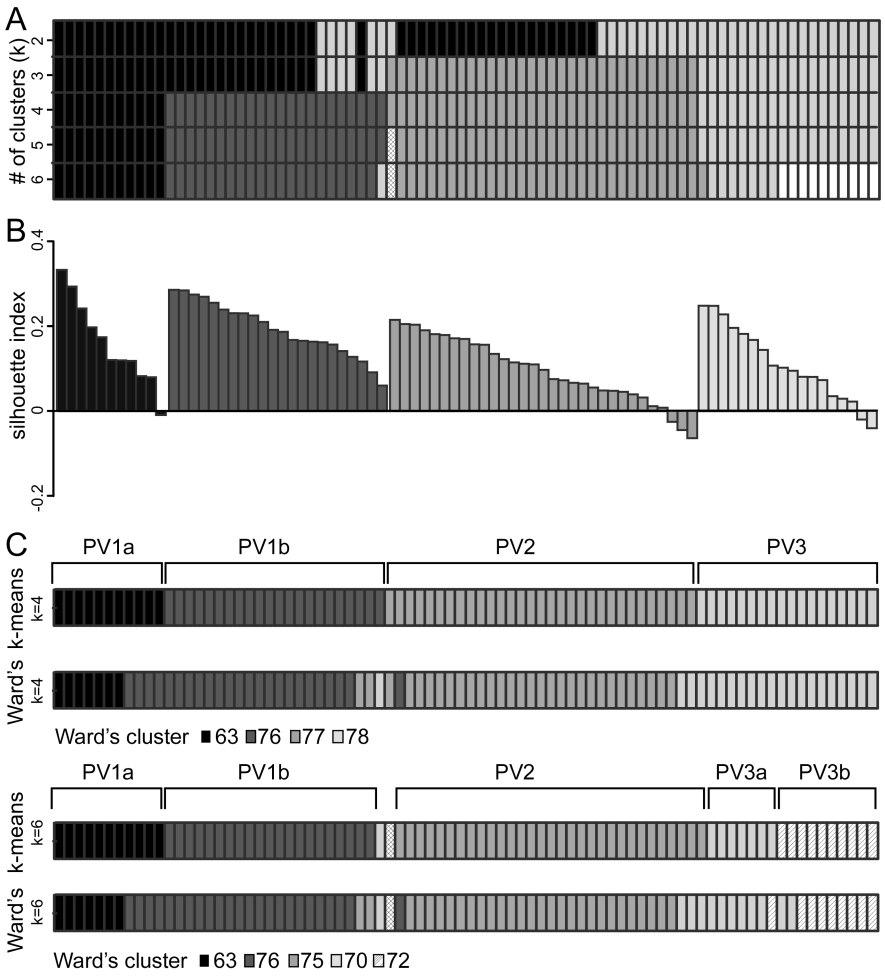

Figure 4-5. Subgroup assignment of PV interneurons with k-means clustering.
K-means clustering was performed using the same dataset as Ward's clustering.
A. Cluster assignments are depicted in a heat map in which each column represents one interneuron (n = 82), and each row contains the shaded k-means cluster assignment for $k = 2$ through $k = 6$.
B. The silhouette index is plotted for each interneuron in each cluster generated by k-means clustering for $k = 4$. Interneurons are shaded black, dark gray, gray, and light gray, corresponding to the major clusters in A. As in Figure 3B, interneurons are ordered by silhouette index within each cluster and do not correspond to the order of interneurons displayed in the heatmap in A.
C. The k-means cluster assignments for $k = 4$ (upper panel, upper row) are depicted with the best cut cluster assignments from Ward's clustering (upper panel, lower row). Cells clustered differently between the two methods are labeled. The four major k-means clusters are labeled with the corresponding subgroup identity; PV1a, PV1b, PV2, and PV3. In the lower panel, the k-means cluster for $k = 5$ is depicted alongside the cluster assignments from Ward's dendrogram cut at $k = 5$, illustrating the further subdivision of PV3 into two subgroups.

Silhouette analysis was used to evaluate the k-means cluster results for $k = 4$ (Figure 4-5B). For PV1a (average silhouette index 0.16), 10 of 11 interneurons have a positive silhouette index. All interneurons in PV1b (0.19) are positive. For PV2 (0.09), 28 of 31 and for PV3 (0.11), 16 of 18 interneurons are positive. In total, 76 out of 82 interneurons have a positive silhouette index with an average silhouette index of 0.13 ± 0.01. All interneurons with a negative silhouette index have cluster PV1b as a nearest neighbor.

The k-means cluster solution for $k = 4$ corresponds well to the 4 clusters identified using Ward's dendrogram (Figure 4-5C): PV1a overlaps extensively with Ward's cluster 63, PV1b with cluster 76, PV2 with cluster 77, and PV3 with cluster 78. For $k = 4$, 72 out of 82 or 88% of interneurons are assigned to the same clusters between the two methods. For seven of the interneurons that are differently assigned, the silhouette value in the Ward's clustering is negative and the nearest neighbor cluster is comparable to the cluster where k-means assigns it. Four of the ten interneurons that are differently assigned move between PV1a and PV1b, which are more closely related according to the Ward's dendrogram.

Based on the average cluster separation statistics (see Materials and Methods), k-means clusters the data comparably to or slightly better than Ward's. K-means clusters have a similar average silhouette width (0.13) to Ward's (0.14) and a similar average between cluster distance, or separation between clusters (k-means 5.95 vs Ward's 5.94). However, k-means clusters outperform Ward's on other measures. For example, the average within cluster distance (a measure of cluster tightness) for k-means is 4.61 compared to 4.68 for Ward's. Similarly, the Calinski Harabasz index of between/within cluster distance is 13.44 for k-means and 12.60 for Ward's (a larger number indicates better clustering).

Based on these indices and close examination of the 10 interneurons differing between the Ward's and k-means cluster assignments, I chose to use the k-means cluster assignments as the better clustering arrangement. Nevertheless, there is strong overall agreement between the Ward's and k-means cluster arrangement. In addition, the conclusions were comparable even if the Ward's cluster arrangement was used (data not shown).

The four distinct clusters can be visualized using PCA.

The first two principal components generated by PCA (PC1 and PC2) together account for 41% of the total variance in the dataset. To further characterize the validity of the four clusters, I plotted PC1 against PC2 for each interneuron in a scatter plot (Figure 4-6), coded according to the k-means cluster assignment. Three of the major subgroups (PV1b, dark gray; PV2, gray; and PV3, outlined light gray) are clearly distinguishable from each other, and can be completely separated by two straight lines drawn at cross angles to each other. PV2 is the best-separated cluster. PV3 and PV1b interneurons are also fairly well separated, with only one PV3 interneuron in close proximity to PV1b interneurons. No straight line can perfectly separate PV1a (black) from PV1b in these dimensions; at least one PV1b is located far into the PV1a area, and PV1a is diffusely distributed with no discernable core cluster. None of the interneurons in the boundary between PV1a and PV1b switch cluster identity with different *k* in k-means clustering or between Ward's clustering and k-means clustering, and none has negative silhouette values. It is likely that additional separation between the two subgroups arises in the remaining variance (59%) not described by the first two PCs. Despite the limitations of using PCA to represent the dataset, these results support the subgroups identified through k-means clustering.

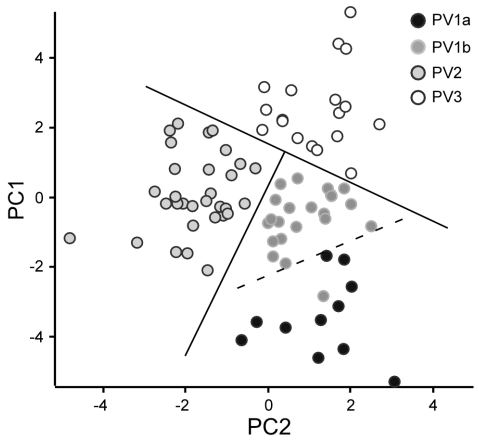

Figure 4-6. Separation of subgroups in scatter plot of first two principal components. The first (PC1) and second (PC2) principal component values derived for each interneuron are plotted against each other and shaded by the k-means cluster (PV1a, PV1b, PV2, and PV3). Subgroups of interneurons are shaded black (PV1a), dark gray (PV1b), gray (PV2), and outlined light gray (PV3).

Membrane properties of the PV interneuron subgroups in layers 2/3 of the visual cortex

Based on k-means cluster analysis, I identify four major subgroups of PV interneurons in layers 2/3 of the visual cortex that I call PV1a, PV1b, PV2, and PV3. PV1a and PV1b are more closely related to each other than to PV2 and PV3. The passive membrane properties, AP shape, and firing patterns of the different subgroups are illustrated in Figure 4-7 and Figure 4-8 and summarized in Table 4-2.

Firing properties.

The most distinctive differences between the subgroups are firing patterns. In general, interneurons in the PV1 subgroups fire regularly and continuously at all current injections above rheobase (Figures 4-7A & 4-7B, left columns) with PV1a interneurons firing at a higher frequency than PV1b. Both PV2 and PV3 interneurons fire with an irregular stuttering pattern near rheobase (Figure 4-7A, right columns). At a higher stimulus evoking firing in the 30 Hz range, PV2 firing remains irregular (Figure 4-7B, middle right) while PV3 firing becomes regular (Figure 4-7B, right). With stronger stimuli and higher frequency firing, the majority of PV2 interneurons (19/31) ultimately reach a regular continuous firing pattern (data not shown). Thus, PV2 interneurons show irregular firing over a significantly wider range of stimuli and frequencies than PV3 interneurons. In general, PV1a and PV1b interneurons can be classified as 'continuous firing', PV2 as 'strongly stuttering', and PV3 as 'weakly stuttering' interneurons.

Quantitatively, the difference in firing patterns is most discernable in the maximum to minimum instantaneous frequency ratio (max/min Ratio) and the coefficient of variation of firing frequency (CV frequency)(Table 4-2). The max/min ratio for continuous firing PV1a (1.8 ± 0.3, mean ± SEM) and PV1b (2.0 ± 0.05) is significantly less than strongly stuttering PV2 (8.6 ± 1.1).

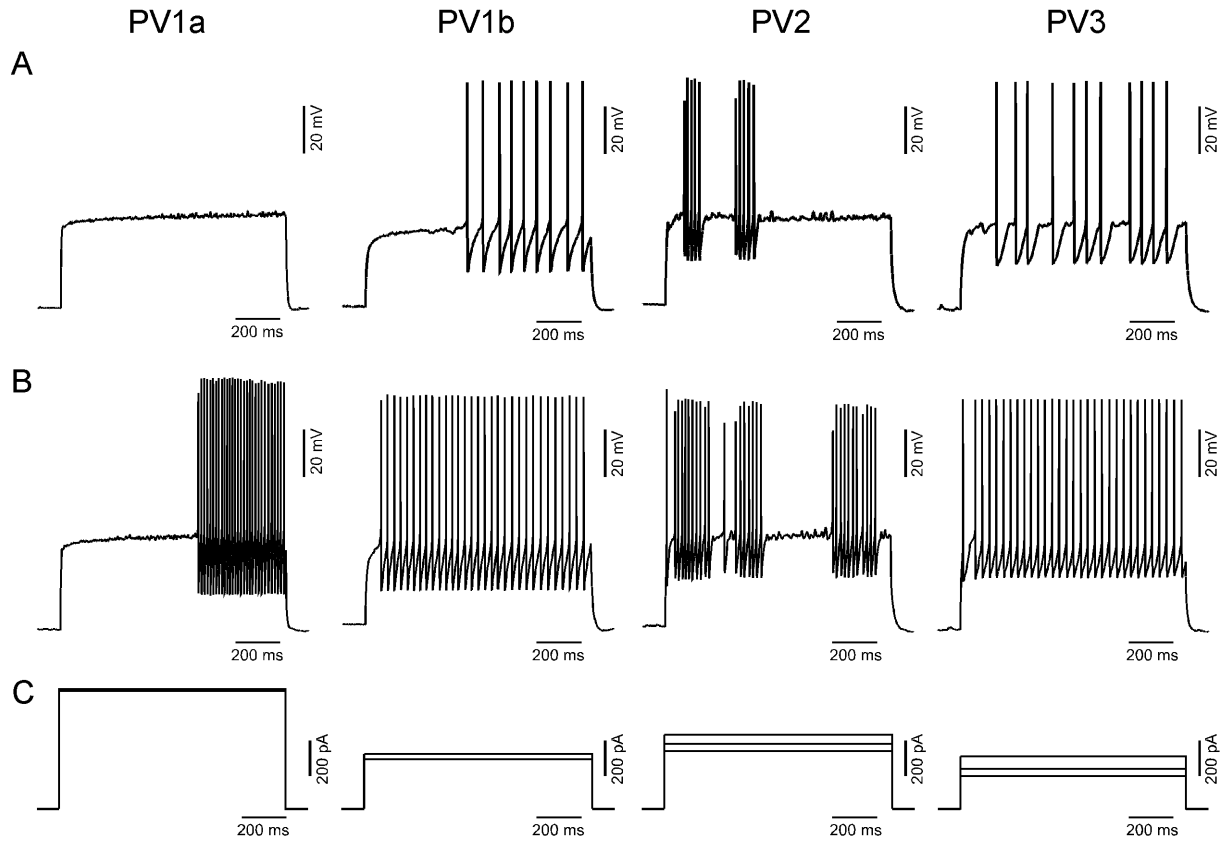

Figure 4-7. Membrane properties of PV interneuron subgroups in layers 2/3 of the visual cortex.

Action potential firing patterns from representative interneurons from PV1a (*left*), PV1b (*middle left*), PV2 (*middle right*), or PV3 (*right*) subgroups.

A. Near rheobase voltage traces contain approximately 10 action potentials. PV1a interneurons typically jumped from no or a few APs to much higher frequencies (>25 Hz). The representative PV1a cell jumps from no to 30 APs, so the trace immediately before the 30 AP trace is shown.

B. Voltage traces (from the same cell shown in A and B) containing approximately 30 action potentials.

C. 1 second depolarizing currents injected into current clamped PV interneurons generating the traces shown in A and B. The rheobase current is also shown for comparison, if different from the stimulus trace for A, B.

Table 4-2. Passive and active membrane properties of PV interneuron subgroups.

	PV1a	PV1b	PV2	PV3	Tukey Test
Passive					
V_m (mV)	-72 ± 2	-77 ± 1	-77 ± 2	-83 ± 1	1a,3 2,3
C_m (pF)	20.4 ± 1.2	20.4 ± 1.1	19.4 ± 0.6	18.4 ± 0.8	N.D.
R_m (MΩ)	84 ± 8	129 ± 13	104 ± 5	213 ± 20	1a,3 1b,3 2,3
rheobase (pA)	570 ± 60	320 ± 30	400 ± 20	200 ± 20	1a,1b 1a,2 1a,3 1b,3 2,3
AP shape					
AP threshold (mV)	-25.8 ± 2.4	-30.4 ± 1.9	-39.5 ± 1.3	-42.3 ± 1.4	1a,2 1a,3 1b,2 1b,3
AP peak (mV)	21.1 ± 2.8	23.2 ± 2.1	16.0 ± 2.0	12.2 ± 2.8	1b,3
AP 1/2-width (ms)	0.40 ± 0.03	0.48 ± 0.03	0.48 ± 0.02	0.73 ± 0.03	1a,3 1b,3 2,3
AHP peak (mV)	-26.9 ± 1.2	-27.0 ± 0.6	-23.4 ± 0.5	-23.9 ± 0.7	1a,2 1b,2 1b,3
AHP latency (ms)	1.4 ± 0.1	2.1 ± 0.2	1.7 ± 0.1	3.7 ± 0.4	1a,3 1b,3 2,3
AHP area (V*s)	170 ± 20	270 ± 10	180 ± 10	390 ± 40	1a,1b 1a,3 1b,2 1b,3 2,3
Firing pattern					
delay 1st AP (ms)	360 ± 130	590 ± 60	490 ± 60	460 ± 60	N.D.
Δ amplitude (mV)	5.3 ± 1.7	-2.2 ± 0.8	2.2 ± 0.8	0.7 ± 0.8	1a,1b 1a,3 1b,2
ISI average (ms)	12.9 ± 1.0	26.8 ± 0.8	29.5 ± 0.7	30.5 ± 0.9	1a,1b 1a,2 1a,3 1b,3
frequency adapt.	0.98 ± 0.12	0.96 ± 0.06	1.22 ± 0.38	0.89 ± 0.11	N.D.
max. inst. freq. (Hz)	95.9 ± 6.0	45.6 ± 1.6	66.7 ± 4.4	43.2 ± 2.0	1a,1b 1a,2 1a,3 1b,2 2,3
min. inst. freq. (Hz)	59.5 ± 7.1	29.0 ± 1.9	8.6 ± 1.1	20.4 ± 2.6	1a,1b 1a,2 1a,3 1b,2 2,3
max/min inst.	1.8 ± 0.3	2.0 ± 0.5	13.8 ± 2.6	4.5 ± 1.5	1a,2 1b,2 2,3
CV frequency	0.08 ± 0.01	0.09 ± 0.01	0.27 ± 0.01	0.13 ± 0.01	1a,2 1b,2 2,3
I/F slope	0.6 ± 0.2	1.5 ± 0.2	2.4 ± 0.3	2.1 ± 0.2	1a,2 1a,3 1b,2
age (dpn)	18.1 ± 0.2	17.3 ± 0.3	16.2 ± 0.2	16.4 ± 0.3	1a,2 1a,3 1b,2
# of interneurons	11	22	31	18	
B13	0	3	5	1	
PV-tdTomato	11	19	26	17	

PV subgroups identified by k-means cluster analysis ($k = 4$) are characterized by passive membrane properties, action potential shape, and firing pattern (see Materials and Methods). Listed are the 17 properties used for clustering plus two additional parameters: maximum instantaneous frequency, and the maximum to minimum instantaneous frequency ratio (max/min inst. ratio). Values shown as mean ± SEM. ANOVA followed by Tukey test ($p < 0.05$) was used to identify significant differences between subgroup parameters. N.D., none of the subgroups were significantly different.

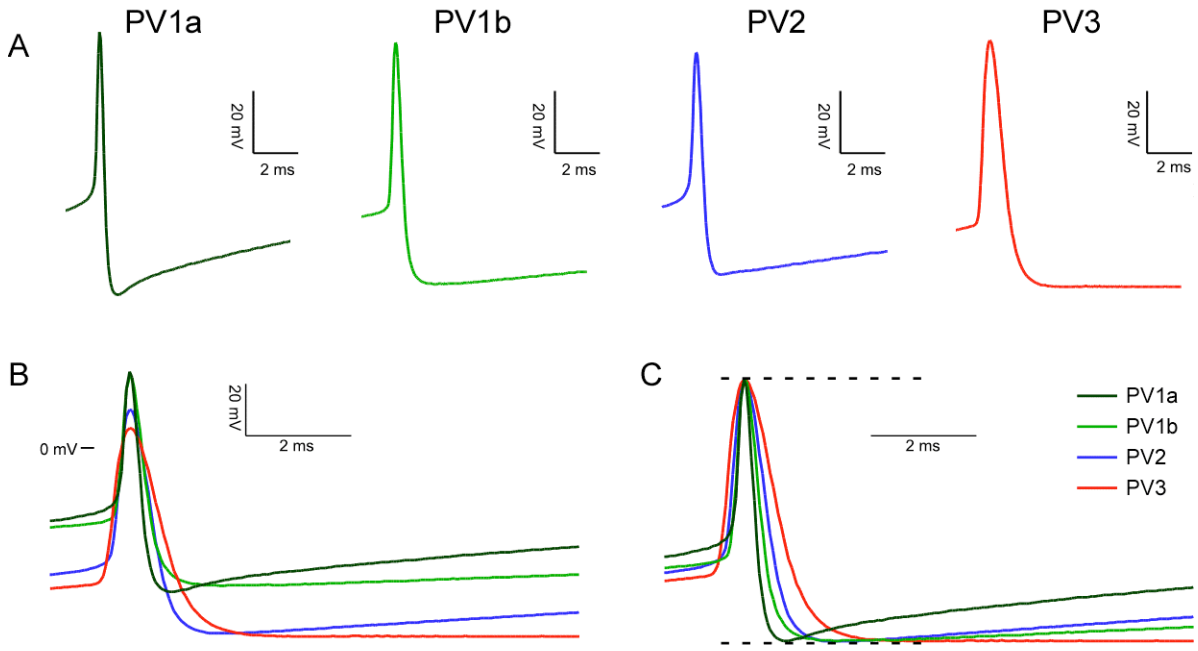

Figure 4-8. First action potential evoked at rheobase in each PV subgroup.
A. The first action potential firing in response to rheobase current is shown magnified to 10 ms. Shading and line thickness is coded by subgroup, for use in interpreting B and C below. Rheobase stimulus for the records shown is 677 (PV1a), 280 (PV1b), 330 (PV2), and 190 (PV3) pA.
B. The same traces shown in A are overlayed using 0 mV to align them vertically.
C. The same traces shown in A and B are scaled to the same max and min, then overlayed.

Similarly, the CV frequency is less variable in PV1a (0.08 ± 0.01) and PV1b (0.09 ± 0.01) than in PV2 (0.27 ± 0.01). The weakly stuttering PV3 displays intermediate values of max/min ratio (4.5 ± 1.5) and CV frequency (0.13 ± 0.01), which are still significantly lower than PV2.

The major difference between PV1a and PV1b is that PV1a interneurons fire at a higher frequency, so the PV1a interneurons have a statistically lower ISI average (12.9 ± 1.0 ms) than PV1b (26.8 ± 0.08 ms), and higher maximum (95.9 ± 6.0 Hz) and minimum instantaneous firing frequency (59.5 ± 7.1 Hz) than PV1b (45.6 ± 1.6 Hz, 29.0 ± 1.9 Hz). PV1a interneurons show a significant decrease in peak AP amplitude (positive Δamplitude) with repeated firing (5.3 ± 1.7 mV), while PV1b interneurons show a slight increase (-2.2 ± 0.8 mV).

Passive membrane properties.

PV3 is significantly different from all other subgroups in passive membrane properties related to membrane resistance (R_m and rheobase). PV3 interneurons have higher input resistance (213 ± 20 MΩ) compared to PV1a (84 ± 8 MΩ), PV1b (129 ± 13 MΩ), and PV2 (104 ± 5 MΩ) (Table 4-2). PV3 interneurons also require less current to depolarize to threshold (rheobase) (200 ± 20 pA) compared to PV1a (570 ± 60 pA), PV1b (320 ± 30 pA), or PV2 (400 ± 20 pA) (Table 4-2, Figure 4-7C). PV1a has a significantly higher rheobase than PV1b.

Action potential shape.

PV3 also differs from all other subgroups in features of AP shape dependent on the membrane time constant (AP half-width, AHP latency, and AHP area) (Figure 4-8). The AP threshold of both PV1a (–25.8 ± 2.4 mV) and PV1b (–30.4 ± 01.9 mV) is significantly more depolarized than either PV2 (-39.5 ± 1.3 mV) or PV3 (-42.3 ± 1.4 mV) (Figure 4-8B). The AP half-width of PV3 interneurons is wider (0.73 ± 0.03 ms) than that of PV1a (0.40 ± 0.03 ms),

PV1b (0.48 ± 0.03 ms), or PV2 (0.40 ± 0.02 ms) (Figure 7C). PV3 also has slower, larger AHPs - PV3 AHP latency (3.7 ± 0.4 ms), and area (390 ± 40 V*s) are significantly greater than PV1a (1.4 ± 0.1 ms, 170 ± 20 V*s), PV1b (2.1 ± 0.2 ms, 270 ± 10 V*s), and PV2 (1.7 ± 0.1 ms, 180 ± 10 ms). PV1a has a significantly smaller AHP area than PV1b.

Excitatory synaptic inputs differ between some PV interneuron subgroups

To find out if the identified subgroups also differed in excitatory inputs, I recorded AMPAR-mediated miniature excitatory postsynaptic currents (mEPSCs) in PV interneurons with stable, low noise resting membrane currents (52 of the 82 interneurons were recorded: PV1a, 7; PV1b, 15; PV2, 18; PV3, 12). Figure 4-9 illustrates 10 second and 100 ms current traces from representative interneurons in each subgroup (Figure 4-9A), and cumulative histograms (upper panels) and ANOVA of means (lower panels) for mEPSC amplitude (Figure 4-9B), 10-90% rise (Figure 4-9C), half-width (Figure 4-9D) and frequency (Figure 4-9E).

The Komogorov-Smirnov (KS) test finds significant differences between each of the subgroups in amplitude, 10-90% rise, half-width, and frequency as well as area (data not shown) ($p < 0.05$). A comparison of mean values, using ANOVA (see Materials & Methods), highlights the largest differences visible in the cumulative histograms. PV1a has the smallest mEPSC amplitudes, (16.5 ± 1.1 pA) significantly smaller than PV2 (23.8 ± 0.9 pA) (Figure 4-9B), and the smallest mEPSC area (19.6 ± 1.4 pA*ms), significantly smaller than PV2 (27.9 ± 1.0 pA*ms) and PV3 (29.3 ± 1.6 pA*ms) (data not shown). PV2 has the fastest 10-90% rise times (0.59 ± 0.04 ms), significantly faster than PV1a and PV1b (PV1a 0.89 ± 0.06; PV1b 0.79 ± 0.05) (Figure 4-9C). PV3 half-widths (1.64 ± 0.10 ms) are significantly wider than those of PV1a (1.23 ± 0.06 ms), PV1b (1.34 ± 0.06 ms), and PV2 (1.34 ± 0.04 ms) (Figure 4-9C).

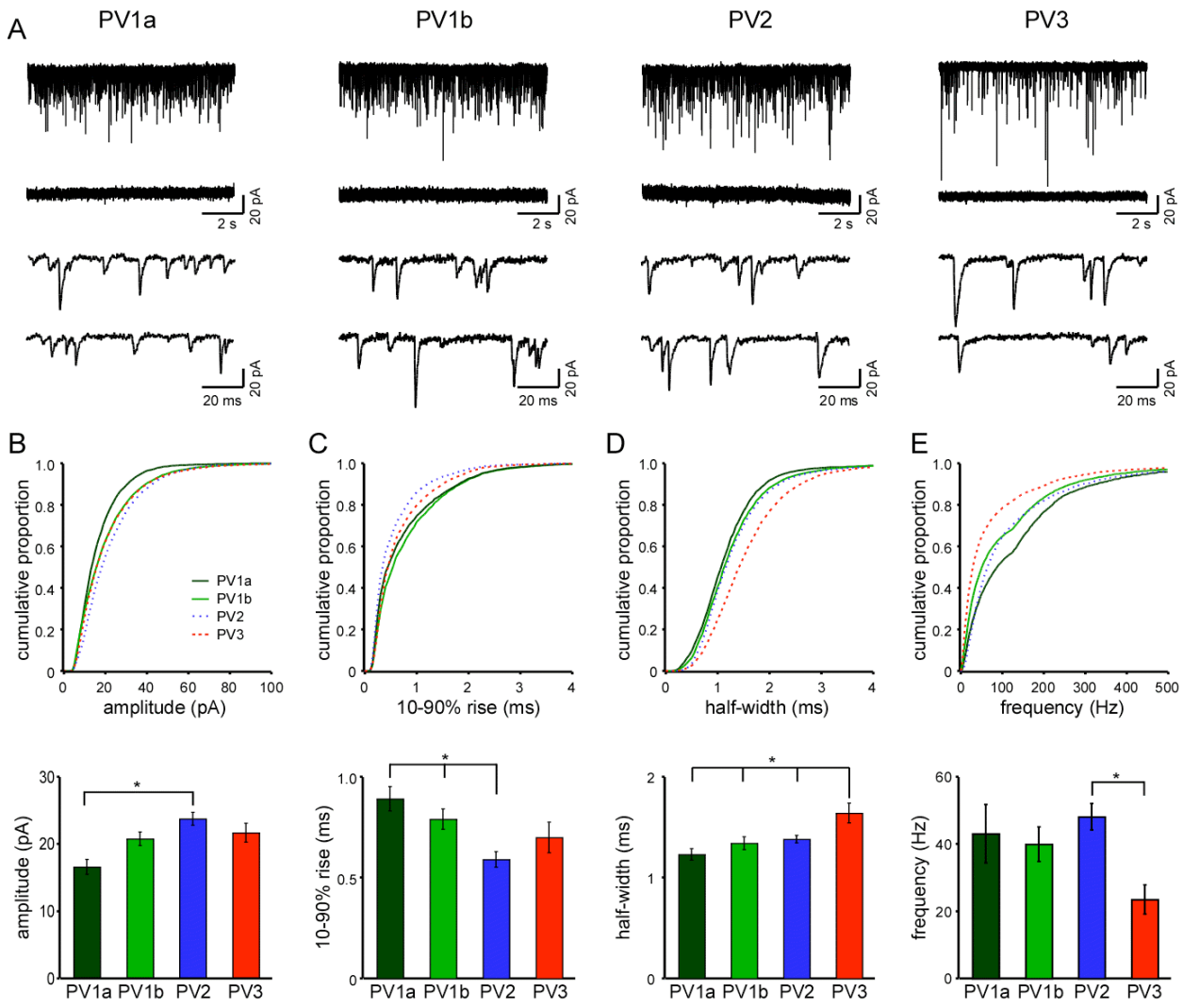

Figure 4-9. mEPSC characteristics of PV interneuron subgroups.
A. Representative current traces from each subgroup (10 s total time shown), in whole cell voltage clamp (V_h –70 mV) in the presence of Mg^{2+}, TTX, and bicuculine (upper traces) or in the same solution but with added CNQX (center traces). The lower two traces (100 ms each) are expanded from the upper trace to show details.
B-E. Cumulative histograms (upper panels) and bar graphs of mean values (lower panels) of mEPSC amplitudes (B), 10-90 % rise time (C), half-width (D) and frequency (E) for each subgroup. See Materials and Methods for details. For cumulative histograms, the KS test finds significant differences between subgroups for each parameter ($p < 0.05$). For bar graphs, * indicates significantly different values (Tukey, $p < 0.05$). Error bars in bar graphs are ± SEM.

PV3 interneurons also show less frequent mEPSCs (23.5 ± 4.3 Hz) than PV2 (48.1 ± 4.0 Hz), but not less than PV1a or PV1b (Figure 4-9E).

DISCUSSION

To identify subgroups of fast-spiking PV interneurons in layers 2/3 of the visual cortex, I used two different clustering algorithms: Ward's and k-means. I initially used the Ward's dendrogram to visualize the relationships between clusters of interneurons and used this information to aide in interpreting k-means clustering (which requires a defined number of clusters). The two clustering algorithms largely converged on the same four subgroups of PV interneurons (Figures 4-4 & 4-5), supporting that the results yielded good cluster assignments.

Using multidimensional cluster analysis of passive membrane properties, AP shape, and firing patterns, I identified four major subgroups of PV interneurons in layers 2/3 of the juvenile mouse visual cortex. Most interneurons in all four subgroups, if injected with high levels of current, fired APs in a regular, continuous fashion. However, at stimulations closer to rheobase, the four subgroups showed notable differences (Table 4-2): PV1a and PV1b fired regularly and continuously at all current injections with PV1a firing at higher rates (Figures 4-7A & 4-7B). In contrast, PV2 exhibited stuttering firing patterns over a wide range of current injections above rheobase (Figure 4-7B). PV3 was somewhat more complex but typically showed stuttering firing patterns at stimulations just above rheobase then transitioned to continuous firing upon slightly higher stimulation levels (Figure 4-7C). PV3 was also notable for its slow passive membrane properties and broad AP shape (Figure 4-8).

Comparison to previously published results

Continuous and stuttering firing patterns have previously been observed in PV interneurons (Goldberg et al. 2008; Miyoshi et al. 2007; Povysheva et al. 2008) and as shown

here, stuttering converted to continuous firing with strong stimulus (Povysheva et al. 2008). Earlier papers have not specifically explored variations in PV basket cell stuttering patterns, and the variation in transition from stuttering to continuous firing.

A delay from depolarization to the appearance of the first AP is common in PV interneurons, particularly in layer 2 (Goldberg et al. 2008; Miyoshi et al. 2007). The delay is correlated with a more depolarized threshold mediated by Kv1.1, and stronger depolarizing stimuli convert the firing to the continuous fast-spiking. All subtypes described here contain a majority of interneurons with delayed firing, and in all subgroups stronger depolarizing stimuli reduces the delay, suggesting that this feature does not contribute to the subgroups identified here.

Another commonly noted feature of PV interneurons is an abrupt onset of firing, in which the rheobase response fires multiple spikes (averaging 16 Hz) (Goldberg et al. 2008; Kawaguchi 1995). In the dataset, the majority of interneurons in all groups fired fewer than ten spikes (10 Hz) in response to rheobase stimulus. PV1b interneurons had the largest number (6 of 22) interneurons that did show an abrupt onset (10 or more Hz) while PV2 had the least (1 of 31 fired at 10 Hz). PV1a interneurons jumped abruptly from firing none or a few APs to frequencies over 30 Hz, while the other subgroups saw a more gradual response. Thus, the classical abrupt onset is not present as described in most PV interneurons, and is absent in the strongly stuttering (PV2) subgroup.

Many fast spiking interneurons show a slight spike frequency adaptation in the first few action potentials (Cauli et al. 1997). PV2, the largest subgroup, is the only subgroup with a frequency adaptation ratio over 1 (Table 4-2), and the degree of adaptation (1.22) appears similar to the degree of adaptation identified previously.

Sub-threshold membrane oscillations have been observed in fast spiking interneurons, possibly mediated by TASK K2P channels (Goldberg et al. 2011). A qualitative comparison of membrane voltage traces between subgroups suggests that PV2 may have more oscillations than other subgroups (see PV2 trace, Figure 4-7A). This is consistent with the lower R_m in this subgroup, also associated with TASK channels. Nevertheless, future experiments will be required to define the role of TASK channels and sub-threshold oscillations in the stuttering firing patterns seen in PV2 interneurons.

Most immunochemicals expressed in other inhibitory interneurons are absent in PV interneurons (Gonchar et al. 2007). However, the mRNA of neuropeptide Y (NPY) and calbindin (CB) have been detected (Cauli et al. 1997; Karagiannis et al. 2009), raising the possibility of immunochemistry-based PV subgroups. NPY mRNA expression is correlated with a delay to AP onset (Karagiannis et al. 2009). However, as noted earlier, there is no significant difference in delay between subgroups, so subgroups described here likely do not align with the NPY expression. CB mRNA is present in a significant percentage (44%) of PV cells (Cauli 1997), but the electrophysiological features of CB expressing PV interneurons have not been characterized.

PV is found in large basket cells (LBCs), nest basket cells (NBCs), small basket cells (SBCs) (Wang et al. 2002), chandelier (Kawaguchi and Kubota 1998), wide arbor (Kawaguchi and Kondo 2002), and local arbor cells (Miyoshi et al. 2007), as well as multipolar bursting cells (Blatow et al. 2003). However, these morphologies are not unique to PV expression; other molecular markers including somatostatin and vasoactive intestinal peptide are expressed in interneurons with the same morphologies (Kawaguchi and Kondo 2002; Wang et al. 2002). The literature on firing patterns associated with different PV morphologies is incomplete and contradictory. One report suggests the delay to onset is restricted to fast spiking interneurons

with a local arbor (Miyoshi et al. 2007), while another reports finding delays to onset in all basket cell morphological subtypes (Gupta et al. 2000). Interestingly, stuttering may be one of several electrophysiological profiles expressed by NBCs (Gupta et al. 2000), but it is unknown how this relates to the subset of PV expressing NBCs.

Chandelier cells are the most extensively characterized as a distinct morphological subtype, and display significantly different subthreshold properties from basket cells (Woodruff et al. 2009). I took advantage of these properties to try to minimize the contribution of chandelier cells to the dataset. Still, the PV3 subgroup does share some features with the chandelier cells (higher membrane resistance, lower rheobase). However, chandelier cells appear to be concentrated at the border of layer 1 and layers 2/3 (Kawaguchi 1995; Woodruff et al. 2009), while the recordings ranged over the whole of layers 2/3. In addition, only two PV3 interneurons showed a delay to AP less than 100 ms, while all chandelier cells have an onset less than 100 ms (Woodruff et al. 2009). These factors argue against chandelier cells contributing in a major way to the PV3 subgroup. Similarly, multipolar bursting cells (Blatow et al. 2003) were minimized based on membrane properties and anatomical location (see Materials and Methods). However, future experiments will be needed to define whether any of the subgroups described here align strongly with a particular morphology.

Developmental changes in membrane properties and relevance to subgroups

The precise window of developmental changes depends on cortical area. In layers 2/3 of barrel cortex some of these developmental changes occur between P14 and P18 (Goldberg et al. 2011), while in layers 2/3 of visual cortex changes may not be fully underway before P22 (Desai et al. 2002; Goldberg et al. 2011; Lazarus and Huang 2011; Okaty et al. 2009). When quantified as a group, only the I/F slope varied from P15 to P19 (Fig. 4-3). However, some of the

differences observed between subgroups could be due to developmental changes in PV interneuron properties. Specifically, PV1a differs from other groups in having a more mature profile in a number of developmental characteristics (R_m, rheobase, half-width, AHP latency, AHP peak, and firing frequency (Goldberg et al. 2011; Lazarus and Huang 2011; Okaty et al. 2009). On the other hand, the slower passive and active membrane properties seen in PV3 are associated with the developmentally immature PV interneuron.

Basis for differences in firing patterns.

These experiments do not directly address the molecular mechanisms underlying the different firing patterns. Nevertheless, previous experiments have identified some key factors contributing to differences in membrane properties, AP shape, and firing patterns.

K_v3 type ion channels are necessary and sufficient for fast-spiking behavior in PV interneurons (Erisir et al. 1999), and expression density is correlated with firing frequency (Gu et al. 2011; Toledo-Rodriguez et al. 2004). The $K_v3.1b$ splice variant enables neurons to fire at a higher rate, similar to firing observed in PV1a (Gu et al. 2011). The other subgroups presumably have a lower expression of this channel.

Kv1 is a slowly inactivating channel that is responsible for both the delay to firing observed around threshold (Goldberg et al. 2008) and for the stuttering quality of near threshold firing patterns (Povysheva et al. 2008; Toledo-Rodriguez et al. 2004) like those observed in PV2 and PV3. However, since PV1b showed significant delay but little to no stuttering, there may be variations in channel subunit composition that differentiate expression of the delay and stuttering features. Furthermore, Kv1 subunits associate with beta subunits (Rhodes et al. 1997) which are modulated by second messengers (Pan et al. 2011) and can form hetero-multimers with other K

channel subtypes, any of which could interact with Kv1 to generate the stuttering behavior in PV2 and 3 but not PV1b.

Blocking HCN channels also creates an interrupted firing pattern (Toledo-Rodriguez et al. 2004), providing another possible factor underlying stuttering.

The slower passive membrane properties and AP shape described in PV3 are seen with a stronger potassium leak current from Kir2.2, Kir2.3, K2p1.1, and K2p9.1 (Goldberg et al. 2011; Okaty et al. 2009). These same features are associated with a lower Kv3 expression, along with a lower overall firing frequency. These slower features may enable this subgroup to convert to continuous firing at a lower firing frequency (for example by altering recovery from inactivation).

Further experiments are needed to define how specific K as well as Na channels combine to generate the diverse PV fast-spiking firing patterns described here.

Differences in excitatory input to PV interneuron subgroup

The different subgroups showed differences in excitatory input as assayed by AMPAR-mediated mEPSCs (Figure 4-8), which provides an independent verification of the subgroups. The larger PV3 mEPSC half-width could in theory be due to mEPSC amplitude, distance from soma, glutamate receptor subtype, or membrane resistance. However, the average mEPSC amplitude and area are not significantly larger in PV3 interneurons. If slow membrane kinetics or filtering with distance caused the slow half-width, the 10-90% rise time would be slower in parallel with half width. The mEPSC 10-90% rise is not significantly larger in PV3 interneurons (not shown), suggesting the difference in half-width is not due to distance from soma or membrane resistance.

This suggests that there is a real difference in the quality of excitatory input onto PV3 interneurons, possibly mediated by different glutamate receptors. GluA1, GluA2, and GluA4 subunits can be expressed in PV interneurons (Chang et al. 2010; Geiger et al. 1995), though GluA2 may be absent in a majority of PV interneurons (Kondo et al. 1997). The slower kinetics of PV3 mEPSCs could be explained by a higher ratio of GluA1 to GluA4 containing synapses. Alternatively, the kinetics could be slower due to a preponderance of flip splice variants in the AMPA receptors (Lambolez et al. 1996), or the presence of TARPs (Milstein and Nicoll 2008). Additional experiments will be required to discover the unique combination of AMPAR subunits contributing to the difference in excitatory input between subgroups.

The slightly lower mEPSC frequency seen in PV3 interneurons could be due to fewer synapses contacting PV3 dendrites, to a lower probability of release at some or all of the synapses, or to some combination of the above. If there are indeed fewer synapses overall, this could be due either to a smaller dendritic tree or lower synaptic density on some or all dendrites. Future work might confirm or eliminate some of these possibilities. Finally, the higher membrane resistance observed in the PV3 subgroup could be a result of the relatively lower numbers of synaptic events (Pare et al. 1998).

Since the role of a neuron in a circuit is dependent on its passive and active membrane properties, the different PV subgroups described here would behave differently in the context of a cortical circuit. For example, PV1a interneurons would not participate in the circuit in response to a weak stimulus, but in response to a sufficiently strong stimulus would inhibit its postsynaptic targets and with other PV1a interneurons would impose a rhythmic oscillation in the gamma range that scales up with stimulus intensity. In contrast, PV3 interneurons would participate in feed forward and feed back inhibition in response to weak inhibition. In groups, their irregular

firing at low frequencies would inhibit synchronized firing in the sub-gamma range. PV2 interneurons would exert a similar suppressive effect on synchronization over a wider range of circuit activation and firing frequencies.

CHAPTER 5: CONCLUSION

Parvalbumin expressing interneurons are a major group of inhibitory interneuron with distinct morphological and physiological characteristics that permit them a unique role in the neural circuit. Variations within PV interneuron input response and pattern output could further specify that role. To look for subgroups of PV interneurons that consistently vary together across multiple features, I used multivariable cluster analysis. Specifically, I clustered variables derived from passive, active, and firing pattern parameters using two different clustering algorithms: Ward's and k-means. The Ward's dendrogram provides a structure in which to visualize the relationships between clusters of interneurons and these relationships are used to suggest some possible numbers of clusters k. I then performed k-means clustering for a range of k and compared the resulting clusters to those identified by Ward's to find cluster arrangements in common. Bootstrapping, silhouettes, and clustering statistics were used to describe the significance of the resulting clusters.

RESULTS SUMMARY

Multiple subgroups of parvalbumin expressing interneurons are identified in layers 2/3 of the juvenile mouse visual cortex. The four major subgroups of PV interneurons differ primarily in their response to stimuli above rheobase. Near rheobase, the subgroups I call PV1a and PV1b fire regularly and continuously while PV2 and PV3 fire with irregular or stuttering firing patterns. With additional stimulus strength PV1a fires at high frequencies and PV3 adopts a continuous firing pattern, while PV2 continues its irregular firing. In addition to a transition from stuttering to regular continuous firing patterns, PV3 is distinguished by slow passive membrane properties and broad AP shape.

I validated the efficacy of this clustering procedure by using it to look for clusters in a pool composed of two major groups of inhibitory interneurons, PV and SOM. Both algorithms correctly clustered the interneurons into two separate groups with little error. The cluster solutions found by the two clustering algorithms are very similar to each other. In contrast, there is a higher percentage of disagreement between Wards and k-means clustering of PV subgroups, and the silhouette statistics indicate that the clusters are not as well separated as PV and SOM. Thus, PV subgroups do not appear to be as distinct from each other as PV interneurons are from SOM. Despite this, the two clustering algorithms do converge on the same four subgroups of PV interneurons, supporting that the clustering is identifying a real underlying pattern in PV behavior.

Miniature excitatory synaptic inputs (mEPSCs) were also recorded in a subset of PV interneurons and summarized for each PV subgroup. In particular PV1a has smaller mEPSCs than PV2 and PV3, while PV3 interneurons have significantly longer mEPSC half-widths and lower frequency mEPSCs than the other subgroups. The differences in excitatory inputs further validate the subgroups identified and contribute to understanding of the connectivity and context of the subgroups in the local circuit.

DISCUSSION OF RESULTS

Beyond the minor differences between the membrane properties of chandelier and basket cells, previous researchers have not qualitatively identified any major subgroups of PV interneurons which differ in membrane properties. It is likely that several factors contribute to these subgroups not having previously been identified. One, while PV expression has long been identified with the fast spiking interneuron, its only in the last several years that advances in mouse genetics research have resulted in commonly available strains that enable PV positive

interneurons to be specifically targeted for sampling, rather than using the multipolar shape or fast spiking phenotype as the first indicator. Thanks to the fluorescent labeling of PV expressing interneurons, there may be a more complete selection of PV interneuron types represented here. Two, multidimensional cluster analysis is increasingly being used in this field to identify subgroups, but has not been previously applied to PV subgroups. Finally, while these PV subgroups have not been characterized as subgroups before, the overall differences in passive membrane properties, AP shape, and firing patterns have each been previously described, suggesting that these findings are not anomalous.

Given equivalent input, these PV subgroups would be predicted to respond differently based on the differences in their passive and active membrane properties. However, evidence presented from synaptic recordings reveal that all subgroups do not receive equivalent input. For example, PV1a appears to receive smaller synaptic inputs and has a high rheobase, so these interneurons likely respond only to strong, synchronized activation from multiple presynaptic partners and provide regular, sustained, high frequency inhibition, contributing to further synchronization in the circuit. In contrast, PV3 receives longer lasting but infrequent inputs and has a lower rheobase. PV3 interneurons would therefore respond more readily to moderate less coincident circuit activation with irregular firing that would inhibit synchronization. With further activation its firing pattern would become regular and support the emergence of oscillations in the lower range of the gamma frequency. PV2 interneurons have a higher frequency of inputs but require more activation to fire than PV3 interneurons. These interneurons would likely respond to circuit activation with irregular firing and suppress oscillations like PV3 interneurons, but would continue to resist synchronization at higher levels of circuit activation than PV3, inhibiting higher gamma frequency oscillations. PV1 interneurons fire regularly and

continuously so once activated would contribute to synchronization and oscillations over a wide range of frequencies. Thus, I provide multiple lines of evidence that PV subgroups are capable of playing different roles in the context of a cortical circuit.

RECOMMENDATIONS FOR FUTURE RESEARCH

There are several directions for future research. One direction is to clarify the molecular mechanisms generating the different membrane properties seen in the PV subtypes. A second direction is to look beyond membrane properties and excitatory synaptic inputs to see if the subgroups differ in their axonal morphology. Finally, the role of these subgroups in the cortical network should be explored further.

There are some obvious candidates in the search for molecular mechanisms underlying the differences in membrane properties, AP shape, and firing patterns described here. Kv1 is involved in the stuttering in near threshold firing patterns (Povysheva et al. 2008), but is also implicated in the delay to firing (Goldberg et al. 2008). Therefore, the search should focus on variations in Kv1 channel subunits or Kv1 associated accessory proteins. The $K_v3.1b$ splice variant may underlie the higher firing rate observed in PV1a (Gu et al. 2011), while variation in Kv3 or potassium leak currents could generate the passive and active features seen in PV3. Beyond protein expression, the sub-cellular distribution of these channels could also generate differences in membrane properties.

PV interneurons exist in several axonal morphologies and have been classified as large basket, small basket, and chandelier cells. The axonal morphologies of the different PV subgroups should be characterized to see if the subgroups correlate with one or more of these or any other axonal morphology. The PV dataset used in this dissertation did specifically exclude candidate chandelier cells based on membrane properties, however it is still possible that

additional chandelier cells were present. Axonal morphology is most interesting as it relates to postsynaptic connectivity. The number and laminar location of axonal arborization suggests the degree and type of contribution to the cortical circuit, so any difference in axonal morphology would in turn inform about the role of the subgroup in cortical function.

The role of these subgroups in the cortex depends upon several factors – input connectivity, response to input, and output connectivity. This dissertation has addressed only the response to input and a small fraction of the question of input connectivity. Spontaneous miniature excitatory synaptic inputs did vary between subgroups, and additional differences might exist. The source (laminar, cortical, or subcortical) and number of excitatory inputs, the probability of release and short-term synaptic plasticity, and the exact location on the interneuron where the input is delivered all might differ between subgroups. The degree, location, and source of inhibitory inputs also remain unexplored. The subgroups could differentially contact postsynaptic targets based on the strength or short term synaptic plasticity of the signal, and/or cell type, laminar location, or cellular region.

The differences in membrane properties between subgroups provide a signature of subgroup membership that can be used experimentally to identify interneurons for subsequent investigations. Questions of synaptic physiology can be addressed using paired recordings or other means of presynaptic excitation such as photostimulation of caged glutamate or cells expressing channel rhodopsin, while other morphological questions require more detailed anatomical studies.

Finally, this work is performed in juvenile mouse, and based on what is already known about the timing of inhibitory interneuron maturation and the electrophysiological profile of inhibitory interneurons in adult mouse, these findings and their implications for circuit function

must be restricted to the juvenile cortex. In the future, the same methods can and should be applied to inhibitory interneuron data in adult mouse to discover whether similar patterns of differences exist in mature inhibitory interneurons, or whether the differences between subgroups observed here are restricted to juvenile mouse. Because visual development and visual cortical function are interconnected, future experiments will be needed to discover whether the interneurons are pursuing a developmental program independent of input, or whether the subgroups observed here occur in response to the onset of visual input.

REFERENCES

Akgul G, and Wollmuth LP. Expression pattern of membrane-associated guanylate kinases in interneurons of the visual cortex. *J Comp Neurol* 518: 4842-4854, 2010.

Ascoli GA, Alonso-Nanclares L, Anderson SA, Barrionuevo G, Benavides-Piccione R, Burkhalter A, Buzsaki G, Cauli B, Defelipe J, Fairen A, Feldmeyer D, Fishell G, Fregnac Y, Freund TF, Gardner D, Gardner EP, Goldberg JH, Helmstaedter M, Hestrin S, Karube F, Kisvarday ZF, Lambolez B, Lewis DA, Marin O, Markram H, Munoz A, Packer A, Petersen CC, Rockland KS, Rossier J, Rudy B, Somogyi P, Staiger JF, Tamas G, Thomson AM, Toledo-Rodriguez M, Wang Y, West DC, and Yuste R. Petilla terminology: nomenclature of features of GABAergic interneurons of the cerebral cortex. *Nat Rev Neurosci* 9: 557-568, 2008.

Atallah BV, Bruns W, Carandini M, and Scanziani M. Parvalbumin-expressing interneurons linearly transform cortical responses to visual stimuli. *Neuron* 73: 159-170, 2012.

Azouz R, and Gray CM. Dynamic spike threshold reveals a mechanism for synaptic coincidence detection in cortical neurons in vivo. *Proc Natl Acad Sci U S A* 97: 8110-8115, 2000.

Bear MF. Mechanism for a sliding synaptic modification threshold. *Neuron* 15: 1-4, 1995.
Behrends JC, and ten Bruggencate G. Changes in quantal size distributions upon experimental variations in the probability of release at striatal inhibitory synapses. *Journal of Neurophysiology* 79: 2999-3011, 1998.

Blatow M, Rozov A, Katona I, Hormuzdi SG, Meyer AH, Whittington MA, Caputi A, and Monyer H. A novel network of multipolar bursting interneurons generates theta frequency oscillations in neocortex. *Neuron* 38: 805-817, 2003.

Buhl EH, Tamas G, Szilagyi T, Stricker C, Paulsen O, and Somogyi P. Effect, number and location of synapses made by single pyramidal cells onto aspiny interneurones of cat visual cortex. *J Physiol* 500: 689-713, 1997.

Burkhalter A. Many specialists for suppressing cortical excitation. *Front Neurosci* 2: 155-167, 2008.

Calinski T, and Harabasz J. A dendrite method for cluster analysis. *Communications in Statistics* 3: 1-27, 1974.

Cardin JA, Carlen M, Meletis K, Knoblich U, Zhang F, Deisseroth K, Tsai LH, and Moore CI. Driving fast-spiking cells induces gamma rhythm and controls sensory responses. *Nature* 459: 663-667, 2009.

Cauli B, Audinat E, Lambolez B, Angulo MC, Ropert N, Tsuzuki K, Hestrin S, and Rossier J. Molecular and physiological diversity of cortical nonpyramidal cells. *J Neurosci* 17: 3894-3906, 1997.

Cauli B, Porter JT, Tsuzuki K, Lambolez B, Rossier J, Quenet B, and Audinat E. Classification of fusiform neocortical interneurons based on unsupervised clustering. *Proc Natl Acad Sci U S A* 97: 6144-6149, 2000.

Chang MC, Park JM, Pelkey KA, Grabenstatter HL, Xu D, Linden DJ, Sutula TP, McBain CJ, and Worley PF. Narp regulates homeostatic scaling of excitatory synapses on parvalbumin-expressing interneurons. *Nat Neurosci* 13: 1090-1097, 2010.

Chen X, de Haas S, de Kam M, and van Gerven J. An Overview of the CNS-Pharmacodynamic Profiles of Nonselective and Selective GABA Agonists. *Adv Pharmacol Sci* 2012: 134523, 2012.

Christie JM, and Jahr CE. Multivesicular Release at Schaffer Collateral-CA1 Hippocampal Synapses. *J Neurosci* 26: 210-216, 2006.

Coogan TA, and Burkhalter A. Hierarchical organization of areas in rat visual cortex. *J Neurosci* 13: 3749-3772, 1993.

Dantzker JL, and Callaway EM. Laminar sources of synaptic input to cortical inhibitory interneurons and pyramidal neurons. *Nat Neurosci* 3: 701-707, 2000.

DeFelipe J. Chandelier cells and epilepsy. *Brain* 122 (Pt 10): 1807-1822, 1999.

DeFelipe J, Hendry SH, and Jones EG. Visualization of chandelier cell axons by parvalbumin immunoreactivity in monkey cerebral cortex. *Proc Natl Acad Sci U S A* 86: 2093-2097, 1989.

Desai NS, Cudmore RH, Nelson SB, and Turrigiano GG. Critical periods for experience-dependent synaptic scaling in visual cortex. *Nat Neurosci* 5: 783-789, 2002.

Dobrunz LE, and Stevens CF. Heterogeneity of Release Probability, Facilitation, and Depletion at Central Synapses. *Neuron* 18: 995-1008, 1997.

Dodge FA, Jr., and Rahamimoff R. Co-operative action of calcium ions in transmitter release at the neuromuscular junction. *J Physiol* 193: 419-432, 1967.

Douglas R, Martin, K. Neuronal ciruits of the neocortex. *Annu Rev Neurosci* 27: 419-451, 2004.

Dumitriu D, Cossart R, Huang J, and Yuste R. Correlation between axonal morphologies and synaptic input kinetics of interneurons from mouse visual cortex. *Cereb Cortex* 17: 81-91, 2007.

Erisir A, Lau D, Rudy B, and Leonard CS. Function of Specific K+ Channels in Sustained High-Frequency Firing of Fast-Spiking Neocortical Interneurons. *Journal of Neurophysiology* 82: 2476-2489, 1999.

Fagiolini M, Fritschy JM, Low K, Mohler H, Rudolph U, and Hensch TK. Specific GABAA circuits for visual cortical plasticity. *Science* 303: 1681-1683, 2004.

Fanselow EE, Richardson KA, and Connors BW. Selective, State-Dependent Activation of Somatostatin-Expressing Inhibitory Interneurons in Mouse Neocortex. *Journal of Neurophysiology* 100: 2640-2652, 2008.

Feldmeyer D, Lubke J, and Sakmann B. Efficacy and connectivity of intracolumnar pairs of layer 2/3 pyramidal cells in the barrel cortex of juvenile rats. *J Physiol* 575: 583-602, 2006.

Felleman D, Van Essen, D. Distributed Hierarchical Processing in the Primate Cerebral Cortex. *Cereb Cortex* 1: 1-47, 1991.

Ferrarelli F, Massimini M, Peterson MJ, Riedner BA, Lazar M, Murphy MJ, Huber R, Rosanova M, Alexander AL, Kalin N, and Tononi G. Reduced evoked gamma oscillations in the frontal cortex in schizophrenia patients: a TMS/EEG study. *Am J Psychiatry* 165: 996-1005, 2008.

Fino E, and Yuste R. Dense inhibitory connectivity in neocortex. *Neuron* 69: 1188-1203, 2011.

Fleidervish IA, Friedman A, and Gutnick MJ. Slow inactivation of Na+ current and slow cumulative spike adaptation in mouse and guinea-pig neocortical neurones in slices. *J Physiol* 493 (Pt 1): 83-97, 1996.

Fogarty M. GM, Gelman D., Marín O., Pachnis V., Kessaris N. Spatial genetic patterning of the embryonic neuroepithelium generates GABAergic interneuron diversity in the adult cortex. . *J Neurosci* 27: 10935–10946, 2007.

Foster KA, Crowley JJ, and Regehr WG. The Influence of Multivesicular Release and Postsynaptic Receptor Saturation on Transmission at Granule Cell to Purkinje Cell Synapses. *J Neurosci* 25: 11655-11665, 2005.

Galanopoulou AS. Mutations affecting GABAergic signaling in seizures and epilepsy. *Pflugers Arch* 460: 505-523, 2010.

Galarreta M, and Hestrin S. Electrical and chemical synapses among parvalbumin fast-spiking GABAergic interneurons in adult mouse neocortex. *Proc Natl Acad Sci U S A* 99: 12438-12443, 2002.

Gallinat J, Winterer G, Herrmann CS, and Senkowski D. Reduced oscillatory gamma-band responses in unmedicated schizophrenic patients indicate impaired frontal network processing. *Clin Neurophysiol* 115: 1863-1874, 2004.

Gandal MJ, Nesbitt AM, McCurdy RM, and Alter MD. Measuring the maturity of the fast-spiking interneuron transcriptional program in autism, schizophrenia, and bipolar disorder. *PLoS One* 7: e41215, 2012.

Geiger JR, Melcher T, Koh DS, Sakmann B, Seeburg PH, Jonas P, and Monyer H. Relative abundance of subunit mRNAs determines gating and Ca2+ permeability of AMPA receptors in principal neurons and interneurons in rat CNS. *Neuron* 15: 193-204, 1995.

Gibson JR, Beierlein M, and Connors BW. Two networks of electrically coupled inhibitory neurons in neocortex. *Nature* 402: 75-79, 1999.

Gillis KD. Techniques for Membrane Capacitance Measurements. In: *Single Channel Recording*, edited by Neher BSaE. NY: Plenum, 1995, p. 155-198.

Goldberg EM, Clark BD, Zagha E, Nahmani M, Erisir A, and Rudy B. K+ channels at the axon initial segment dampen near-threshold excitability of neocortical fast-spiking GABAergic interneurons. *Neuron* 58: 387-400, 2008.

Goldberg EM, Jeong HY, Kruglikov I, Tremblay R, Lazarenko RM, and Rudy B. Rapid developmental maturation of neocortical FS cell intrinsic excitability. *Cereb Cortex* 21: 666-682, 2011.

Golomb D, Donner K, Shacham L, Shlosberg D, Amitai Y, and Hansel D. Mechanisms of Firing Patterns in Fast-Spiking Cortical Interneurons. *PLoS Comput Biol* 3: e156, 2007.

Gonchar Y, and Burkhalter A. Connectivity of GABAergic calretinin-immunoreactive neurons in rat primary visual cortex. *Cereb Cortex* 9: 683-696, 1999.

Gonchar Y, and Burkhalter A. Distinct GABAergic Targets of Feedforward and Feedback Connections Between Lower and Higher Areas of Rat Visual Cortex. *J Neurosci* 23: 10904-10912, 2003.

Gonchar Y, and Burkhalter A. Three distinct families of GABAergic neurons in rat visual cortex. *Cereb Cortex* 7: 347-358, 1997.

Gonchar Y, Wang Q, and Burkhalter A. Multiple distinct subtypes of GABAergic neurons in mouse visual cortex identified by triple immunostaining. *Front Neuroanat* 1: 1-11, 2007.

Gordon JA, and Stryker MP. Experience-dependent plasticity of binocular responses in the primary visual cortex of the mouse. *J Neurosci* 16: 3274-3286, 1996.

Gu Y, Barry J, McDougel R, Terman D, and Gu C. Alternative splicing regulates kv3.1 polarized targeting to adjust maximal spiking frequency. *J Biol Chem* 287: 1755-1769, 2011.

Guerra L, McGarry LM, Robles V, Bielza C, Larrañaga P, and Yuste R. Comparison between supervised and unsupervised classifications of neuronal cell types: A case study. *Developmental Neurobiology* 71: 71-82, 2011.

Gulyas AI, Szabo GG, Ulbert I, Holderith N, Monyer H, Erdelyi F, Szabo G, Freund TF, and Hajos N. Parvalbumin-containing fast-spiking basket cells generate the field potential oscillations induced by cholinergic receptor activation in the hippocampus. *J Neurosci* 30: 15134-15145, 2010.

Gupta A, Wang Y, and Markram H. Organizing principles for a diversity of GABAergic interneurons and synapses in the neocortex. *Science* 287: 273-278, 2000.

Haider B, Duque A, Hasenstaub AR, and McCormick DA. Neocortical network activity in vivo is generated through a dynamic balance of excitation and inhibition. *J Neurosci* 26: 4535-4545, 2006.

Haider B, Duque A, Hasenstaub AR, Yu Y, and McCormick DA. Enhancement of visual responsiveness by spontaneous local network activity in vivo. *Journal of Neurophysiology* 97: 4186-4202, 2007.

Halabisky B, Shen F, Huguenard JR, and Prince DA. Electrophysiological classification of somatostatin-positive interneurons in mouse sensorimotor cortex. *Journal of Neurophysiology* 96: 834-845, 2006.

Hartigan JA, and Wong MA. Algorithm AS 136: A K-Means Clustering Algorithm. *Journal of the Royal Statistical Society Series C (Applied Statistics)* 28: 100-108, 1979.

Hasenstaub A, Shu Y, Haider B, Kraushaar U, Duque A, and McCormick DA. Inhibitory postsynaptic potentials carry synchronized frequency information in active cortical networks. *Neuron* 47: 423-435, 2005.

Helmstaedter M, Sakmann B, and Feldmeyer D. The relation between dendritic geometry, electrical excitability, and axonal projections of L2/3 Interneurons in rat barrel cortex. *Cereb Cortex* 19: 938-950, 2009.

Hennig C. fpc: Flexible procedures for clustering. 2010.

Hestrin S, and Galarreta M. Electrical synapses define networks of neocortical GABAergic neurons. *Trends Neurosci* 28: 304-309, 2005.

Hippenmeyer S, Vrieseling E, Sigrist M, Portmann T, Laengle C, Ladle DR, and Arber S. A developmental switch in the response of DRG neurons to ETS transcription factor signaling. *PLoS biology* 3: e159, 2005.

Holmgren C, Harkany T, Svennenfors B, and Zilberter Y. Pyramidal cell communication within local networks in layer 2/3 of rat neocortex. *J Physiol* 551: 139-153, 2003.

Holtmaat A, Wilbrecht L, Knott GW, Welker E, and Svoboda K. Experience-dependent and cell-type-specific spine growth in the neocortex. *Nature* 441: 979-983, 2006.

Huang ZJ, Kirkwood A, Pizzorusso T, Porciatti V, Morales B, Bear MF, Maffei L, and Tonegawa S. BDNF regulates the maturation of inhibition and the critical period of plasticity in mouse visual cortex. *Cell* 98: 739-755, 1999.

Hubel D.H. WTN. Receptive fields, binocular interactions, and functional architecture in the cat's visual cortex. *J Physiol* 160: 106-154, 1962.

Jagadeesh B, Gray CM, and Ferster D. Visually evoked oscillations of membrane potential in cells of cat visual cortex. *Science* 257: 552-554, 1992.

Jain D. *Algorithms for Clustering Data*. Prentice-Hall, 1988.

Jonas P, Bischofberger J, Fricker D, and Miles R. Interneuron Diversity series: Fast in, fast out--temporal and spatial signal processing in hippocampal interneurons. *Trends Neurosci* 27: 30-40, 2004.

Juge N, Gray JA, Omote H, Miyaji T, Inoue T, Hara C, Uneyama H, Edwards RH, Nicoll RA, and Moriyama Y. Metabolic control of vesicular glutamate transport and release. *Neuron* 68: 99-112, 2010.

Kandel E, Schwartz, J., Jessel, T. editor. *Principles of Neural Science*. McGraw-Hill, 2000.

Kapfer C, Glickfeld LL, Atallah BV, and Scanziani M. Supralinear increase of recurrent inhibition during sparse activity in the somatosensory cortex. *Nat Neurosci* 10: 743-753, 2007.

Karagiannis A, Gallopin T, David C, Battaglia D, Geoffroy H, Rossier J, Hillman EMC, Staiger JF, and Cauli B. Classification of NPY-Expressing Neocortical Interneurons. *J Neurosci* 29: 3642-3659, 2009.

Karube F, Kubota Y, and Kawaguchi Y. Axon branching and synaptic bouton phenotypes in GABAergic nonpyramidal cell subtypes. *J Neurosci* 24: 2853-2865, 2004.

Kawaguchi Y. Groupings of nonpyramidal and pyramidal cells with specific physiological and morphological characteristics in rat frontal cortex. *Journal of Neurophysiology* 69: 416-431, 1993.

Kawaguchi Y. Physiological subgroups of nonpyramidal cells with specific morphological characteristics in layer II/III of rat frontal cortex. *J Neurosci* 15: 2638-2655, 1995.

Kawaguchi Y, and Kondo S. Parvalbumin, somatostatin and cholecystokinin as chemical markers for specific GABAergic interneuron types in the rat frontal cortex. *J Neurocytol* 31: 277-287, 2002.

Kawaguchi Y, and Kubota Y. Correlation of physiological subgroupings of nonpyramidal cells with parvalbumin- and calbindinD28k-immunoreactive neurons in layer V of rat frontal cortex. *Journal of Neurophysiology* 70: 387-396, 1993.

Kawaguchi Y, and Kubota Y. GABAergic cell subtypes and their synaptic connections in rat frontal cortex. *Cereb Cortex* 7: 476-486, 1997.

Kawaguchi Y, and Kubota Y. Neurochemical features and synaptic connections of large physiologically-identified GABAergic cells in the rat frontal cortex. *Neuroscience* 85: 677-701, 1998.

Kisvarday ZF. GABAergic networks of basket cells in the visual cortex. *Prog Brain Res* 90: 385-405, 1992.

Kondo M, Sumino R, and Okado H. Combinations of AMPA receptor subunit expression in individual cortical neurons correlate with expression of specific calcium-binding proteins. *J Neurosci* 17: 1570-1581, 1997.

Krimer LS, and Goldman-Rakic PS. Prefrontal Microcircuits: Membrane Properties and Excitatory Input of Local, Medium, and Wide Arbor Interneurons. *J Neurosci* 21: 3788-3796, 2001.

Krimer LS, Zaitsev AV, Czanner G, Kroner S, Gonzalez-Burgos G, Povysheva NV, Iyengar S, Barrionuevo G, and Lewis DA. Cluster analysis-based physiological classification and morphological properties of inhibitory neurons in layers 2-3 of monkey dorsolateral prefrontal cortex. *Journal of neurophysiology* 94: 3009-3022, 2005.

Kubota Y, and Kawaguchi Y. Dependence of GABAergic synaptic areas on the interneuron type and target size. *J Neurosci* 20: 375-386, 2000.

Kubota Y, Shigematsu N, Karube F, Sekigawa A, Kato S, Yamaguchi N, Hirai Y, Morishima M, and Kawaguchi Y. Selective coexpression of multiple chemical markers defines discrete populations of neocortical GABAergic neurons. *Cereb Cortex* 21: 1803-1817, 2011.

Kuffler S. DISCHARGE PATTERNS AND FUNCTIONAL ORGANIZATION OF MAMMALIAN RETINA. *Journal of Neurophysiology* 16: 37-68, 1953.

Kuhlman SJ, and Huang ZJ. High-resolution labeling and functional manipulation of specific neuron types in mouse brain by Cre-activated viral gene expression. *PLoS One* 3: e2005, 2008.

Lambolez B, Ropert N, Perrais D, Rossier J, and Hestrin S. Correlation between kinetics and RNA splicing of alpha-amino-3-hydroxy-5-methylisoxazole-4-propionic acid receptors in neocortical neurons. *Proc Natl Acad Sci U S A* 93: 1797-1802, 1996.

Lau D, Vega-Saenz de Miera EC, Contreras D, Ozaita A, Harvey M, Chow A, Noebels JL, Paylor R, Morgan JI, Leonard CS, and Rudy B. Impaired fast-spiking, suppressed cortical inhibition, and increased susceptibility to seizures in mice lacking Kv3.2 K+ channel proteins. *J Neurosci* 20: 9071-9085, 2000.

Lazarus MS, and Huang ZJ. Distinct maturation profiles of perisomatic and dendritic targeting GABAergic interneurons in the mouse primary visual cortex during the critical period of ocular dominance plasticity. *Journal of Neurophysiology* 106: 775-787, 2011.

Lee S, Hjerling-Leffler J, Zagha E, Fishell G, and Rudy B. The largest group of superficial neocortical GABAergic interneurons expresses ionotropic serotonin receptors. *J Neurosci* 30: 16796-16808, 2010.

Lee SH, Kwan AC, Zhang S, Phoumthipphavong V, Flannery JG, Masmanidis SC, Taniguchi H, Huang ZJ, Zhang F, Boyden ES, Deisseroth K, and Dan Y. Activation of specific interneurons improves V1 feature selectivity and visual perception. *Nature* 488: 379-383, 2012.

Lee WC, Chen JL, Huang H, Leslie JH, Amitai Y, So PT, and Nedivi E. A dynamic zone defines interneuron remodeling in the adult neocortex. *Proc Natl Acad Sci U S A* 105: 19968-19973, 2008.

Lewis DA, Curley AA, Glausier JR, and Volk DW. Cortical parvalbumin interneurons and cognitive dysfunction in schizophrenia. *Trends Neurosci* 35: 57-67, 2012.

Lodge DJ, Behrens MM, and Grace AA. A Loss of Parvalbumin-Containing Interneurons Is Associated with Diminished Oscillatory Activity in an Animal Model of Schizophrenia. *J Neurosci* 29: 2344-2354, 2009.

Ma WP, Liu BH, Li YT, Huang ZJ, Zhang LI, and Tao HW. Visual representations by cortical somatostatin inhibitory neurons--selective but with weak and delayed responses. *J Neurosci* 30: 14371-14379, 2010.

Ma Y, Hu H, Berrebi AS, Mathers PH, and Agmon A. Distinct subtypes of somatostatin-containing neocortical interneurons revealed in transgenic mice. *J Neurosci* 26: 5069-5082, 2006.

Maffei A, and Turrigiano GG. Multiple Modes of Network Homeostasis in Visual Cortical Layer 2/3. *J Neurosci* 28: 4377-4384, 2008.

Malenka RC, and Bear MF. LTP and LTD: an embarrassment of riches. *Neuron* 44: 5-21, 2004.

Mann EO, and Paulsen O. Role of GABAergic inhibition in hippocampal network oscillations. *Trends Neurosci* 30: 343-349, 2007.

Marin O. Interneuron dysfunction in psychiatric disorders. *Nat Rev Neurosci* 13: 107-120, 2012.

Markram H, Toledo-Rodriguez M, Wang Y, Gupta A, Silberberg G, and Wu C. Interneurons of the neocortical inhibitory system. *Nat Rev Neurosci* 5: 793-807, 2004.

Mason A, Nicoll A, and Stratford K. Synaptic transmission between individual pyramidal neurons of the rat visual cortex in vitro. *J Neurosci* 11: 72-84, 1991.

McCormick DA, Connors BW, Lighthall JW, and Prince DA. Comparative electrophysiology of pyramidal and sparsely spiny stellate neurons of the neocortex. *Journal of Neurophysiology* 54: 782-806, 1985.

McGarry LM, Packer AM, Fino E, Nikolenko V, Sippy T, and Yuste R. Quantitative classification of somatostatin-positive neocortical interneurons identifies three interneuron subtypes. *Front Neural Circuits* 4: 12, 2010.

Mensi S, Naud R, Pozzorini C, Avermann M, Petersen CC, and Gerstner W. Parameter extraction and classification of three cortical neuron types reveals two distinct adaptation mechanisms. *Journal of Neurophysiology* 107: 1756-1775, 2012.

Meyer AH, Katona In, Blatow M, Rozov A, and Monyer H. In Vivo Labeling of Parvalbumin-Positive Interneurons and Analysis of Electrical Coupling in Identified Neurons. *The Journal of Neuroscience* 22: 7055-7064, 2002.

Miles R, Toth K, Gulyas AI, Hajos N, and Freund TF. Differences between somatic and dendritic inhibition in the hippocampus. *Neuron* 16: 815-823, 1996.

Miller MN, Okaty BW, Kato S, and Nelson SB. Activity-dependent changes in the firing properties of neocortical fast-spiking interneurons in the absence of large changes in gene expression. *Dev Neurobiol* 71: 62-70, 2011.

Miller MN, Okaty BW, and Nelson SB. Region-specific spike-frequency acceleration in layer 5 pyramidal neurons mediated by Kv1 subunits. *J Neurosci* 28: 13716-13726, 2008.

Milstein AD, and Nicoll RA. Regulation of AMPA receptor gating and pharmacology by TARP auxiliary subunits. *Trends Pharmacol Sci* 29: 333-339, 2008.

Miyoshi G, Butt SJ, Takebayashi H, and Fishell G. Physiologically distinct temporal cohorts of cortical interneurons arise from telencephalic Olig2-expressing precursors. *J Neurosci* 27: 7786-7798, 2007.

Miyoshi G, and Fishell G. GABAergic Interneuron Lineages Selectively Sort into Specific Cortical Layers during Early Postnatal Development. *Cereb Cortex* 2011.

Miyoshi G, Hjerling-Leffler J, Karayannis T, Sousa VH, Butt SJ, Battiste J, Johnson JE, Machold RP, and Fishell G. Genetic fate mapping reveals that the caudal ganglionic eminence

produces a large and diverse population of superficial cortical interneurons. *J Neurosci* 30: 1582-1594, 2010.

Morales B, Choi SY, and Kirkwood A. Dark rearing alters the development of GABAergic transmission in visual cortex. *J Neurosci* 22: 8084-8090, 2002.

Murtagh F. *Multidimensional Clustering Algorithms*. Physica-Verlag, 1985.

Murtagh F, Heck, A. *Multivariate Data Analysis*. Dordrecht: Kluwer Academic Publishers, 1987.

Nowak LG, Azouz R, Sanchez-Vives MV, Gray CM, and McCormick DA. Electrophysiological classes of cat primary visual cortical neurons in vivo as revealed by quantitative analyses. *Journal of Neurophysiology* 89: 1541-1566, 2003.

Okaty BW, Miller MN, Sugino K, Hempel CM, and Nelson SB. Transcriptional and electrophysiological maturation of neocortical fast-spiking GABAergic interneurons. *J Neurosci* 29: 7040-7052, 2009.

Oliva AA, Jr., Jiang M, Lam T, Smith KL, and Swann JW. Novel hippocampal interneuronal subtypes identified using transgenic mice that express green fluorescent protein in GABAergic interneurons. *J Neurosci* 20: 3354-3368, 2000.

Orekhova EV, Stroganova TA, Nygren G, Tsetlin MM, Posikera IN, Gillberg C, and Elam M. Excess of high frequency electroencephalogram oscillations in boys with autism. *Biol Psychiatry* 62: 1022-1029, 2007.

Otto JF, Yang Y, Frankel WN, White HS, and Wilcox KS. A spontaneous mutation involving Kcnq2 (Kv7.2) reduces M-current density and spike frequency adaptation in mouse CA1 neurons. *J Neurosci* 26: 2053-2059, 2006.

Pan Y, Weng J, Levin EJ, and Zhou M. Oxidation of NADPH on Kvbeta1 inhibits ball-and-chain type inactivation by restraining the chain. *Proc Natl Acad Sci U S A* 108: 5885-5890, 2011.

Pare D, Shink E, Gaudreau H, Destexhe A, and Lang EJ. Impact of spontaneous synaptic activity on the resting properties of cat neocortical pyramidal neurons In vivo. *Journal of neurophysiology* 79: 1450-1460, 1998.

Porter JT, Cauli B, Staiger JF, Lambolez B, Rossier J, and Audinat E. Properties of bipolar VIPergic interneurons and their excitation by pyramidal neurons in the rat neocortex. *Eur J Neurosci* 10: 3617-3628, 1998.

Povysheva NV, Zaitsev AV, Rotaru DC, Gonzalez-Burgos G, Lewis DA, and Krimer LS. Parvalbumin-Positive Basket Interneurons in Monkey and Rat Prefrontal Cortex. *Journal of Neurophysiology* 100: 2348-2360, 2008.

R Development Core Team RFfSC. R: A Language and Environment for Statistical Computing. 2005.

Reyes A, Lujan R, Rozov A, Burnashev N, Somogyi P, and Sakmann B. Target-cell-specific facilitation and depression in neocortical circuits. *Nat Neurosci* 1: 279-285, 1998.

Rhodes KJ, Strassle BW, Monaghan MM, Bekele-Arcuri Z, Matos MF, and Trimmer JS. Association and colocalization of the Kvbeta1 and Kvbeta2 beta-subunits with Kv1 alpha-subunits in mammalian brain K+ channel complexes. *J Neurosci* 17: 8246-8258, 1997.

Rousseeuw PJ. Silhouettes: a Graphical Aid to the Interpretation and Validation of Cluster Analysis. *Journal of Computational and Applied Mathematics* 20: 53-65, 1987.

Rozov A, Burnashev N, Sakmann B, and Neher E. Transmitter release modulation by intracellular Ca2+ buffers in facilitating and depressing nerve terminals of pyramidal cells in layer 2/3 of the rat neocortex indicates a target cell-specific difference in presynaptic calcium dynamics. *J Physiol* 531: 807-826, 2001a.

Rozov A, Jerecic J, Sakmann B, and Burnashev N. AMPA Receptor Channels with Long-Lasting Desensitization in Bipolar Interneurons Contribute to Synaptic Depression in a Novel Feedback Circuit in Layer 2/3 of Rat Neocortex. *J Neurosci* 21: 8062-8071, 2001b.

Rudy B, Fishell G, Lee S, and Hjerling-Leffler J. Three groups of interneurons account for nearly 100% of neocortical GABAergic neurons. *Developmental Neurobiology* 71: 45-61, 2011.

Runyan CA, Schummers J, Van Wart A, Kuhlman SJ, Wilson NR, Huang ZJ, and Sur M. Response features of parvalbumin-expressing interneurons suggest precise roles for subtypes of inhibition in visual cortex. *Neuron* 67: 847-857, 2010.

Sah P. Ca(2+)-activated K+ currents in neurones: types, physiological roles and modulation. *Trends Neurosci* 19: 150-154, 1996.

Schaefer AT, Angelo K, Spors H, and Margrie TW. Neuronal oscillations enhance stimulus discrimination by ensuring action potential precision. *PLoS biology* 4: e163, 2006.

Searl TJ, and Silinsky EM. Evidence for two distinct processes in the final stages of neurotransmitter release as detected by binomial analysis in calcium and strontium solutions. *J Physiol* 539: 693-705, 2002.

Shipp S. Structure and function of the cerebral cortex. *Current Biology* 17: R443-339, 2007.
Shipp S. The functional logic of cortico_pulvinar connections. *Philos Trans R Soc Lond B Biol Sci* 358: 1605-1624, 2003.

Sohal VS, Zhang F, Yizhar O, and Deisseroth K. Parvalbumin neurons and gamma rhythms enhance cortical circuit performance. *Nature* 459: 698-702, 2009.

Somogyi P. A specific 'axo-axonal' interneuron in the visual cortex of the rat. *Brain Res* 136: 345-350, 1977.

Somogyi P, and Cowey A. Combined Golgi and electron microscopic study on the synapses formed by double bouquet cells in the visual cortex of the cat and monkey. *J Comp Neurol* 195: 547-566, 1981.

Somogyi P, Kisvarday ZF, Martin KA, and Whitteridge D. Synaptic connections of morphologically identified and physiologically characterized large basket cells in the striate cortex of cat. *Neuroscience* 10: 261-294, 1983.

Somogyi P, and Klausberger T. Defined types of cortical interneurone structure space and spike timing in the hippocampus. *J Physiol* 562: 9-26, 2005.

Spencer KM, Niznikiewicz MA, Shenton ME, and McCarley RW. Sensory-evoked gamma oscillations in chronic schizophrenia. *Biol Psychiatry* 63: 744-747, 2008.

Steriade M, Amzica F, and Contreras D. Synchronization of fast (30-40 Hz) spontaneous cortical rhythms during brain activation. *J Neurosci* 16: 392-417, 1996.

Strauss U, Herbrik M, Mix E, Schubert R, and Rolfs A. Whole-cell patch-clamp: true perforated or spontaneous conventional recordings? *Pflugers Arch* 442: 634-638, 2001.

Sudhof TC. The Synaptic Vesicle Cycle. *Annu Rev Neurosci* 27: 509-547, 2004.

Suzuki R, and Shimodaira H. pvclust: Hierarchical Clustering with P-Values via Multiscale Bootstrap Resampling. 2009.

Tamas G, Lorincz A, Simon A, and Szabadics J. Identified sources and targets of slow inhibition in the neocortex. *Science* 299: 1902-1905, 2003.

Tamas G, Somogyi P, and Buhl EH. Differentially interconnected networks of GABAergic interneurons in the visual cortex of the cat. *J Neurosci* 18: 4255-4270, 1998.

Telgarsky M, Vattani, A. Hartigan's Method: k-means Clustering without Voronoi. In: *13th International Conference on Artificial Intelligence and Statistics (AISTATS)*. Chia Laguna Resort, Sardinia, Italy.: JMLR, 2010.

Thomson AM. Activity-dependent properties of synaptic transmission at two classes of connections made by rat neocortical pyramidal axons in vitro. *J Physiol* 502 (Pt 1): 131-147, 1997.

Thomson AM, and Bannister AP. Interlaminar connections in the neocortex. *Cereb Cortex* 13: 5-14, 2003.

Thomson AM, West DC, Wang Y, and Bannister AP. Synaptic Connections and Small Circuits Involving Excitatory and Inhibitory Neurons in Layers 2-5 of Adult Rat and Cat Neocortex: Triple Intracellular Recordings and Biocytin Labelling In Vitro. *Cereb Cortex* 12: 936-953, 2002.

Toledo-Rodriguez M, Blumenfeld B, Wu C, Luo J, Attali B, Goodman P, and Markram H. Correlation maps allow neuronal electrical properties to be predicted from single-cell gene expression profiles in rat neocortex. *Cereb Cortex* 14: 1310-1327, 2004.

Toledo-Rodriguez M, Goodman P, Illic M, Wu C, and Markram H. Neuropeptide and calcium-binding protein gene expression profiles predict neuronal anatomical type in the juvenile rat. *J Physiol* 567: 401-413, 2005.

Torrey EF, Barci BM, Webster MJ, Bartko JJ, Meador-Woodruff JH, and Knable MB. Neurochemical markers for schizophrenia, bipolar disorder, and major depression in postmortem brains. *Biol Psychiatry* 57: 252-260, 2005.

Turrigiano GG, Leslie KR, Desai NS, Rutherford LC, and Nelson SB. Activity-dependent scaling of quantal amplitude in neocortical neurons. *Nature* 391: 892-896, 1998.

Wadiche JI, and Jahr CE. Multivesicular Release at Climbing Fiber-Purkinje Cell Synapses. *Neuron* 32: 301-313, 2001.

Wang Y, Gupta A, Toledo-Rodriguez M, Wu CZ, and Markram H. Anatomical, Physiological, Molecular and Circuit Properties of Nest Basket Cells in the Developing Somatosensory Cortex. *Cereb Cortex* 12: 395-410, 2002.

Wang Y, Toledo-Rodriguez M, Gupta A, Wu C, Silberberg G, Luo J, and Markram H. Anatomical, physiological and molecular properties of Martinotti cells in the somatosensory cortex of the juvenile rat. *J Physiol* 561: 65-90, 2004.

Watanabe J, Rozov A, and Wollmuth LP. Target-specific regulation of synaptic amplitudes in the neocortex. *J Neurosci* 25: 1024-1033, 2005.

Whittington MA, and Traub RD. Interneuron Diversity series: Inhibitory interneurons and network oscillations in vitro. *Trends in Neurosciences* 26: 676-682, 2003.

Wilson NR, Runyan CA, Wang FL, and Sur M. Division and subtraction by distinct cortical inhibitory networks in vivo. *Nature* 488: 343-348, 2012.

Woodruff A, Xu Q, Anderson SA, and Yuste R. Depolarizing effect of neocortical chandelier neurons. *Front Neural Circuits* 3: 15, 2009.

Wu X-S, Xue L, Mohan R, Paradiso K, Gillis KD, and Wu L-G. The Origin of Quantal Size Variation: Vesicular Glutamate Concentration Plays a Significant Role. *J Neurosci* 27: 3046-3056, 2007.

Xu X, and Callaway EM. Laminar Specificity of Functional Input to Distinct Types of Inhibitory Cortical Neurons. *J Neurosci* 29: 70-85, 2009.

Xu X, Roby KD, and Callaway EM. Immunochemical characterization of inhibitory mouse cortical neurons: three chemically distinct classes of inhibitory cells. *J Comp Neurol* 518: 389-404, 2010.

Yizhar O, Fenno LE, Prigge M, Schneider F, Davidson TJ, O'Shea DJ, Sohal VS, Goshen I, Finkelstein J, Paz JT, Stehfest K, Fudim R, Ramakrishnan C, Huguenard JR, Hegemann P, and Deisseroth K. Neocortical excitation/inhibition balance in information processing and social dysfunction. *Nature* 477: 171-178, 2011.

Zaitsev AV, Gonzalez-Burgos G, Povysheva NV, Kroner S, Lewis DA, and Krimer LS. Localization of calcium-binding proteins in physiologically and morphologically characterized interneurons of monkey dorsolateral prefrontal cortex. *Cereb Cortex* 15: 1178-1186, 2005.

Zilberter Y, Kaiser KM, and Sakmann B. Dendritic GABA release depresses excitatory transmission between layer 2/3 pyramidal and bitufted neurons in rat neocortex. *Neuron* 24: 979-988, 1999.

Zucker RS, and Regehr WG. SHORT-TERM SYNAPTIC PLASTICITY. *Annu Rev Physiol* 64: 355-405, 2002.